UNIVERSIDADE ESTADUAL DE CAMPINAS

Instituto de Física "Gleb Wataghin"

Caroline Lydie Mouls

Growth, characterization and magnetoelectric study of ferromagnet-ferroelectric heterostructures

Crescimento, caracterização e estudo magnetoelétrico de heteroestruturas ferromagnéticas-ferroelétricas

Campinas, 2017

Caroline Lydie Mouls

Growth, characterization and magnetoelectric study of ferromagnet-ferroelectric heterostructures

Crescimento, caracterização e estudo magnetoelétrico de heteroestruturas ferromagnéticas-ferroelétricas

Dissertation presented to the Institute of Physics Gleb Wataghin of the University of Campinas in partial fulfillment of the requirements for the degree of Doctor in Sciences.

Tese apresentada ao Instituto de Física Gleb Wataghin da Universidade Estadual de Campinas como parte dos requisitos exigidos para a obtenção do título de Doutora em Ciências

Orientador/*Supervisor*: Julio Criginski Cezar

Co-orientador/*Co-supervisor*: Eduardo Granado Monteiro da Silva

ESTE EXEMPLAR CORRESPONDE À VERSÃO FINAL DA TESE DEFENDIDA PELA ALUNA CAROLINE LYDIE MOULS E ORIENTADA PELO DR. JULIO CRIGINSKI CEZAR.

Campinas, 2017

Agência(s) de fomento e nº(s) de processo(s): FAPESP, 2013/12423-3; FAPESP, 2012/51198-2

Ficha catalográfica
Universidade Estadual de Campinas
Biblioteca do Instituto de Física Gleb Wataghin
Maria Graciele Trevisan - CRB 8/7450

M861g

Mouls, Caroline Lydie, 1987-
Growth, characterization and magnetoelectric study of ferromagnet-ferroelectric heterostructures / Caroline Lydie Mouls. – Campinas, SP : [s.n.], 2017.

Orientador: Julio Criginski Cezar.
Coorientador: Eduardo Granado Monteiro da Silva.
Tese (doutorado) – Universidade Estadual de Campinas, Instituto de Física Gleb Wataghin.

1. Ferroeletricidade. 2. Filmes finos. 3. Ferromagnetismo. I. Cezar, Julio Criginski, 1972-. II. Silva, Eduardo Granado Monteiro da, 1974-. III. Universidade Estadual de Campinas. Instituto de Física Gleb Wataghin. IV. Título.

Informações para Biblioteca Digital

Título em outro idioma: Crescimento, caracterização e estudo magnetoelétrico de heteroestruturas ferromagnéticas-ferroelétricas
Palavras-chave em inglês:
Ferroelectricity
Thin films
Ferromagnetism
Área de concentração: Física
Titulação: Doutora em Ciências
Banca examinadora:
Julio Criginski Cezar [Orientador]
Cris Adriano
Pascoal José Giglio Pagliuso
João Paulo Sinnecker
Ducinei Garcia
Data de defesa: 27-10-2017
Programa de Pós-Graduação: Física

MEMBROS DA COMISSÃO JULGADORA DA TESE DE DOUTORADO DE **CAROLINE LYDIE MOULS - RA 151611** APRESENTADA E APROVADA AO INSTITUTO DE FÍSICA "GLEB WATAGHIN", DA UNIVERSIDADE ESTADUAL DE CAMPINAS, EM 27/10/2017.

COMISSÃO JULGADORA:

- Prof. Dr. Júlio Criginski Cezar – Laboratório Nacional de Luz Síncrotron/CNPEM/MCT
- Profa. Dra. Cris Adriano – IFGW/UNICAMP
- Prof. Dr. Pascoal José Giglio Pagliuso – IFGW/UNICAMP
- Prof. Dr. João Paulo Sinnecker – Centro Brasileiro de Pesquisas Físicas
- Profa. Dra. Ducinei Garcia – Universidade Estadual de São Carlos

OBS.: Informo que as assinaturas dos respectivos professores membros da banca constam na ata de defesa já juntada no processo vida acadêmica do aluno.

CAMPINAS
2017

Acknowledgements

Eu passei quatros anos trabalhando num grupo muito legal. Na verdade é mais que muito legal, é *irado*, como diria o Jeovani. Isso com certeza tem muito a ver com meu orientador, Julio. Ele consegue resolver todos os problemas dos estudantes dele, de consertar descargas no PEEM até tentar salvar a vida de um pássaro ferido. Ele sempre me apoiou e sempre foi presente para mim. Muito obrigada Julio para me dar a oportunidade de trabalhar com você. Quero agradecer também ao Pedro e ao Thiago, cuja experiência me ajudou muito no meu projeto. Quero agradecer também todo o pessoal da linha PGM, o Horácio, a Camili, o Mirko, o Wendell e os outros. Foi muito bom trabalhar com vocês.

As *crianças* sempre tiveram um lugar especial no meu coração. Karine, Paloma, Maíra, os Lucas e os Felipes, muito obrigada por ter me ensinado todo o refinamento da cultura brasileira. Também quero agradecer as pessoas da república "Madalena Arrependida", a melhor república de Barão Geraldo. Foi muito legal conviver com vocês, já estou com saudade. Também vou sentir saudade dos peruanos, Fio, Marvyn, Guille, Alain, e do quase peruano Rene. Foi muito bom criticar a comida brasileira com vocês.

I also want to thank the people who helped me in Berlin, Slavomir, Johanna,

Imtiaz and Stefan, thank you for all you taught me. Your help enabled me to finish my PhD. I also want to thank Thomas for growing the two MgO/Fe/BTO samples, which gave the best results. In particular, we would like to acknowledge Prof. Dr. Claus M. Schneider for the collaboration opportunity.

This PhD work was funded by the São Paulo Research Foundation, FAPESP, under grant 2013/12423-3, as part of the FAPESP Young Researcher grant 2012/51198-2.

Abstract

The results of this thesis can be separated in two main lines: i) growth and characterization of ferroelectric thin films; ii) magnetoelectric characterization of Fe thin films grew on $BaTiO_3$ substrates. We succeed to fabricate simple thin films of $BiFeO_3$ and $SrRuO_3$ by RF-magnetron sputtering. The films where characterized by several structural and spectroscopic techniques, showing that in some cases we obtained very high quality epitaxial films. Besides the results on thin film growth, we characterized the ferroelectric domains of a thin iron magnetic film grown on top of a ferroelectric $BaTiO_3$ substrate. This kind of system behaves as a magnetoelectric multiferroic heterostructure. We studied the interaction between ferroelectric and ferromagnetic domains mostly by photoelectron emission microscopy (PEEM). This technique allows one to obtain microscopic information about the electric and magnetic domains in the sample. We were able to demonstrate the interaction between the magnetic and ferroelectric degrees of freedom in such heterostructures. We found that the underlying ferroelectric domains on $BaTiO_3$ in some situations determine the orientation of the top Fe magnetic layer. These results show the potential of such artificial magnetoelectric heterostructure to control the magnetic state through the application of electrical voltages.

Keywords: Multiferroics. Ferroelectrics. Magnetoelectrics. Thin films. Photoelectron emission microsocopy.

Resumo

Os resultados dessa tese podem ser separados em duas linhas principais: i) crescimento e caracterização de filmes finos ferroelétricos; ii) caracterização magnetoelétrica de filmes finos de Fe crescidos sobre substratos de $BaTiO_3$. Conseguimos fabricar filmes finos simples de $BiFeO_3$ e $SrRuO_3$ por *RF-magnetron sputtering*. Esses filmes foram caracterizados por diversas técnicas estruturais e espectroscópicas, demonstrando que em alguns casos obtivemos filmes epitaxiais de alta qualidade. Além dos resultados em filmes finos, neste trabalho de doutorado também investigamos a interação entre os domínios ferromagnéticos e os domínios ferroelétricos de um filme fino magnético crescido sobre um substrato ferroelétrico. Esse tipo de sistema se apresenta como uma heteroestrutura multiferroica magnetoelétrica. O objetivo desse trabalho é compreender como se dá a interação de um filme fino de ferro crescido sobre um monocristal ferroelétrico de $BaTiO_3$. Para esse fim empregamos principalmente a técnica de microscopia de emissão de fotoelétrons (PEEM). Essa técnica permite obter informação micrométrica sobre o estado de polarização elétrica e magnetização da amostra. Dessa forma demonstramos que sob condições controladas existe uma interação entre os domínios ferroelétricos e ferromagnéticos nessa heteroestrutura. Nossos resultados mostraram que os domínios ferroelétricos do substrato de $BaTiO_3$ determinam a orientação dos domínios magnéticos de camadas ultrafinas de Fe. Esses resultados demonstram o potencial desse tipo de heteroestrutura para aplicações onde um estado magnético pode ser alterado através de um potencial elétrico.

Palavras-chave: Multiferroicos. Ferroelétricos. Magnetoelétricos. Filmes finos. Microscopia de emissão de fotoelétrons.

List of Tables

Contents

Chapter 1

Introduction: magnetism and ferroelectricity

Although ferroelectric materials are less known than ferromagnetic materials, ferroelectrics are already used in many applications. Some of these applications just depend on the piezoelectric, pyroelectric or dielectric properties of ferroelectric materials, as it is the case for micro motors, micro capacitors, piezoelectric generators, or microsensors [1]. But other applications are also related with the existence and the possible switch of the electrical polarization for ferroelectrics. An example of these applications are ferroelectric random access memory (FeRAM) memories, which are non-volatile memories [2]. Each memory cell (bit) is formed by a capacitor, constituted by a thin ferroelectric film between two electrodes and whose electric polarization corresponds to the values 1 or 0 of the bit, and of a transistor, which makes possible to select the desired cell among the others. A voltage greater than the voltage required to switch the electric polarization is applied only if the two inputs of the transistor, one corresponding to "Bit line" and one to "Word line", are active. When the cell is selected, the current passing through the capacitor is compared to the current passing through another similar capacitor, used

as a reference. If the two do not have the same electric polarization, the difference of intensity between the two will be appreciable (if the capacitor has an electric polarization reversed in comparison to the electric field generated by the applied voltage, we will have, in addition to the leakage current, a current related to the switch of the electric polarization). This configuration is called 1T1C (1 transistor, 1 capacitor), but a 2T2C configuration can also be found, where another transistor/capacitor set is added as reference for each cell, to avoid the fatigue due to a unique reference for all cells. These FeRAM memories are already commercialized, for example, SAMSUNG uses a thin film of lead titanate zirconate (PZT) of 4 Mbit, and configuration of 1T1C. The fact of switching the electric polarization each time it is opposite to the applied electric field implies that the reverted polarization must be switched again for not loosing the information of the bit, the reading is thus destructive. These polarization switchings generate significant material degradation.However, even with this material degradation, FeRAM are more fatigue resistant than the most commonly used FLASH memories. The biggest disadvantage of FeRAM, compared to Flash, is the price and the small memory density, points that can be improved with the study of new materials. On the other hand, with the possibility of growing extremely thin films, it is possible to change the electric polarization of ferroelectrics with a voltage of only 1V, whereas flash memories can not be used with less than 5V [3]. Another ferroelectric memory, which is not yet commercialized, is the ferroelectric field effect transistor (FeFET) memory [2], in which a ferroelectric thin film is used instead of a dielectric layer normally found in a field effect transistor (FET) memory. Writing is done with the application of voltage pulses, which determine the electric polarization of the ferroelectric. This polarization will generate charges on the surfaces. At the interface between the ferroelectric and the semiconductor, opposite mobile charges will appear on the semiconductor side, and these charges will change the resistance between the source

and the FET drain. The reading is made by measuring the resistance between the source and the drain, and in this case is not destructive, and thus more resistant to the fatigue (it is only necessary to change the polarization for the writing, which is less frequent than the reading). On the other hand, a buffer layer must be used between the ferroelectric and semiconductor layers to prevent injection of charges, even if this reduces the voltage applied to the ferroelectric. In order to improve the use of FeFET and to imagine commercialization, the leakage current must still be reduced as it complicates the reading of the state [4]. Magnetic memories, such as hard disk drive or magnetoresistive random access memory (using magnetic tunnel junctions), are still more widely used. But using the coupling between magnetic and electric order in multiferroic magnetoelectric materials, one could use the advantage of both types, implementing magnetic memories with electrical writing, or memories of four states (two for magnetization and two for electrical polarization). Magnetic multiferroic could also find other application as microwave components, magnetic field sensors or even for magnetoelectric probes for scanning probe microscopy [5].

The objective of this thesis is to study the interaction between magnetic and ferroelectric domains in multiferroic, magnetoelectric systems. To accomplish this work, we grew ferromagnetic and ferroelectric thin films, and characterized their chemical composition, crystalline structure and electronic structure. Finally we determined the microscopic interaction between ferroelectric or ferromagnetic domains.

To understand the concepts involved in this work, in this chapter we introduce the background theory for this project, recalling some basics about magnetism, ferroelectricity, multiferroicity and the magnetoelectric coupling mechanism. In chapter 2 we present the experimental techniques used along this work. Finally, in chapters 3 and 4

we present and discuss the results obtained during this project.

1.1 Magnetism

Classical mechanics can give useful insights on magnetic effects. Considering that the movement of the electron consists on a constant circular orbit around the nucleus, we can for example explain the diamagnetic effect, present in all materials, as explained in [6], when you turn on a magnetic field, currents are generated inside the atom by induction. According to Lenz 's law, the direction of these currents (and thus the induced magnetic moments) will be opposite to the direction of the initial magnetic field. The gyromagnetic ratio of a particle (ratio of the magnetic moment divided by the angular momentum) calculated classically gives $\gamma = \frac{e}{2m}$, with e the charge of the particle and m its mass. Although not valid only for general case, it gives the $\frac{1}{m}$ dependence of the magnetic moment, explaining why magnetism of electrons is much higher than magnetism of protons, and thus why electron contribution is generally the only one considered. However,the explanation of magnetism effect with classical mechanics is quite limited. For example, classically, diamagnetism and paramagnetism should cancel each other, and it is not possible to explain the quantization of magnetic moments of isolated atoms. Indeed, magnetism is a quantum-mechanical phenomenon. Magnetism of matter comes from spin and orbital momentum contribution of an electronic incomplete shell, as for a complete shell the individual electron contribution cancel each other. More precisely, for one electron, the total magnetic dipole moment $\vec{\mu_J}$, resulting from both spin and orbital momentum is related to the total angular momentum $\vec{J}$ of this electron by :

$$\vec{\mu_J} = g_J \mu_B \frac{\vec{J}}{\hbar} \tag{1.1}$$

With g_J the Landé factor and μ_B the Bohr magneton. When magnetic moments of individual electrons are ordered (anti-)parallel over several atoms (long range ordering), the material is said to be (anti-)ferromagnetic. On the contrary, a material showing individual magnetic moments without long range ordering is said to be paramagnetic.

For all ferromagnetic materials there is a transition temperature, named Curie temperature, T_c, above which thermal fluctuation overcome the magnetic long range ordering, corresponding to a phase transition to the paramagnetic phase.

Finally, depending on the external applied magnetic field, the magnetization history of the sample and its interaction with the environment, ferromagnetic materials develop regions of uniform magnetization, called magnetic domains. These domains are particularly important within this project and will be discussed in detail on the next section.

1.1.1 Magnetic domains formation

Whereas electric dipolar interaction is enough to explain the ordering of electrical polarization in ferroelectric materials, the magnetic dipolar interaction is too weak to explain alone the magnetic ordering. A difference in energy for states of different spin can be explained by exchange interactions. With the need for the many-body electron wavefunction to be antisymmetric, electrons of same spin can not be at the same position (Pauli principle), and then electrons of same spin tend to avoid each other, which results in a minimization of coulomb repulsion. This Coulomb exchange favors ferromagnetism, whereas kinetic exchange, due to the possible hopping of electrons between atoms leading to the reduction of the kinetic energy when electrons are delocalized, favors anti-ferromagnetism [7]. In crystalline magnetic materials, whereas the spin moments are

isotropic and do not interact directly with the lattice, the electronic orbitals have an interaction with the crystal field generated by the lattice. These electrostatic interactions lead to an alignment of the electronic orbitals in preferential directions according to their symmetry. This anisotropy existing for orbital magnetic moments is coupled to the spin moments via spin-orbit coupling [8]. The preferential axes for magnetization are named easy axes, whereas the axis for which the maximum energy is necessary for aligning the magnetization are hard axes. The effective anisotropy energy is the energy necessary to rotate the magnetization from easy to hard direction. The minimization of the magnetostatic energy can also be seen as a source of anisotropy. The magnetostatic energy is a consequence of dipole-dipole interaction between magnetic moments. It can be decomposed into two contribution, one volume contribution depending on the gradient of magnetization, and the other is a surface contribution. This surface contribution depends on the term $\vec{M}.\vec{n}$, $\vec{n}$ being the surface normal. This $\vec{M}.\vec{n}$ term can be seen as a pseudo magnetic charge as it is at the origin of a demagnetizing field, which oppose to the initial magnetization $\vec{M}$. For a thin film, the magnetization will prefer lying along the plane of the film, to minimize these pseudo magnetic charges and thus the demagnetizing field. This preferential anisotropy can be described as a shape anisotropy.

Although exchange coupling is the strongest interaction (some eV/atom), they operate at small length scales, whereas magnetostatic and anisotropies interactions operate at larger length scale. Thus ferromagnetic domain pattern is determined by the competition between exchange, anisotropy and magnetostatic energies.

The magnetostatic energy favors the formation of domains, in order to close the magnetic flux inside the material. The formation of domains results in the presence of domain walls between different domains, where the magnetization is not homogeneous.

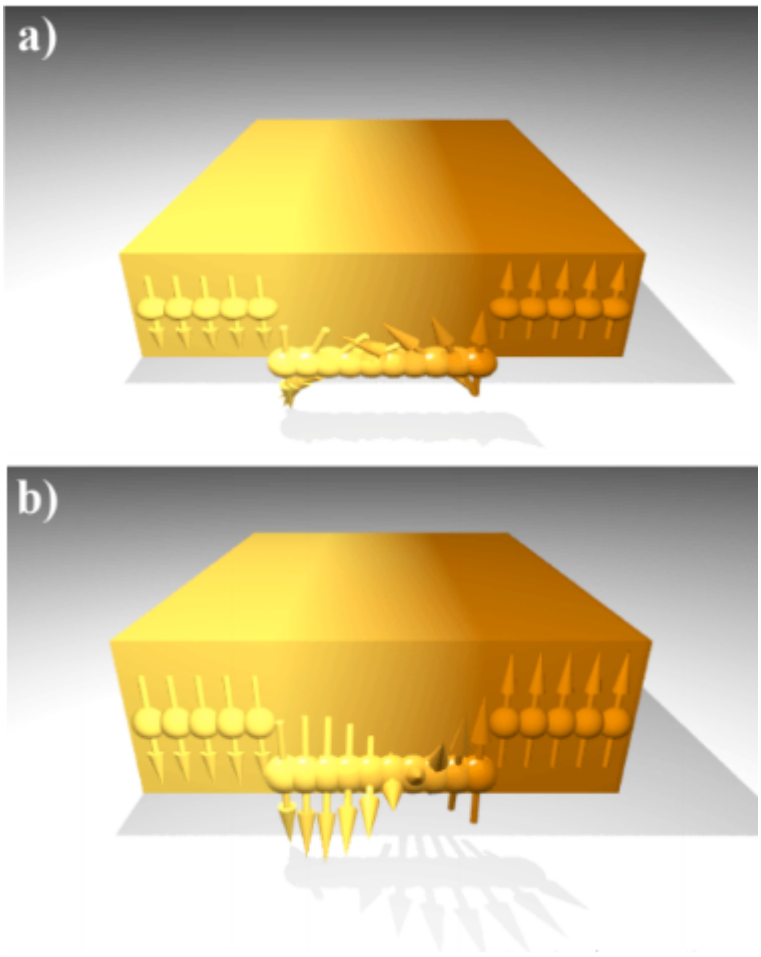

Figure 1 – Rotation of the magnetization for a Néel wall (a), and a Bloch wall (b) [10]

Because of exchange interactions it is not possible to have big disparities in the magnetization direction between two neighboring atoms, thus the change in the magnetization will be distributed along several atoms [9]. The competition between the exchange, anisotropy and magnetostatic energies will define the type of domain walls. The width and the energy of the domain walls are characteristics of the material. A strong exchange interaction favors large walls whereas a strong anisotropy favors narrow walls, as more energy is needed to move apart from the easy magnetization axes.

The module of the magnetization is supposed to be constant along all the wall, so the change of magnetization is done only by rotating the magnetization along the wall. Thus, for 180°domain walls for example, two types of domain walls are possible, Bloch

domains walls and Néel domain walls, according to the two possible axes of rotation, as shown in Fig. 1. Néel walls generate pseudo magnetic charges inside the wall, whereas Bloch walls generate pseudo charges at the surface, thus, in general Néel walls appear in thin ferromagnetic films, whereas Bloch walls appear in bulk ferromagnetic materials.

When applying a strong magnetic field, the magnetization of the ferromagnetic domains align with the magnetic field. This can be done by a growth of domains which already have their magnetization aligned or by a rotation of the magnetization of other domains. This results in a hysteresis curve when plotting the magnetization as function of the applied magnetic field. After application and then removal of the applied field, the final magnetization is not null, but has a remanent value. One needs to apply an opposite magnetic coercive field to be macroscopically demagnetize the material.

1.2 Ferroelectricity

A material is ferroelectric if it has a spontaneous electric polarization, and if that polarization can be reversed by the application of an electric field. The existence of an electric polarization implies restrictions on the symmetry of the crystal (see 1.3.2). If the operation of space inversion symmetry is contained in the point group of the crystal, the crystal can not have an electric polarization. Among the 32 crystalline point groups, there are 21 that do not have this inversion symmetry. Among these 21, 20 are piezoelectric [11]. The piezoelectricity corresponds to the appearance of an electric polarization when a mechanical stress is applied in the material. For these piezoelectric point groups, only 10 of these 20 point groups have an spontaneous electric polarization [11] and are called polar point groups. All these polar point groups are pyroelectric, that is, they present a change in the electric polarization when the temperature of the material changes, what can be

detected by a flow of charges at the surface of the crystal. Among these polar groups, some have the property of ferroelectricity (their electric polarization can be switched). This means that a ferroelectric material also has properties of pyroelectricity and piezoelectricity, which can be understood physically. As the electric polarization is related to a displacement of the ions (the polarization is coupled to the crystalline structure), anything that will influence the structure will change the value of the electric dipoles. As temperature and stress influence the structure, then a variation of temperature, or the application of a force, will generate a change in the electric polarization. It is the symmetry of the crystal which will determine the possible directions for the electric polarization.

Ferroelectric phase transition

The ferroelectric property is only present for a certain range of temperature and pressure. In particular, ferroelectrics are paraelectrics at high temperature. We then have a phase transition when the temperature decreases, from the paraelectric phase to the ferroelectric phase, for a certain temperature called the Curie temperature [12]. Two types of ferroelectric transitions can be distinguished. An order-disorder transition, where, in the paraelectric phase, the material presents a "disordered" microscopic polarization, the electric dipoles at the origin of the electric polarization are not correlated to each other, even at the microscopic level. In other words, their orientations are random. The second transition is a displacive transition, where the electric polarization does not exist in the paraelectric phase, even microscopically, and the ferroelectricity is due to the displacement of the ions when the temperature is lower than the Curie temperature. In this last case, the paraelectric phase is of higher symmetry than the ferroelectric phase. The origin of displacive transitions is usually described by a softening of a phonon mode. These two models of transitions are ideal models, in fact the transition can be a mixture of the two

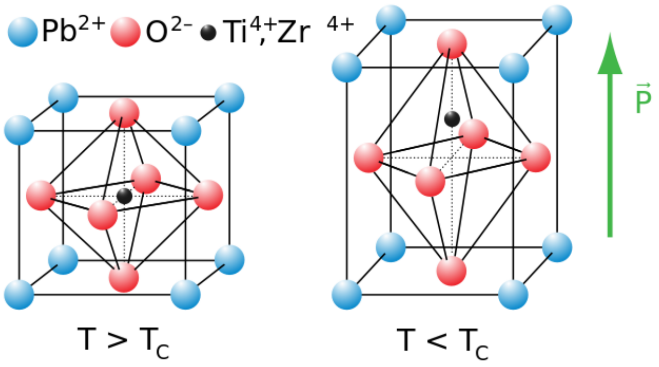

Figure 2 – Left panel: high temperature structure for a cubic perovskite. Right panel: tetragonal structure of the ferroelectric phase, as found for example in $PbTiO_3$ or $PbZrO_3$ [14].

[13].

The phase transition may be of first or second order, depending on how the symmetry of the paraelectric phase is broken. A phase transition is first order if the order parameter (here the electric polarization) appears discontinuously when the temperature becomes lower than the Curie temperature. The two symmetry groups in the paraelectric and ferroelectric phases may or may not have a group / subgroup relationship. A ferroelectric phase transition is of second order if the polarization appears gradually. Then the symmetries of the two phases are related and the symmetry group of the most ordered phase must be a subgroup of the most symmetrical phase. Below the Curie temperature, the interaction between the dipoles becomes preponderant, and tends to align the electric dipoles, creating regions where the electric polarization is homogeneous. In analogy with ferromagnetic materials, these regions are called ferroelectric domains.

Types of ferroelectrics

The electric dipoles present in ferroelectrics can have different origins. Several ferroelectric materials are perovskite oxides. Perovskites are materials with chemical formula ABO_3, the structure of which is depicted in Fig. 2. The atom at the center of

the oxygen octahedra (for the high temperature phase) is a transition metal atom. The origin of ferroelectricity in those materials (as for $BaTiO_3$) is generally a covalent bonding between a transition metal cation with empty d orbitals and an oxygen anion with fully occupied p orbitals, which favors the displacement of the cation toward the anion. The chemical bond enables the formation of electric dipole whereas the repulsion between electron clouds favors non-polar cubic structure [12]. For those materials, the origin of ferroelectricity is thus a polar distortion. When polar distortion is the driving mechanism of ferroelectricity, the materials are said to be proper ferroelectrics. Another case of polar distortion for ferroelectrics is the case of $BiMnO_3$ and $BiFeO_3$. For those materials the ferroelectricity has another mechanism, which implies another atom than the transition metal. The origin comes from the two electrons of Bi^{3+}, which are initially $2s$, but they are hybridized with p orbitals. These two electron do not participate in chemical bonding, and that have a high polarizability. They are called "lone pairs" [15]. The orientation of this pair of electrons in one direction generates the electrical polarization and is considered as a polar distortion. Thus $BiMnO_3$ and $BiFeO_3$ are also proper ferroelectrics.

The origin of improper ferroelectrics is different of a polar distortion. It can be geometric (structural transition driven), charge ordering (for electronic ferroelectric), or magnetic (magnetoelectric mechanism). For these improper ferroelectrics, their description within the Landau theory is not done as a primary order parameter, but as a secondary order parameter coupled to a primary nonpolar lattice distortion or to a magnetic order parameter [12].

An example of geometric ferroelectric is the hexagonal perovskite $YMnO_3$. The driving mechanism in this material is a rotation of the oxygen bipyramids. This rotation usually does not result in ferroelectricity as for a cubic perovskite structure this rotation

keeps the center of symmetry [12]. But in the case of the hexagonal $YMnO_3$ geometry, this rotation leads to ferroelectricity.

Long-range ordering

The appearance of an electric dipole does not always result in ferroelectricity. The long-range ordering of electric dipoles is due to the dipole-dipole interaction. But other interactions can overcome this one and can result in an ordering where the existing electric dipoles cancel each other and no macroscopic electric polarization is present. This configuration would be the electric analogous of antiferromagnetic materials, thus antiferroelectric materials [12].

1.2.1 Ferroelectric domains

The formation of the domains is governed by the minimization of the energy of the system. Domain walls cost more energy than domains. So a perfect infinite crystal would minimize its energy having all the electric moments aligned in a single domain. But if it is not infinite, an electric moment that is not parallel to the surface will generate charges on that surface. These surface charges $\sigma = \vec{P}.\vec{n}$, (given by the Maxwell's laws), with $\vec{n}$ the vector normal to the surface, will generate a depolarization field, opposite in direction to the electric moment. This field has a cost in energy, which is lowered by the existence of domains of reversed polarization. To some extent, the domains cancels the depolarization field. This depolarization field tends to stabilize the existence of a large number of domains [16].

For thin films, the importance of this depolarization field has a greater weight, so thin films generally have a higher density of domain walls. On the other hand, the

depolarization field interacts with the electric polarization of the domains, and this interaction may even cancel ferroelectricity if the film is too thin. One solution to minimize these surface charges (which generate the depolarization field) is to use two electrodes in contact with the two surfaces, which will provide a screening of the surface charges. Neutralizing the depolarization field decreases domain density because it is the depolarization field that causes the emergence of a large number of domains to be energetically interesting [12]. The ferroelectric surface charges can also been screened by other mechanisms, like by mobile charges inside the ferroelectric, or by adsorbates present at the surface or ferroelectrics [17]. As elastic energy also has a great importance, anything that influences this energy, such as the stress caused by an epitaxial growth on a crystal substrate, can also influence the morphology of the domains, or even the existence of ferroelectricity. For example, bulk $SrTiO_3$ is not ferroelectric, but it can become ferroelectric in the presence of stress [12].

Similarly to the ferromagnetic material, plotting the electric polarization as function of the applied electric field gives rise to an hysteresis curve, characterized by the value of the remanent polarization and coercive electric field. This hysteresis curve represents the alignment of the ferroelectric domains with the applied electric field, by growth or shrinking, nucleation and vanishing of these domains. Also, there is a smaller contribution of the dielectric property present for all ferroelectric materials.

1.2.2 Domain walls

In a perfect material, the area of the domain walls should be minimized, which implies that the walls should be "smooth", but with the existence of defects, the morphology may be different [16]. When an external electric field is applied, nucleation, extinction

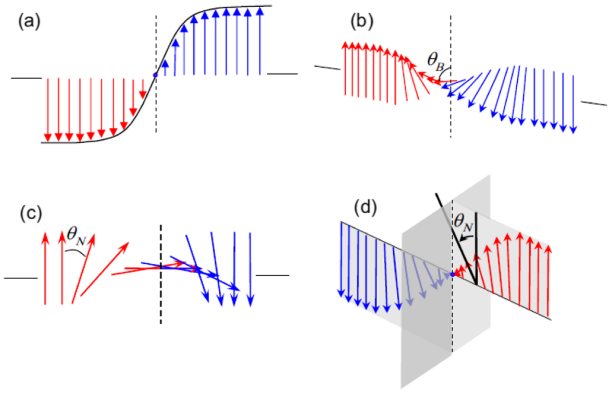

Figure 3 – a) Ising wall, b) Bloch wall, c) Néel wall e d) Ising-Néel mixed wall [16]

or motion of domain walls can happen. After applying this field, the domains are usually not the same as before applying the field. The symmetry of the point groups gives us the different possible directions for the electric polarization (section 1.3.2). For example, a rhombohedral structure, has eight possible directions [18] corresponding to the axes of rotation, on the diagonals of the pseudo cube. The polarization of two neighboring domains may then make between them an angle of 180, 71 or 109°.

For 180°domain walls with the domain wall perpandicular to the electric polarization, there is an electrostatic repulsion of the dipoles. This costs more energy but these type of domains can also be observed. Two kinds of domains can be observed, when the polarizations of both sides of a 180°wall converge their arrows, we call these domain walls "head to head". Otherwise we refer to "tail to tail" domain walls [16]. Head to head walls are generally insulating, and tail to tail generally conductive, allowing them to be observed with conducting AFM or PEEM (these microscopy techniques will be described in chapter 2). Comparing them with walls that are parallel to the polarization, it has been observed in electron transmission microscopy that these head to head or tail to tail walls are about 10 times wider than parallel polarized walls [19].

Contrary to magnetic moments, the polarization is not quantified, so it is possible

to change the amplitude of these moments arbitrarily. It is then possible to reverse the polarization along the wall without changing the orientation of the polarization but only its module. These walls are called Ising walls, and are described in panel (a) of Fig. 3. Ferroelectric materials can also display the types of walls that exist in ferromagnetism, where the polarization flips along the wall with a continuous change in the polarization orientation inside the wall. In analogy with the magnetic case, these are called Bloch or Néel walls. Finally, a mixture of more than one type of wall is also possible. Fig. 3 sketches these kind of ferroelectric domain walls. Ising walls cost less energy because the coupling between the polarization and the stress implies that generating a rotation of the electric polarization has a cost of elastic energy. Another reason is that a component perpendicular to the plane of the wall will generate charges [16]. The reference [16] presents a whole discussion about magnetic and ferroelectric domain walls, including their potential use as basic bricks of new devices.

1.3 Multiferroicity

So far we have made a short review of magnetism and ferroelectricity. These are two of the most employed ferroic properties in technological applications. In this section we will introduce the materials that present both magnetism and ferroelectricity. We will recall that those are not the only ferroic properties, but as a matter of fact, within the scientific community there is a misuse of the term *multiferroic material* assuming it present magnetic and ferroelectric properties. For the most of this work, this will be the use we will made of the term *multiferroic*: a material or heterostructure that presents both some (anti)ferromagnetism and ferroelectricity.

1.3.1 Ferroic properties

Ferroelectricity and ferromagnetism are only two of the four primary ferroic properties, the other two being ferrotoroidicity and ferroelasticity. These four properties have in common a phase transition with the emergence of an order parameter and of domains, where this order parameter is homogeneous. This order parameter is the polarization (as we have seen), a magnetization, a toroidal moment, and a strain tensor for ferroelectricity, ferromagnetism, ferrotoroicity and ferroelasticity respectively. For ferroelectricity, ferromagnetism and ferrotoroidicity, their order parameters have at least two possible directions, and the application of an external field, corresponding to the conjugate variable of the order parameters, can change these directions. The conjugate variable is the electric field for ferroelectricity, the magnetic field for ferromagnetism, the source field (corresponding to the vector product of the electric field and the magnetic field) for the ferrotoroidicity , and the stress tensor for ferroelasticity. We then have similar hysteresis curves for these four ferroic properties, plotting the order parameter as a function of the conjugate variable of the order parameter.

Multiferroic materials are materials having at least two primary ferroic properties. Recently, this definition was generalized to the presence of antiferromagnetism or ferrimagnetism in addition to ferromagnetism[20].

There are two types of multiferroics, the multiferroics in a single phase, and the composite multiferroics. These last ones are system where two single ferroic materials are put together and their resulting interaction leads to multiferroicity. They normally are in the form of alloys of such materials or heterostructures grown on a crystalline substrate.

There are also secondary ferroelectric properties, such as piezoelectricity (the

appearance of a moment of polarization when we apply a stress or the appearance of a deformation when we apply an electric field) or magnetostriction (the appearance of a magnetic moment when we apply a tension or the appearance of a deformation when we apply a magnetic field).

Landau's theory allows us to understand that these secondary ferroic properties correspond to a coupling of primary ferroic properties [21].

1.3.2 Symmetry

We will describe the phase transitions with some more details. As we have already seen for ferroelectrics, at high temperature the material has a phase of high symmetry, which is called "prototype". At the transition temperature, a spontaneous symmetry break occurs. The ferroic phase has a lower symmetry than the "prototype" phase. The new point group of the ferroic phase is in general a subgroup of the point group of the phase of the prototype [13], [12]. We characterize the phase transition of a multiferroic by first writing the point group of the prototype, followed by the letter F (for Ferroic), and the point group of the ferroic phase. For example: 42m1'Fmm2 [22, 23]. The symmetry of point group can give us several informations. Now we will focus on the ferroelectric and ferromagnetic properties, which are important for applications. According to the Neumann principle, the macroscopic properties have at least the symmetries of the point group of the ferroic phase [18].

The polarization moment is invariant under time inversion symmetry operation but is non-invariant under space inversion (it means that if we apply the inversion operation of the space, the polarization moment must be reverted). In contrast, the magnetization moment is invariant under the spatial inversion symmetry operation but

is non-invariant under time inversion.

Thus each time the point group of a ferroic phase is invariant by spatial inversion, this phase can not be ferroelectric. And each time the point group of a ferroic phase is invariant by time inversion, this phase can not be ferromagnetic [20]. With the symmetries of the point group of the ferroic phase we can predict the possible orientations of magnetic and electric moments [23]. For example, if the system has a symmetry operator of the type mirror plane, then P will be contained in the plane of the mirror, and M would be perpendicular to this plane.

The joint symmetries of the prototype and ferroic phase may give us even more information. First we introduce the concept of orientation state, which is one of the possible states that a ferroic material can assume without the application of its conjugated external field [23]. For example, for a ferromagnetic material, the magnetization direction of each magnetic domain in remanence would be an orientation state. We can find all possible orientation states by applying to an arbitrary orientation state a set of symmetry elements that belong to the point group of the prototype but do not belong to the point group of the ferroic phase. The number of possible orientation states is the number of elements of symmetry of the point group of the prototype divided by the number of elements of symmetry of the point group of the ferroic phase [23]. If the orientation of the order parameter is different in all these obtained orientation states, we say that the order parameter has a distinction of full orientation states.

To check this, we must first know one possible orientation of the order parameter. The symmetries contained in the point group of the ferroic indicate the possible orientations, as we have already seen. We choose a direction and then apply this set of

symmetry operations, contained in the point group of the prototype and not in the punctual group of the ferroic [23] (as to obtain the states of orientations). If all directions are different, the system has *complete distinction*, if not all are different, it is said of *partial distinction*. If all are equal and the order parameter is different from 0, the system is said of *null distinction* [20]. The distinction for order parameters can give us interesting information. For example, if polarization and magnetic moment have two complete distinction, it means that if we change the polarization moment orientation with an electric field, we will also change the orientation of the magnetic moment. In this case, the system present complete coupling. On the other hand, if one of the two has zero distinction, it will not be possible to change its orientation.

But symmetries analysis do not give information about the amplitude of their order and their couplings. This requires understanding the coupling mechanisms, which will be discussed in the next section.

1.4 Magnetoelectric coupling

In this section we will recall the main magnetoelectric coupling mechanisms for the two possible types of multiferroic structures, single phase multiferroics and multiferroic heterostructures.

1.4.1 Single phase multiferroics

Many perovskites are ferroelectrics (for example $BaTiO_3$ or $PbTiO_3$), and also many are ferromagnetic (like $YTiO_3$). But there are few perovskites having the two properties [12]. The magnetic order is generally due to the partial filling of the d shell of the transition metal. However, in most perovskites, the ferroelectric order needs an

empty d shell, because it allows a favorable state of a covalent bond with an oxygen [24]. This fact is due to a hybridization of the d shell of the transition metal with the p shell of the oxygen. We will have then a displacement of that transition metal towards the oxygen. This explains why in general one can not find a perovskite with both properties.

Multiferroics in single phase are classified according to their origin of ferroelectricity. If the origin corresponds to a magnetic order, they are classified as type II multiferroics. For any other origin, they are classified as type I [25]. Single phase multiferroicity has several origins [15, 25].

1.4.2 Multiferroic heterostructures

Because of the difficulty to find multiferroic magnetoelectrics in single phase with both strong ferroic properties (high curie temperature, magnetization and electrical polarization) and strong magnetoelectric coupling, other well studied multiferroics materials are multiferroic heterostructures. We will present here mechanisms for materials with an existing interface between ferromagnetic and ferroelectric materials. The quality of the interface between the two materials will determine the magnetoelectric coupling. Thus most of multiferroic heterostructures correspond to deposited thin films by sputtering or pulsed laser deposition.

1.4.2.1 Carrier mediated and bonding magnetoelectricity

At the interface of a ferroelectric with another material, surface charges appear at this interface on the ferroelectric side ($\vec{P}.\vec{n}$, with $\vec{n}$ the vector normal to the interface). If the other material in contact is a ferromagnetic metal, those surface charges in the ferroelectric will lead to a spin dependent screening in the metal part on the first layers

near the interface. This effect of ferroelectric charge screening is also named ferroelectric field effect.

This spin dependent change in the band structure, corresponding to a redistribution of the electrons over the magnetic orbitals, may lead to a change in the magnetic properties (magnetocrystalline anisotropy, microscopic magnetic value, or may even results in a phase transition) for those first layers of atoms. Similarly, hybridization of orbitals at the interface, which also influence the spin splitted band structure, can also lead to a change in the magnetic properties of the ferromagnet or even induce magnetization into the ferroelectric [26].

1.4.2.2 Strain transfer

For a thin magnetic film grown on a ferroelectric substrate, the strain imposed by the substrate in the thin film can strongly influence its magnetic properties due to inverse magnetostriction effect. Actually, there is no need to have a ferroelectric and ferromagnetic material to have strain induced magnetoelectricity. For example a piezomagnetic material deposited on a layer of a piezoelectric, could reach large values of magnetoelectric coupling coefficient due to the elastic coupling. The coefficient will only depend on the piezoelectric and piezomagnetic coefficients and on the quality of the surface. The advantage of using a ferroelectric material is that the stress does not disappear without application of electric field, and a change in the electric polarization by application of an electric field may lead to a simple way to change the applied stress. Whereas carrier mediated and bonding magnetoelectricity mechanisms are efficient only in the first layers near the interface, strain transfer can be efficient on a much larger number of layers, depending on the quality of the deposited film.

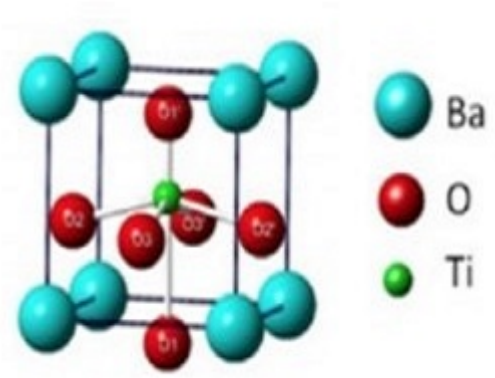

Figure 4 – Tetragonal BTO unit cell

1.5 Thin iron layers on $BaTiO_3$: some previous results

The main results from this PhD work are on the understanding of the magneto-electric coupling at the interface between an iron thin film on barium titanate substrate. This section gives an introduction to this system, reviewing part of the results that can be found on the literature and can be of help to analyze the data we will present on chapter 4.

1.5.1 $BaTiO_3$ ferroelectric domains

$BaTiO_3$ is a cubic perovskite above around 393 K (120°C), with Ti^{4+} ion in the center of an oxygen octahedra. The Ti^{4+} are also in the center of the unit cell and O^{2-} ions at the centers of the unit cell faces. Ba^{2+} ions occupy the corners of the unit cell. A transition from cubic to tetragonal phase occurs decreasing the temperature to 120°C, tetragonal $BaTiO_3$ unit cell is elongated along one axis of the unit cell, with an opposite displacement of the Ti and O ions along this same axis as it can be seen (exaggerated) on Fig. 29. Those ionic displacements leads to ferroelectricity, the electrical polarization reaching up to 26 $\mu C/cm^2$. Tetragonal to orthorhombic transition is observed for temperature below 275 K (2°C). For the tetragonal phase, the polarization can only

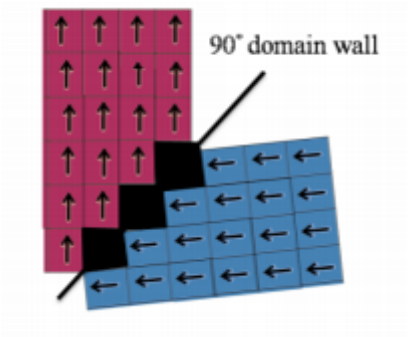

Figure 5 – Deviation of the lattice for perpendicular domains due to tetragonality [28]

be along one of the 3 axis of the unit cell and there is only 6 possible directions for the polarization. The characteristics of the domain walls separating two domains of different polarization are defined by electric and stress boundary conditions, implying no charges at the domain walls and a continuity of the lattice strain.

Two types of domain walls are present for tetragonal ferroelectrics, 180°and 90°domain walls. Two parallel domains with opposite direction result in 180°domain walls at the interface. As the two domains have the same lattice strain, no restriction conditions are needed for the shape of the wall, and watermark like patterns may appear [27].

For two perpendicular domains, a domain wall direction at almost 45°from the electric polarization of each domain enables to reduce lattice mismatch and to have a neutral domain wall.

As the unit cell is tetragonal, there is a slight deviation of the lattice to reduce lattice mismatch, so that the angle between the two elongated axis (and thus the two polarizations) is not exactely 90°(it is actually 90.62°) [28], as can be seen (exagerated) in Fig. 5. Indeed, lattice parameter for the tetragonal phase is 403.6 pm, along the elongated axis and 399.2 pm for the 2 others, so the tetragonality of the unit cell is close to 1%.

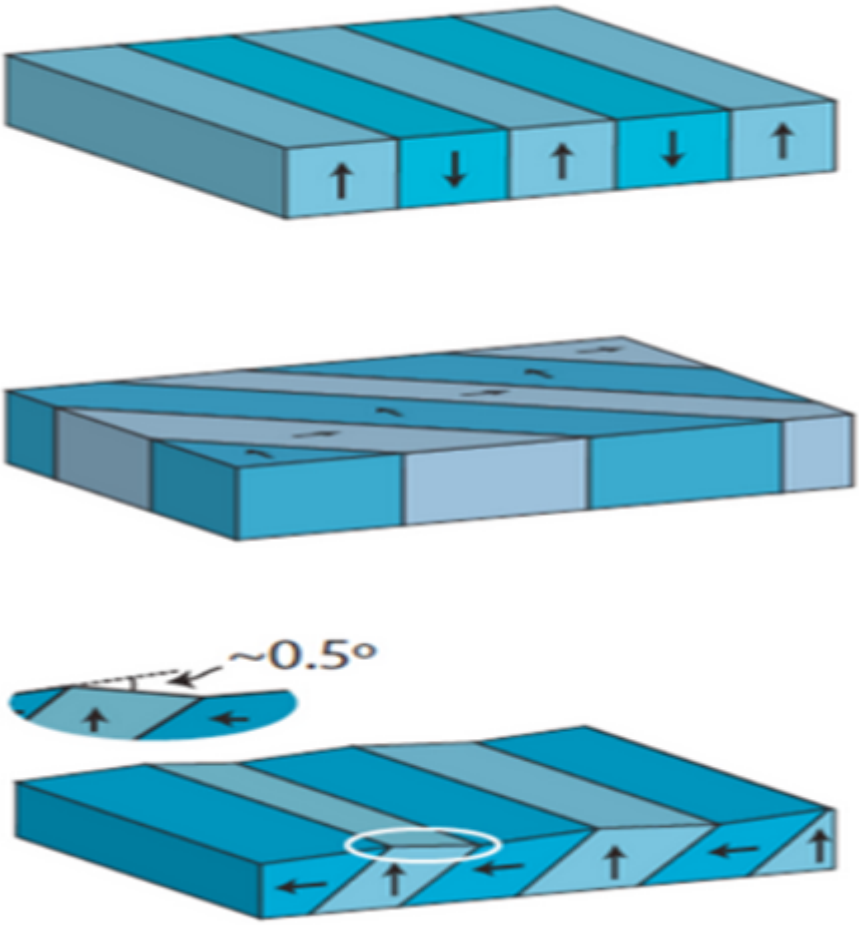

Figure 6 – Types of domain configuration for tetragonal ferroelectrics [10]

The need of neutral walls restricts the possible direction for the polarization (so that the projection on the normal to the interface of the difference of electric polarization is zero, $\Delta\vec{P}.\vec{n} = 0$), although charged domain walls are sometimes present.

For a $BaTiO_3$ single crystal cut along one of its main axis, the ferroelectric domains can be in-plane and are denominated $a1$ and $a2$ domains, or out-of-plane c called domains. Each kind of domain follows one of the three orthogonal main axis of the crystal, and thus $a1$ and $a2$ in plane domains have polarization perpendicular to each other. Fig. 71 illustrates these kind of domains in $BaTiO_3$ single. Fig. 71-top shows the configuration

for c domains of opposite polarization. The stripe like domains shown are possible, but in this case one can also have more irregular, watermark patterns. Fig. 71-middle shows a domain configuration for a succession of $a1/a2$ domains. In this case the stripe like pattern is expected to minimize the domain wall and elastic energies. Fig. 71-bottom shows a domain configuration for a succession of a/c domains, i.e., in and out-of-plane domains. All these configurations respect the requirements that we saw before (for minimization of stress and neutral domain walls). For the case depicted on the bottom figure, we see that the tetragonality results in a rough topography at the surface, characteristic of a/c domains configuration.

The $BaTiO_3$ single crystals we used in this thesis were cut to have surfaces (100) or (001). The surface of (100) $BaTiO_3$ single crystals has generally in-plane domains ($a1$ and $a2$), whereas (001) cut usually shows all domain types. But after annealing, due to the formation of oxygen vacancies at the surface, in-plane domains are stabilized, even for a (001) $BaTiO_3$ crystal.

1.5.2 Fe on BTO

The $Fe/BaTiO_3$ system, with a thin Fe layer deposited on a $BaTiO_3$ substrate, is a system showing magnetoelectric coupling. Fe and $BaTiO_3$ have a good lattice match, which enables the Fe epitaxial growth, with an in-plane Fe [110] $\shortparallel$ $BaTiO_3$ [100] alignment. Assuming a full strain transfer in the case of epitaxial growth, out-of-plane c ferroelectric domains impose a compressive strain on Fe in-plane lattice parameters of 1.6 %. Fig. 7 shows the stress induced on Fe by in-plane and out-of-plane $BaTiO_3$ domains [29]. As shown in Fig. 8, on a TiO_2 terminated $BaTiO_3$, the Fe atoms grow upon the oxygen, whereas for BaO terminated $BaTiO_3$, the Fe atoms grow on oxygen and barium [30].

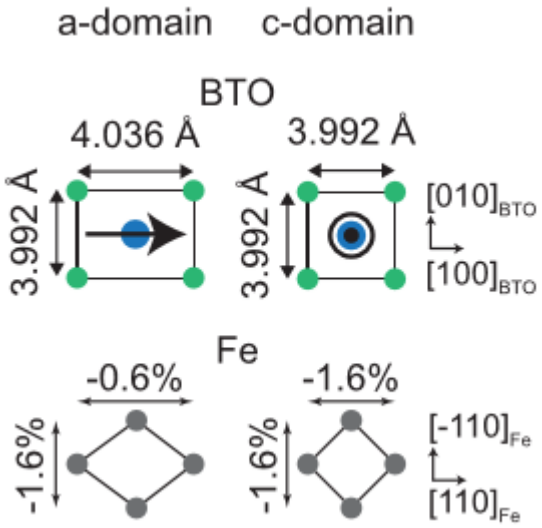

Figure 7 – Stress induced on Fe in-plane lattice parameters when it is grown on in-plane $BaTiO_3$ domain and out-of-plane $BaTiO_3$ domain [29]

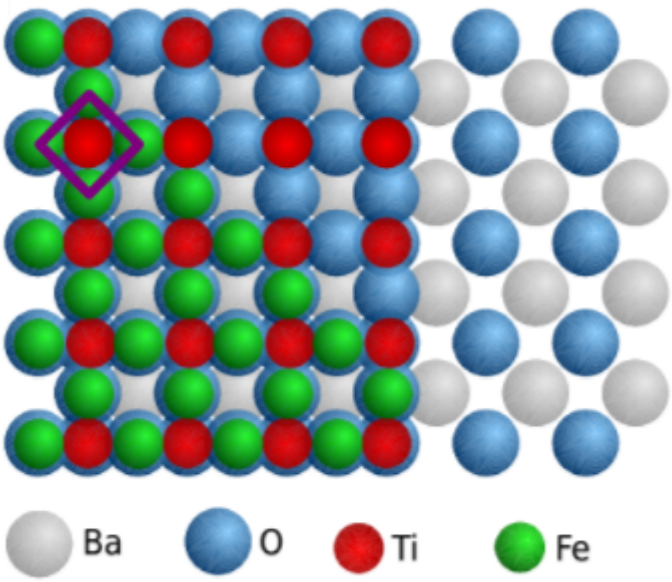

Figure 8 – Fe growth on $BaTiO_3$, Fe is upon Ba and O for BaO terminated $BaTiO_3$ and upon O for TiO_2 terminated $BaTiO_3$ [30].

Theoretical calculation showed that for Fe grown on $BaTiO_3$ with ferroelectric out of plane domains, orbital and charge coupling resulted in a change in magnetic properties for the first layers of Fe grown on *up* or *down* $BaTiO_3$ domains and also resulted into induced magnetic moment in the Ti and O ions at the interface [26]. Ref.[31] also showed a tunnel magnetoresistance dependence on $BaTiO_3$ *up* or *down* polarization for the Fe/$BaTiO_3$ system, with a 10% difference in Fe magnetization at the interface.

In [29], the authors grew 20 nm of Fe at 573 K (300°C) by molecular beam epitaxy on a $BaTiO_3$ (001) single crystal, with a capping layer of 5 nm of Au. Notice that the growth temperature is well above the tetragonal-cubic transition of $BaTiO_3$. After decreasing the temperature to room temperature, the cubic to tetragonal $BaTiO_3$ phase transition induces a different strain imposed on Fe according to the $BaTiO_3$ ferroelectric domain laying above it. By means of MOKE microscopy, they showed that this strain transfer resulted in a strong induced magnetoelastic anisotropy in Fe, sufficient to pin the magnetization of Fe. For in-plane $BaTiO_3$ domain, the Fe magnetic easy axis was pinned to the direction perpendicular to the $BaTiO_3$ ferroelectric domain direction, whereas for out-of-plane $BaTiO_3$ ferroelectric domains, the Fe magnetization direction was pinned to the [100] or [010] (or equivalent) Fe axis, corresponding to the [110] or [1-10] or equivalent $BaTiO_3$ axis, due to a biaxial induced magnetic anisotropy. Those [100] or [010] Fe axis also correspond to the magnetocrystalline anisotropy direction of bcc Fe. The ferroelectric domain pattern is thus imprinted into the magnetic domain pattern by strain transfer.

1.6 Objectives of this work

This thesis can be outline in two main goals: i) to grow and characterize ferroelectric and magnetoelectric thin film systems; ii) to explore the potential of synchrotron based

photoemission electron microscopy in the investigation of magnetoelectric heterostructures, in particular taking advantage of the intrinsic element sensitivity of soft X-rays spectroscopies. These two main goals are reflected in the two results chapters presented in this thesis.

Chapter 2

Experimental Methods

Along the work of this thesis we have been involved in the growth and characterization of the samples we have worked on. In this chapter we describe the techniques needed to characterize the properties of these samples. The characterization always starts with the determination of their structural, morphological and compositional properties. These are the first indications of the sample quality. Those that present the best results during the initial characterization are selected to pass through further tests to determine their magnetic and ferroelectric properties. Finally, in some cases we also investigated the electronic structure of the sample. One of our goals was to correlate the macroscopic properties of the samples with their electronic structure.

In the following sections we briefly describe the experimental techniques employed during this work.

2.1 Sputtering

We have used the sputtering technique to grow our first ferroelectric films on silicon substrates. These were mostly "case studies" samples that gave us some experience

on the technique. As ferroelectrics are intrinsically insulators, whereas the electrodes are metallic, we end up using two variations of this deposition system, each one suitable for different transport properties of the element under evaporation. In the following we describe the sputtering thin film deposition technique and give some information about the growth of our samples.

2.1.1 Direct Current sputtering

In Direct Current (DC) Sputtering, thin films are grown by condensation on a substrate of particles ejected from a target by a plasma. Vacuum of the order of 10^{-5} Pa is necessary to get a minimum of contamination and to create this plasma. A plasma is a situation where neutral gas atoms, ions, electrons and photons exist in a near balanced state simultaneously [32]. To create a plasma for sputtering an inert gas (often argon) is used, with usually a pressure between 100 to 10,000 Pa [33]. The argon atoms are ionized and then accelerated toward the target by an electric potential between the target (which get a negative potential and is thus the "cathode", as we can see it as a passive device) and the rest of the equipment (which includes the substrate) [32]. Those ions can therefore collide with the target atoms and eject them by momentum transfer. Then those ejected atoms travel in a straight line and may reach the substrate if they do not collide with something else, and those "adatoms" condensate in the substrate. If the ions energy is sufficient they can set off collision cascades, leading to the ejection of the target atoms and also ejection of secondary electrons, which may ionize other argon atoms and thus contribute to maintain the plasma. Other secondary processes can occur, an important one is the production of oxygen anions of high energy, in case of the use of oxygen gas to form the plasma. Those anions can influence a lot the structure of the films, as we will

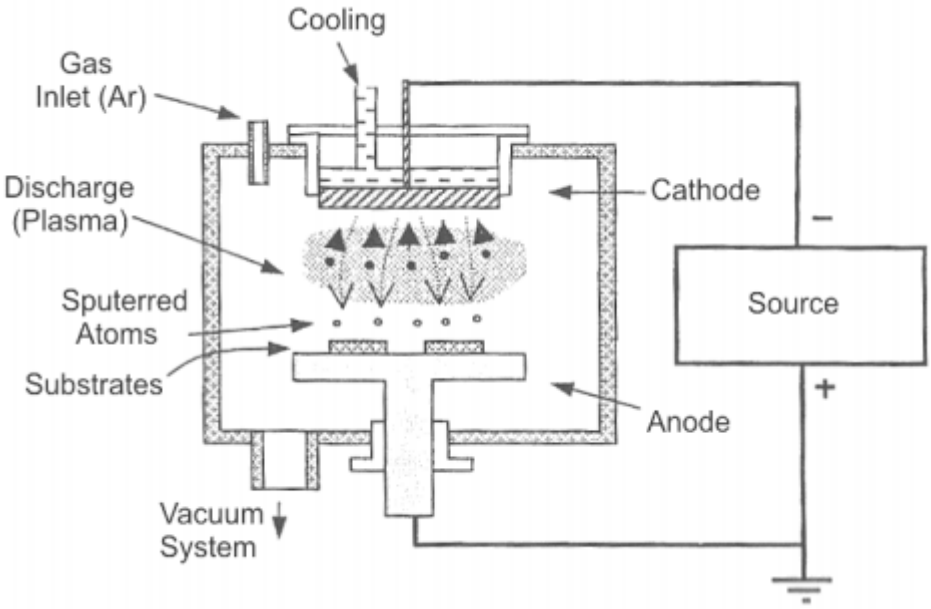

Figure 9 – Schematic of DC sputtering [34]

explain below. Collision of an electron with an argon cation results in the emission of a photon, whose energy is characteristic of the plasma color.

Fig. 9 shows a schematic configuration of DC sputtering. The positive argon ions, while colliding with the target, can be trapped in it, and this brings a positive charge in the target if the target is not conductive. This positive charge can prevent the collision of other positive ions. That is why in DC sputtering the target must be conductive, to neutralize those charges. The utilization of a reactive gas, sometimes needed to get the desired stoichiometry, as the use of oxygen gas to grow oxides, can be a problem as it can react with the surface of the target and make it insulating. But as long as the partial pressure is low this effect should not appear. Without using reactive gases the stoichiometry of the film should be the same that the target one. Indeed, even if the probability of being sputtered is different for each element of the target, this fact is compensated as only the atoms present in the surface can be sputtered. So if one element is more sputtered it will be less present in the surface, which equilibrate the sputtered

rates of different elements.

However, the stoichiometry can change a little because of the volatility of one element if the substrate is maintained at high temperature, or because of resputtering. Indeed, energetics anions can be produced from secondary processes (like O_2^-), and may be accelerated toward the substrate and induce resputtering, and the difference of resputtering rate for each element is not compensated [35]. In this technique, a lot of electrons can be lost (they are not used to ionize argon atoms) which leads to low deposition rate [36], but this low ionization efficiency can be easily improved.

2.1.2 DC Magnetron Sputtering

To overcome the low ionization efficiency it is possible to create a magnetic field near the target in order to constrain electron motion near this target, thus improving considerably the probability of ionization of argon atoms and thus the collision of argon ions with the target. This technique is called magnetron sputtering [36]. The magnetic field can be confined over a very small region above the target or can be confined over a bigger region where the substrate can be placed. These techniques are respectively balanced and unbalanced magnetron sputtering [36]. The balanced magnetron sputtering decreases the probability of energetic ion (electron and anion) collisions with the substrate. Energetic anion bombardment can cause resputtering, which can be harmful for the stoichiometry and can introduce defects on the film, but on the other hand, electron and anion collisions enable to increase the energy of the adatoms, which is also important for a crystalline growth, as we will see below.

2.1.3 RF Magnetron Sputtering

RadioFrequency sputtering uses an alternative potential (whose frequency is in the radiofrequency range) between the target and the rest of the equipment instead of a constant one. Ar cations can be trapped into the target and become a positive charge for insulating targets. But with RF sputtering, when the potential in the target get positive, the secondary electrons just emitted before are attracted by the target and can collide with Ar cations trapped in the target and neutralize the charge. As a continuous component is added to the AC signal, the target get positive for a very short time [33] (much less than half a period), so that positive ions who are heavier should not have time to reach the substrate. With RF sputtering it is therefore possible to sputter insulating targets. On the other hand, for the same deposition rate, the cost of RF sputtering is higher than the DC one, partly because an impedance adaptation is needed to avoid reflexion of the power in the AC source, which lower the efficiency. RF Sputtering, like DC Sputtering, is also generally used with a magnetic field, and is therefore RF Magnetron Sputtering.

2.1.4 Sputtering Conditions of some perovskites

As we saw in the previous part, sputtering parameters influence a lot the structure of the film. Here we will see what are the conditions generally used to growth two perovskites, $SrRuO_3$ (SRO) (used as electrode) and $BiFeO_3$ (BFO) (multiferroic), as they are the two most important materials we tried to grow until now.

Growth of $SrRuO_3$ films

$SrRuO_3$ (SRO) is an orthorhombic distorted perovskite at room temperature. It is a commonly used electrode to grow multifunctional oxide films. It possesses a good resistivity ($280\mu\Omega$.cm for bulk, [37]), and good lattice match with other distorted perovskite. Using SRO enables to grow other distorted perovskite (like $BiFeO_3$) epitaxially with less leakage current and fatigue than with other metallic electrodes. This can be understood by the quality of the interface, which shows fewer defects like oxygen vacancies than with metallic electrodes, and those defects are known to increase leakage current and fatigue [38]. A good quality of the interface also provides a good screening of the polarization charges [39], which is important for ferroelectric properties.

However, energetic ionic bombardment on the substrate during sputtering deposition is a problem for growing SRO, and SRO thin films are often grown by PLD or MOCVD. With sputtering, the out of plane lattice parameter and unit cell volume are larger and the resistivity is higher (and with a negative temperature dependence) than with other methods [40]. Ref. [41] also showed that Sr ions switched place with Ru ions in SRO films because of sputtering damage. But it is possible to reduce this damage. In Ref. [37], they showed that it was possible to grow good quality SRO films with an increase of the pressure. They used in plane RF sputtering, a power of 50 W, a temperature 823 K, a distance between target and substrate of 12 cm and a Ar:O2 ratio of 4:1. With a pressure of 27 Pa (close to 0.2 mTorr) they managed to growth 60 nm SRO on (001)$SrTiO_3$ with a resistivity of $250\mu\Omega$.cm (close to the single crystal one), and with a positive temperature dependency (which corresponds to a metallic behavior). It is also possible to use 90°-off axis sputtering [42].

$SrTiO_3$ substrate is often choose to growth perovskite because it shares the same structure and similar lattice parameter with a lot of other perovskite crystals. But it is also possible to use other less expensive substrate. In Ref. [43], epitaxial growth of SRO thin films by RF sputtering on Pt(111)/γ-Al2O3(111)nSi(111) was observed. They used RF power of 15W, 1 Pa pressure with an Ar:O2 ratio of 4:1, and a deposition temperature of 973 K. On Ru/SiO2/Si by RF magnetron sputtering the SRO structure was observed [44] but other phases corresponding to oxided Ru at the interface with Ru also appeared. Finally, in Ref. [38], SRO was deposited on SiO2/Si with DC magnetron sputtering. The SRO was found polycristalline but, for a set of parameters, a good resistivity of 440 μC.cm was found. 15 mn preheating time, 823 K deposition temperature (or more), lower deposition rate and 20-30 per cent oxygen ratio were found to decrease the resistivity.

Growth of $BiFeO_3$ films

Bulk $BiFeO_3$ (BFO) is a rhombohedral distorted perovskite at room temperature [45], but in thin film it has often been observed to have a monoclinically distorted rhombohedral structure [46], although it can also have the bulk structure [45], or tetragonal structure [47], [48]. BFO is a room temperature multi-ferroic with coexisting anti-ferromagnetic, ferroelectric and ferroelastic orders. A significant enhancement of magnetization compared with the bulk has also been observed [46], and is attributed to the presence of oxygen vacancies in thin films. The polarization lies in the [111]pseudo cubic direction, and the anti ferromagnetic plane (G type) is located perpendicular to the polarization direction. For bulk, BFO crystals with high electrical resistivity have been produced only in 2007 [49], resulting in low leakage current, which allowed to measure a

value of electrical polarization of about 100 $\mu C/cm^2$, in agreement with thin films values and theoretical calculations [49]. BFO thin films present a value of electric polarization close to the bulk value, although it can be lower due to the presence of other phases or if the film is polycristalline. At 80K a thin film grown by PLD also observed a polarization close to 166 $\mu C/cm^2$ [50] (and 110 $\mu C/cm^2$ at room temperature). $BiFeO_3$ stoichiometry is difficult to obtain. Usually, growth of BFO is done with BiFeO3 target enriched with Bi, to compensate preferential resputtering of Bi [51] and volatilization of Bi on the film at high temperature. Resputtering effect is more pronouced with O_2 gas as previously explained [35]. However, Ref. [52] mentions a deficit in Fe.

With a non stoichiometric deposition, various other phases can be observed, like Bi_2O_3, $Bi_{24}Fe_2O_{39}$, $Bi_{25}FeO_{40}$, $Bi_2Fe_4O_9$ and Fe_2O_3. To obtain the pure BFO phase, adjustment of pressure and temperature must be done. In Ref. [53] (where PLD deposition was used), it was observed, in relation to the optimized conditions where only $BiFeO_3$ phase was present, that increasing temperature or decreasing the pressure lead to the presence of the Fe_2O_3 phase, whereas decreasing temperature or increasing the pressure lead to the presence of the Bi_2O_3 phase. In spite of the difficulties to get a stoichiometric deposition, good quality BFO films can be obtained by sputtering. In Ref. [54], off-axis sputtering was used to decrease the damage effect of ionic bombardment. With a 5 per cent excess of Bi, BFO was epitaxially deposited at 963 K on 100 nm SRO on two (100)STO substrates, one with 0,8° miscut and one with 4° miscut. For the deposition with the former, the secondary phase Fe_2O_3 was found whereas for the latter, only the BFO phase was found, it is believed that a high miscut degree helps incorporating and retaining Bi, which could explain why Fe_2O_3 is only found in the lowest miscut [54].

In Ref. [55] it was also observed the epitaxial deposition of pure BFO phase.

They used a temperature deposition of 883 K, a ratio Ar:O2 of 2:1, and a total pressure of 0.5 Pa. Polycristalline pure BFO phase also observed with RF magnetron sputtering, using 7 Pa, a Ar:O2 ratio of 4:1, and a deposition temperature of 923 K [56], and in Ref. [57], BFO thin films were deposited on SRO buffer layer by RF sputtering with 220 Watts, 953 K, deposition rate of 33 pm/s, 133 Pa, 200sccm Ar, 30 sccm O_2, on SRO/Pt/TiO_2/SiO_2/Si.

2.2 Scanning microscopy

Scanning probe microscopy comprises a very broad range of techniques that allow one to investigate in details the morphology, magnetism, electric polarability among other properties of surfaces. The first scanning probe technique was the scanning tunneling microscopy (STM), which since its start in 1981 brought a wealth of information about the surface of metals and semiconductors. In the next sections we describe the atomic and piezoresponse force microscopies, which have been routinely used to characterize our samples.

2.2.1 Atomic force microscopy

Atomic Force Microscopy (AFM) uses a very thin tip whose radius of curvature is of some nanometers, fixed to a cantilever with tens of microns in length, whose mechanical properties, such as stiffness constant and resonance frequency, can be precisely determined. The AFM technique is based on the interaction between the tip and the atoms on the surface of the sample. The interaction can have several origins, like Van der Waals force, electrostatic and magnetic. The different interaction sources can be in-

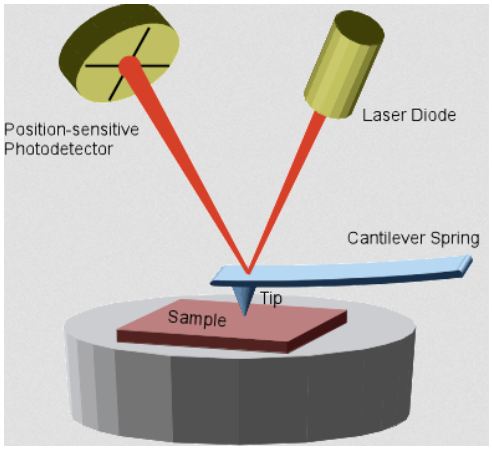

Figure 10 – Sketch of deflection measurement in an atomic force microscope [58].

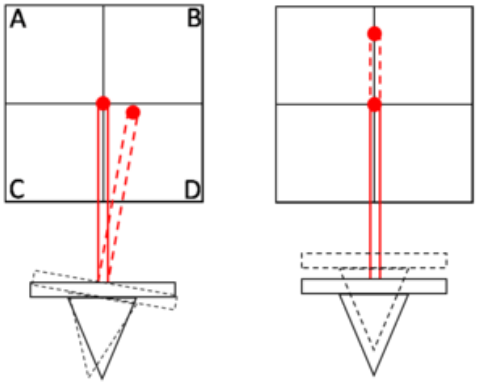

Figure 11 – Lasers position in the photodiode [59].

tensified by a suitable fabrication of the tip. Contrary to tunneling microscopy, it is not necessary to have a conductive sample for AFM. The resulting forces will generate a tip movement detected by the deflection of a laser beam reflected on the cantilever. The laser source is fixed and its deflection, after reflection on the cantilever (Fig. 10) is detected by a set of 4 photodiodes mounted in quadrant. The tip can have two types of displacement: a vertical movement which is usually the only one used for the AFM, and a twisting movement which is interesting for piezoelectric force microscopy (PFM) as will be shown in section 2.2.3. A vertical movement will imply a laser deflection as shown in Fig. 11 on the right. A torsional motion will imply a movement almost in the perpendicular direction, as shown in Fig. 11-left. The 4-photodiode system allows quantifying these movements and separating them. The reference position is at the center of the photodiode array. With the

conventions of Fig. 11, the vertical signal is given by $((A+B)-(C+D))/(A+B+C+D)$ and the lateral signal by $((B+D)-(A+C))/(A+B+C+D)$, each photodiode giving a signal proportional to the distance between the center of the array and the position of the laser in that photodiode.

There are several modes to obtain sample topography. In contact mode, the tip is approximated until it has repulsive interactions, and then to keep constant the distance between tip and sample, the position of the cantilever is adjusted to compensate for the tip deflection (the laser should always be in the center of the photodiodes). This mode is more accurate but is more likely to damage the tip or sample.

In the tapping mode, we oscillate the cantilever at a fixed frequency. The feedback here is made on the amplitude of the oscillations, the height of the cantilever is then adjusted to leave constant the amplitude of these oscillations. This mode allows to leave the tip farther away from the sample, which is safer. Depending on the samples and tips the lateral resolution can range from 0.1 to 10 nm.

2.2.2 Conducting Atomic Force Microscopy

Conducting atomic force microscopy (c-AFM) is a variation of atomic force microscopy. In this case the tip is covered with a metallic layer and the system measures the electrical current passing between the tip and the lower electrode below the sample (as for tunneling microscopy). To do this, a negative voltage is applied below the sample and one measures the electric current given by the electrons coming out of the sample through the tip. This measurement can be done in parallel with the standard AFM. It allows to obtain the topography and conductivity of the sample. It has been successfully used to investigate the ferroelectric domain walls, and it is one of the techniques that allowed to

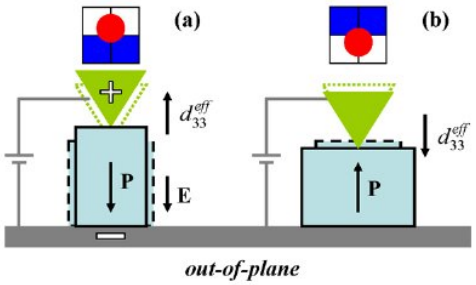

Figure 12 – Position of the laser in the photodiodes, vertical movement [61]

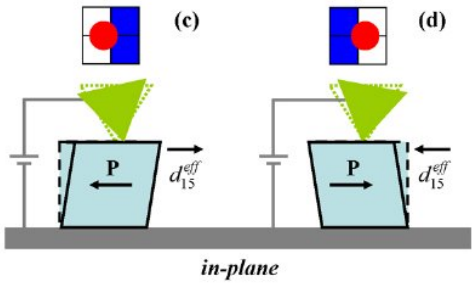

Figure 13 – Position of the laser in the photodiodes, lateral movement [61]

confirm that *tail-to-tail* walls are conducting [60], as mentioned in section 1.2.2.

2.2.3 Piezoresponse force microscopy

Piezoresponse Force Microscopy (PFM) allows to determine the piezoelectric properties of the sample. In this case a voltage is applied to the sample surface through a conducting tip. If the sample is piezoelectric, this voltage will lead to a mechanical deformation under the tip. Strictly speaking, this is the inverse piezoelectric effect, where the application of a electric field induces a mechanical deformation. As the feedback loop keeps the tip at constant distance from the sample, one can detect the piezoelectric deformations by measuring the height of the tip. As ferroelectrics are always piezoelectrics by symmetry (section 1.2), PFM is widely used to visualize ferroelectric domains. The mechanical deformation of the ferroelectric due to the inverse piezoelectric effect is very small, what makes the expected signal very small too. To overcome this fact and get a measurable signal, the applied voltage is AC modulated to have the possibility to extract

the useful signal from the noise by means of lock-in amplification.

From the obtained vertical signal we can deduce the orientation of the out-of-plane component of the electric polarization. The induced mechanical deformation has the same frequency as that of the applied voltage, but may have a difference of phase. If it is in phase with the applied voltage, as shown in Fig. 12 on the left, when the field is positive (negative voltage applied to the sample) the domain will expand and the tip will be deflected upwards. We define this as in-phase measurements. When the polarization is in the opposite direction, the movement of the ferroelectric surface, and thus the deflection of the tip, will be in the opposite direction and then the phase shift between the electric signal and the signal given by the photodiodes has a phase of 180°. The phase of the vertical signal, which can be 0 or 180°, gives the orientation of the polarization for out-of-plane ferroelectric domains.

The lateral signal is given by the twisting of the tip. This signal is related with the lateral component of the polarization along the direction of movement of the cantilever, as shown in Fig. 13. Thus, with a set of measurements in orthogonal directions of the sample, PFM is in principle able to provide a three dimensional description of the electric polarization [62].

Finally, controlling the amplitude of the applied voltage during the PFM scan, we are able to switch the polarization of the sample and use the PFM tip to "write" ferroelectric domains [63].

2.3 X-ray diffraction

Diffraction experiments deliver a lot of information about sample crystallinity, symmetry of the crystals, lattice parameters, size of grains, presence of defects, presence of different phases or preferential direction of a polycrystal. X-ray diffraction corresponds to elastic scattering of photons with matter. It can be classically described by the movement of electrons of the atoms due to the electric field of the light. Thus, every electron is like a punctual source of elastic light emission, and these different emitted light waves interact with each other.

It can be shown that, for an almost plane incident wave, the amplitude of the scattered wave with momentum transfer $\vec{Q} = \vec{k}_f - \vec{k}_i$, with $\vec{k}_i$ and $\vec{k}_f$ the initial and scattered wave vector, the pattern of the scattered waves, observed at a large distance from the sample, is proportional to the Fourier transform of the electronic density, $\int \rho(r) e^{i\vec{Q}\vec{r}} d^3r$ [64]. For an infinite periodic lattice with electronic density present only at the lattice points, which is described as an infinite Dirac sum, the Fourier transform is an infinite Dirac sum, corresponding to the reciprocal lattice, of the momentum transfer. This means that diffraction is possible only if the momentum transfer corresponds to a reciprocal lattice vector. Taking into account that the crystal is not infinite, and that the X-ray beam probes only a small part of it, the probed electronic density can be seen as an infinite Dirac sum multiplied with window functions. The Fourier transform of a product of function is the convolution of the Fourier transforms of these functions. As the Fourier transform of a rectangular window function is a cardinal sine function (or *sinc* function), the Fourier transform of the probed electronic density will corresponds to an infinite sum of cardinal sine functions, each one centered on a reciprocal lattice point. In particular, for thin films or crystals, the direction perpendicular to the surface is generally the direction for which less atoms are probed. Thus it would corresponds to a smaller window function

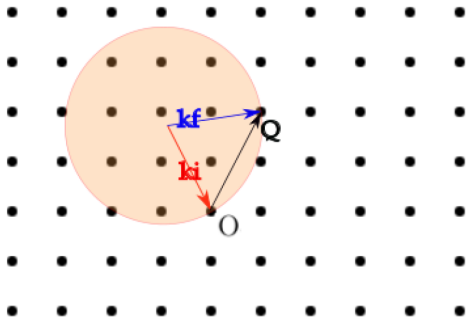

Figure 14 – Ewald sphere for a 2D lattice.

and thus the diffraction peaks will be elongated in that direction. These are called crystal truncation rods [64].

Thus the momentum transfer does not need to correspond exactly to a reciprocal lattice vector, a slight change from these values will also lead to scattering: spatial limitation of the probed electronic density leads to the broadening of the diffraction peaks. The energy of the X-rays can also influence the size of this window function, as higher energy X-rays will penetrate more in the crystal. But the electrons can not be considered localized at the lattice points of a crystal. Considering that the electronic distribution is not present only at the lattice points but corresponds to the distribution of the electrons in an atom, with the atoms at each lattice point, and the presence of a motif, with the sum of several atoms in the unit cell, the electronic density is described by the convolution of an infinite Dirac sum with the electronic distribution of a unit cell, and then multiplied with window functions. The Fourier transform of a convolution of two functions corresponds to the product of the Fourier transform of each function, so the unit cell electronic distribution will influence the distribution of the diffraction amplitude by a multiplicative factor which will modulate the amplitude of the peaks, usually decreasing the intensity for peaks away from the direct diffraction spot.

Thus the Fourier transform of the electronic density of a crystal corresponds to

its reciprocal lattice with broadened lattice points and with a modulation of their intensity. Diffraction will occur if the momentum transfer Q is equal to a vector of this reciprocal lattice. This condition can be described with the help of the Ewald sphere. This sphere is constructed from the k_i wave vector. As k_i and k_f have the same amplitude due to the elastic scattering, the k_f vector will also be contained in this sphere. With the origin of the reciprocal lattice on the end of the k_i vector, diffraction will occur if the Ewald sphere intercept a lattice point of the reciprocal lattice, as shown in Fig. 14. For this condition to be satisfied, the energy of the X-rays (and thus the Ewald sphere radius) can be changed, or the crystal can be rotated (thus rotating the reciprocal space lattice). Generally, the energy of the X-rays is constant and the sample is rotated, as well as the detector. The diffraction corresponding to a reciprocal lattice vector Q can be associated in the direct space to the reflexion of a family of parallel planes, perpendicular to this vector, with a distance d between them, as shown in Fig. 15. Those X-rays will interfere constructively if their optical path difference is equal to a multiple of their wavelength. Constructive interferences from the reflexion on these planes lead to $\lambda = 2dsin(\theta)$, which corresponds to the Bragg law, with θ the angle between the incident X-ray beam and the diffraction plane in the sample. As $\vec{Q} = \vec{k}_f - \vec{k}_i$, Q can also be related to θ by $Q = \frac{4\pi sin(\theta)}{\lambda}$.

In the next paragraphs we will present three diffraction techniques that we have used, θ-2θ scans, X-ray reflectivity (XRR) scans and reciprocal space mapping (RSM).

2.3.1 θ-2θ scans

Various experiments using diffraction are available. For thin films grown over a crystalline substrate, the configuration used is often θ-2θ scans. These scans consist of

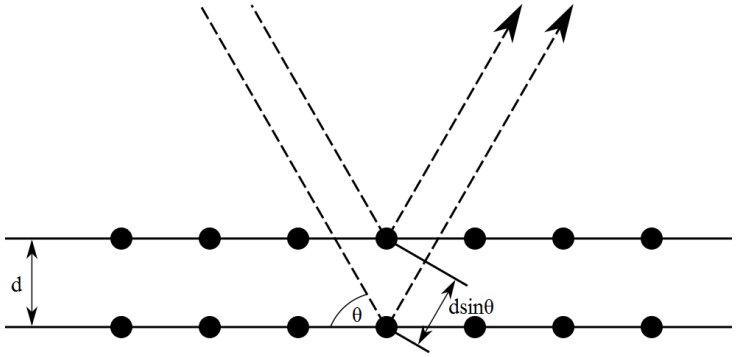

Figure 15 – Bragg reflections [65]

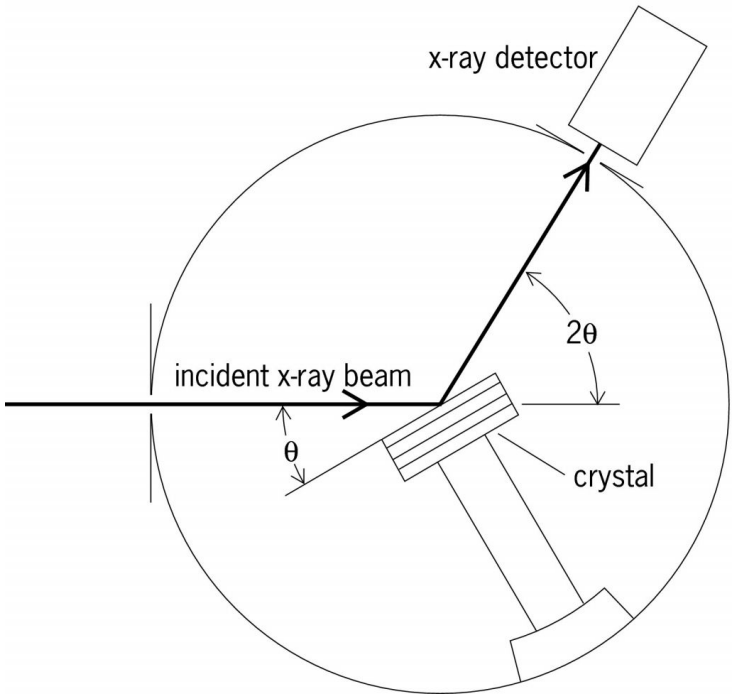

Figure 16 – Configuration of a θ-2θ scan [66]

measuring the diffraction intensity for reciprocal space vectors along the axis perpendicular to the surface of the sample. This means that the planes which reflects the X-ray are parallel to the surface. For that, the angle between $\vec{k}_i$ and the sample surface must always be half of 2θ, the angle between $\vec{k}_i$ and $\vec{k}_f$. During the measurement the X-ray source is fixed, whereas the sample holder and the detector rotate along the same axis, perpendicular to the plane of Fig. 16. The sample holder and the detector are rotated simultaneously, the sample holder by $d\omega$ and the detector by $2d\theta$, with in this case $\omega = \theta$ for all the measurement. θ-2θ scans thus probe the reciprocal lattice along the normal to

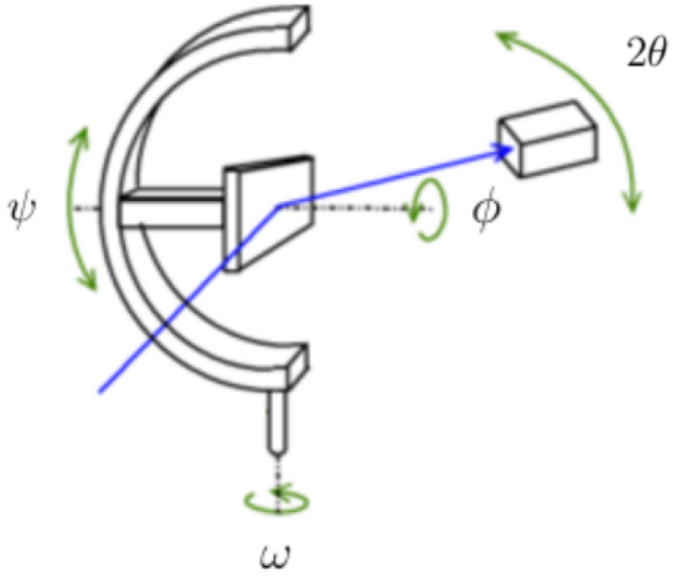

Figure 17 – Schematic representation of a diffractometer.

the surface. For that configuration to be possible, the alignment of the sample surface, in relation to the X-ray source and to the detector, must be done beforehand. For this thesis the sample measured by diffraction were thin films grown over a monocrystal of cubic (001) $SrTiO_3$ (STO). A possible miscut angle can make the 001 axis of the crystal a bit different from the normal of the surface, thus, in order to probe the reciprocal lattice along the (001) axis of the substrate, the (001) or (002) Bragg peaks have to be used for precise alignment.

We name $\vec{x}$, $\vec{y}$, and $\vec{z}$ the axis of the crystalline substrate (with $\vec{z}$ perpendicular to the surface). Fig. 17 show the schematic of a typical diffractometer used as sample holder. It enables rotations in 3 directions, rotation of ω, ψ and ϕ as shown in the figure.

The ϕ rotation axis of the sample holder do not necessarily correspond to the $\vec{z}$ axis of the crystalline substrate. This is not important for doing θ-2θ scans but have its importance for doing reciprocal space maps as described in section 2.3.3 further on. Indeed in this case a ϕ rotation is usually needed. It is possible to align the $\vec{z}$ to the ϕ

rotation axis when the sample is mounted on a goniometer. Using the reflection of a laser on the surface of the sample, a ϕ rotation will induce an elliptical movement on the laser. The goniometer is adjusted so that a ϕ rotation does not induce any movement of the reflexion of the laser. For that we may mark the position of the laser for ϕ equal to 0, 90, 180 and 270°, and then adjust the goniometer so that the reflexion of the laser is at the center of the ellipse.

The incident X-ray direction is fixed for the measurement. For a fixed detector position (determined by 2θ) the measured reciprocal lattice vector is also fixed (equal to $\vec{k}_f - \vec{k}_i$, with the direction of $\vec{k}_f$ determined by the position of the detector), so for the position of detector corresponding to the 2θ of a Bragg peak (usually the 002 Bragg peak for the STO substrate), we now have to move the sample so that the 002 reciprocal vector get aligned to this $\vec{k}_f - \vec{k}_i$ vector, and then we will measure the intensity corresponding to the 002 Bragg peak. To align the position of the detector in relation to the X-ray source, the sample holder is removed, and a 2θ scan (rotation of the detector) is taken to determine the 2θ position for maximum intensity, then this position is set to $2\theta = 0$. After that, the sample holder is translated until the X-ray beam is cut by half. Then an ω scan (rotation of the sample holder as shown in Fig. 17) is done and ω is set to zero for the position of maximum intensity, a ψ scan (see Fig. 17) is performed, also searching the position of maximum intensity, although at $\omega = 0$, the intensity detected is not really sensitive to the ψ angle. To completely align the surface of the sample, the ω and 2θ angles of sample holder and detector are changed, with $\omega = \theta$ corresponding to the Bragg angle of the 002 planes of the substrate.

Then, an ω and a ψ scan are again performed, searching the position of maximum intensity of the diffraction peak. This ψ position should then be set to zero and the ω

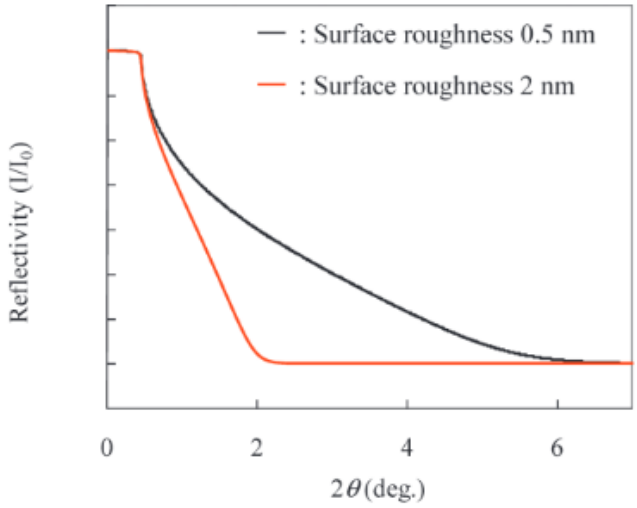

Figure 18 – Reflectivity in function of sample roughness [67]

position to θ. After this alignment, θ -2θ scan can be performed, and it is possible to identify all the reflecting planes of the thin film and the substrate almost parallel to the sample surface, corresponding to a reciprocal lattice vector along the $\vec{z}$ axis of the substrate. With the Bragg law, the Bragg angles can be related to the distance between the planes responsible for the diffraction. As the d distance of the diffracting planes is a characteristic of the material and of the orientation of the planes, it is possible to determine if the thin film is polycrystalline, if it has preferential orientations or various phases. From θ or d, we can deduce the value of lattice parameters or equivalently the values of the reciprocal lattice vectors.

2.3.2 X-ray Reflectivity

Doing θ-2θ scans with θ (incidence angle) below 10° also gives informations about the sample, even if no diffraction peaks are visible. This measurement corresponds to X-ray Reflectivity (XRR).

For a infinite and uniform sample, either crystalline or amorphous, for θ below

the critical angle of the material, the X-rays are completely reflected. Then, with increasing θ, the reflectivity decreases rapidly [67], and this decrease is intensified with the rugosity of the sample, as seen in Fig. 18, because roughness increases diffuse scattering leading to a rapid decrease of the signal [64]. With a thin film above the infinite sample with a different electron density, when the incidence angle is above the critical angle, some X-rays can be subjected to various refractions and reflexions at the air/thin film interface and the thin film/substrate interface before reaching the detector. There exist incident angles so that all those X-rays and the ones directly reflected by the ar/thin film interface interfere constructively (or destructively), this will lead to oscillations appearing in the reflectivity signal. Those oscillations are called Kiessig fringes. Their periodicity is characteristic of the films thickness. Indexing the maxima of the oscillation it is possible to determine the value of the film thickness :

$$d = \frac{\beta\lambda}{2}$$

Where the β coefficient corresponds to the slope of the index number of the maximas of the fringes in function of the valor of the corresponding $sin\theta$ [33].

Therefore with increasing thickness the angular periodicity decreases, and inversely, with decreasing thickness the angular periodicity increases.

It is usually not possible to detect films with thickness of less than a few nanometers, especially if the rugosity of the surface is important, which will attenuate rapidly the signal with increasing angles, and thus the oscillations could not appear. Conversely, for thickness of more than nearly 100nm, the instrument angular resolution may not be sufficient to observe the oscillations [33].

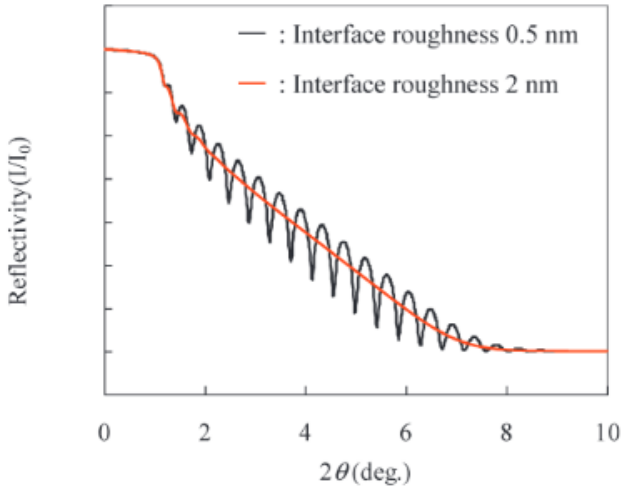

Figure 19 – Reflectivity in function of interface roughness [67]

As the reflection at the thin film/infinite substrate interface depends on the difference of density between the thin film and the substrate, and depends on the rugosity of this interface, the amplitude of the oscillations will also depends on those parameters [67]. The larger the difference of density, the higher the amplitude of the oscillations (and also the higher the critical angle). The amplitude of the oscillations also decreases with increasing interface roughness [67], as shown in Fig. 19.

Finally, if more than one layer is present, various oscillation frequencies will appear. These oscillations can be modeled to give structural information about the heterostructure, like the thickness of each layer and the quality of their interface.

2.3.3 Reciprocal space mapping

θ-2θ scans give a measure of the reciprocal lattice of the sample, with the intensity of the peak as function of the Q_z component of the reciprocal lattice vector (with Q_x and Q_y null). But it is also possible to obtain the diffraction intensity as function of other components of $\vec{Q}$, using reciprocal space mapping (RSM) as we describe in the following.

We saw above that the ϕ axis of rotation of the sample holder should be aligned with the surface normal of the sample (corresponding in a good approximation to the z axis of the substrate) for θ-2θ scans, but the x and y axis still not correspond to the other rotation axes of the sample holder (of angles ψ and ω). For that the ϕ angle should be adjusted. It can be done with the measurement of a reciprocal lattice vector which is not parallel to the z axis of the sample. We will use the example of the (103) peak of STO or its equivalent. From the configuration where the measured reciprocal lattice vector corresponds to the (002) Bragg peak of STO (with the sample aligned as explained above), the ω angle corresponds to the angle between the incident X-ray and the perpendicular plane to the z axis, and is equal to θ (the half angle between incident and scattered beam), and the ψ angle is zero.

To measure the (103) peak we have to place the detector at the right $2\theta_{103}$ position, and the sample holder corresponding position of $\omega = \theta_{103}$. But this would be still for a reciprocal lattice vector parallel to the z axis. It is necessary to rotate the sample holder to align the 103 peak with the measured reciprocal lattice vector. This could be done with a rotation of the ψ axis but then the associated peaks of the thin film would appear for a different value of ψ, and it would not be possible to see them doing a simultaneous rotation of ω and 2θ as it is usually done for RSM. Thus to find the peak the ω angle is changed from the θ_{103} position to $\pm$ 18.4°, the angle between the 103 peaks and the z axis. Then the sample is rotated along the z axis (ϕ angle) until finding a peak. As the z axis may not correspond exactly to the ϕ rotation axis in spite of the previous alignment, ψ and ω angles should be adjusted again, looking for the maximum of intensity, and set respectively to zero and $\theta_{103} \pm 18.4°$. Now we can say that the crystallographic axes of the substrate are aligned with the rotation axes of the sample holder. We take

for convention $\vec{x}$ the axis of the substrate parallel to the ω rotation axis, and $\vec{y}$ the axis of the sample parallel to the ψ rotation axis.

The simplest way to measure diffraction peaks with the reciprocal space vector not parallel to the z axis is to measure scans similar to θ -2θ but with ω different from θ. RSM is done by 2 axis measurements scans, rotating simultaneously ω and 2θ (sample and detector), with $d\theta = d\omega$, so that the offset $\omega - \theta$ is constant along the scan. Several scans are measured with different values of $\omega - \theta$ offset, enabling a broad range of values and to plot the intensity of diffraction in function of Q_y and Q_z for a given Q_x component (usually null). For that we have to express the probed reciprocal vector as function of the measured angles. After a rotation of χ and/or ω from its inicial $\chi = 0$ and $\omega = \theta$ position, the inicial x, y and z axis of the sample are changed into the x', y' and z' axis. But as the measured vector is fixed by the detector, the reciprocal lattice vector which is measured is still along the initial z axis. So in order to know the components of the measured reciprocal lattice vector relative to the new axis of the substrate, we have to project the z axis on the new axis $\vec{x''}$, $\vec{y''}$, and $\vec{z''}$ of the substrate. It gives considering first a ω rotation and then a ψ rotation :

$$\vec{z} = cos(\omega - \theta)cos(\psi)\vec{z'} + cos(\omega - \theta)sin(\psi)\vec{x'} - sin(\omega - \theta)\vec{y'}$$

To express the probed reciprocal vector in function of the angles, we use $Q = \frac{4\pi sin(\theta)}{\lambda}$. Thus we can write $\vec{Q} = (\frac{4\pi sin(\theta)}{\lambda})(cos(\omega - \theta)cos(\psi)\vec{z''} + cos(\omega - \theta)sin(\psi)\vec{x'} - sin(\omega - \theta)\vec{y'})$

In practice only the ω angle is rotated, giving : $\vec{Q} = (\frac{4\pi sin(\theta)}{\lambda})(cos(\omega - \theta)\vec{z'} - sin(\omega - \theta)\vec{y'})$

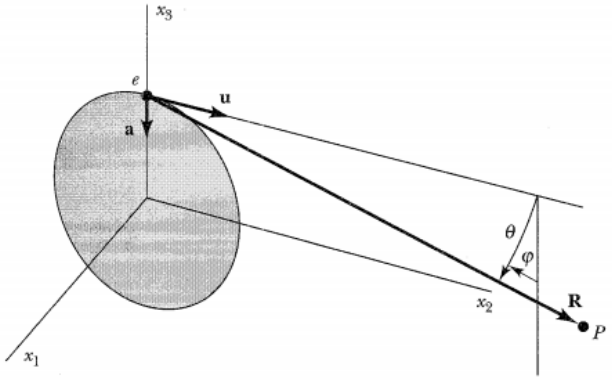

Figure 20 – Coordinates system used to calculated the radiation emitted by a relativistic electron [68].

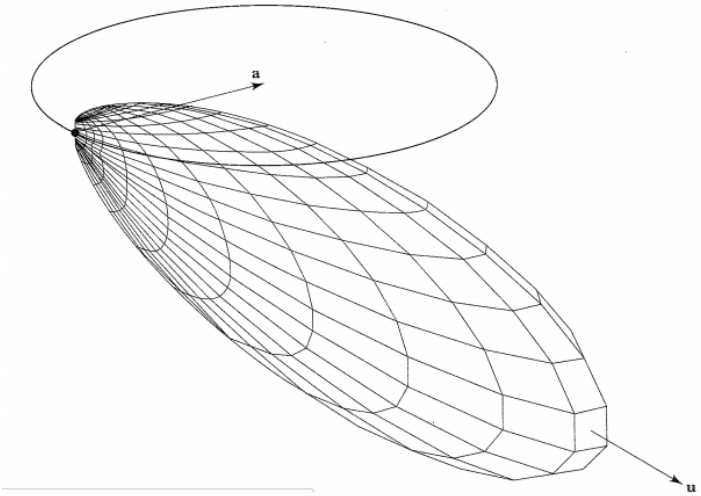

Figure 21 – Spatial distribution of the radiation emitted by a relativistic electron [68].

Or equivalently : $\vec{Q} = (\frac{2\pi}{\lambda})((sin(2\theta - \omega) + sin(\omega))\vec{z'} - (cos(2\omega - \theta) - cos(\omega))\vec{y'})$

RSM is interesting for example to check if a thin film has the same in plane lattice parameter as the substrate (strained film), or to look for the presence of different ferroelastic domains.

2.4 Synchrotron radiation

The radiation emitted in a synchrotron is related to the transversal acceleration of relativistic charges (electrons moving in a storage ring). The relativistic electromagnetic

theory allows to understand the spatial distribution of this radiation, and its dependence with some parameters of the ring. With the Liénard Wiechert potentials, and considering the radiation of a charge in a circular orbit, it is possible to find the electromagnetic fields emitted by this charge, and we can deduce from these fields the emitted power per unit of solid angle [68], [69]:

$$\frac{dP}{d\Omega} = \frac{e^2a^2}{4\pi c^3}\frac{(1-\beta cos\theta)^2-(1-\beta^2)sen^2\theta cos^2\phi}{(1-\beta cos\theta)^5} \tag{2.1}$$

With the coordinates used in Fig. 20, and β the value of the electron velocity divided by the speed of light, and a the value of acceleration. The spatial dependence of this power is represented in Fig. 21. We can see that for relativistic charges, most of the radiation is emitted tangentially and in the direction of the motion. In the plane of the electron orbit, the angle at which we can consider all the radiation emitted is of the order of $1/\gamma$, with $\gamma = \frac{1}{\sqrt{1-\beta^2}}$. This factor γ (which we can relate to the energy of the electrons) is therefore important to have a small emitted photon beam (which permits to have an higher brightness). It justifies the use of relativistic charges to have a large γ. The brightness represents the number of photons per second, per unit area and solid angle, and for 0.1 % width in frequency (convention to compare between synchrotrons). In addition, if we integrate the power over all solid angles, considering that the β is almost equal to 1 (which is a good approximation, the electrons having an energy of more than 1 GeV), we find that the total emitted power is proportional to γ^2, thus we also see here the importance of having relativistic charges. The discussion above is valid only for one electron, and characterizes the emission at one point of the electron trajectory, with the electron in a circular orbit.

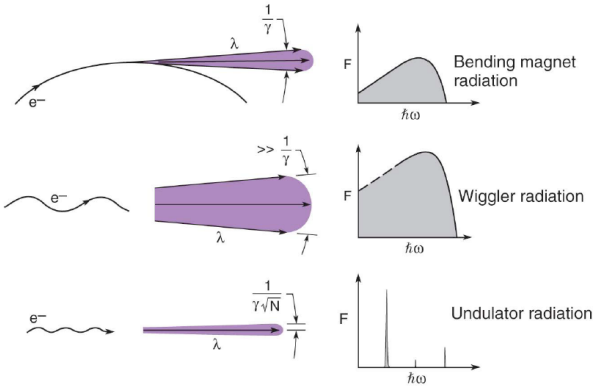

Figure 22 – The three ways to produce radiation in a synchrotron: bending magnets, wigglers and undulators [70].

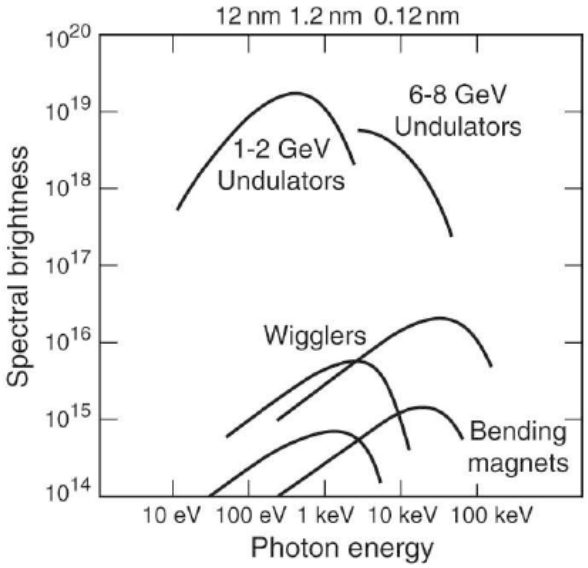

Figure 23 – Brightness of different synchrotron sources in low and high energy machines [70].

In the storage ring, there is not just one electron but several equidistant bunches of electrons. As they loose energy because of radiation, a radio-frequency cavity periodically accelerate them, so that the energy of the electron is almost constant. Thus radiation is emitted every time a bunch of electron pass through the bending magnet, resulting in a pulsed time structure. In modern synchrotrons, each pulse lasts around a few tens of picoseconds with a broad variation of time between pulses that can range from a few nanoseconds to several microseconds. This time structure makes possible to perform time-resolved experiments.

In spite of the ultra high vacuum in the storage ring, collisions between the electrons and any atom or molecule present in the storage ring continuously decrease the number of electrons in the storage ring. At LNLS in Campinas, reinjection of electrons is made more or less after every 12h. During this elapsed time, the loss of electrons in the storage ring made the photon emission progressively lower. The trajectory of the electrons is not perfectly circular in the storage ring, but is composed of straight sections and region where the electron trajectory is curved to close its path into a polyhedron. These curves are imposed by bending magnets.

2.4.1 Insertion devices

The most basic sources of radiation in a synchrotron are the bending magnets that keep the electrons in a closed trajectory. But these magnets have a limited performance. To obtain brighter X-rays beams, it is possible to use insertion devices installed in the straight sections between bending magnets. These devices are composed of periodic arrays of permanent or electro-magnets. The resulting periodic magnetic field deviates the electron beam from its reference trajectory within the straight section. Modern synchrotron sources are built to optimize the emission by insertion devices.

In general insertion devices will bend the electron trajectory several times as depicted in Fig. 22. Depending on how much the electrons are deviated from their straight trajectory, the emitted radiation will have two distinct behaviors:

Strong deviations : In this case each half-period of the magnetic array behaves as independent bending magnets. The final intensity is proportional to the number of repetitions or periods of the magnetic array. These devices are called *wigglers*, and

deliver X-rays beams around one order of magnitude more intense than bending magnets.

Weak deviations : in this case the effective magnetic field of the insertion device is small enough in order that the deviation of the electrons can be well approximated by a sinusoidal function. Within this approximation there is a constructive interference among the radiation beams emitted by each period of the magnet array. This interference provides X-rays beams several orders of magnitude more intense than bending magnets. In this case the emitted radiation is not continuous anymore, but has peaks were the intensity is maximum. These devices are called *undulators*.

Fig. 22 shows the spectra of the radiation for bending magnets, wigglers and undulators. In the case of wigglers, as there is no interference the emitted spectra is similar to the spectra of a bending magnet, which consist of a broad spectra. The intensity is just summed incoherently for each curve of the electron bunch. For undulators, the interferences result in a much more intense emission (the brightness value is higher by several orders of magnitude) and a discretized spectra. The frequency of the peaks appearing in the wavelength spectrum depends on the spatial frequency of the magnets and on the magnetic field generated by these magnets. By changing the gap between the two arrays of magnets, and thus the magnetic field seen by the electrons, we can then change the value of the energy peaks of the undulators. Fig. 23 shows brightness values that can be reached with the different devices. For the undulators, the brightness values correspond to the maximum that can be reached by changing the gap between the array of magnets for one energy considered. For the wiggler and bending magnet, it corresponds to the full spectrum, we see that above a certain value of energy, the emission decays a lot. This can be explained by relativistic electromagnetic theory [69].

The much higher brightness for undulators is also due to its low emittance compared to bending magnet or wigglers. The emittance corresponds to product of the angular distribution and the size of the beam and this parameter is conserved along the path of the beam. Thus a low emittance enables to focus more the beam onto the sample, and then improve the brightness. For an undulator, the angular distribution is limited by the γ angle, and the size of the emitted photon beam is roughly the size of the bunch of electrons.

2.4.2 Polarization of the photon beam

The photon beam can be described as an electromagnetic wave, and the spin of the photon can be related to the polarization of this electromagnetic wave. For a polarized plane wave with propagation wave vector $\vec{k}$ along the z axis and w the angular frequency of the wave, the polarization of the wave is described by the spatial and temporal dependence of the electric field (phase relation between space and time), $\vec{E} = E_{0x}cos(kz-wt+\phi_1)e_x + E_{0y}cos(kz-wt+\phi_2)e_y$. Thus, in the (x,y) plane, if $E_{0x} = E_{0y}$ and $\phi_1 - \phi_2 = \pm\frac{\pi}{2}$, the electric field will have a circular movement in this plane (circular polarization), which corresponds to photons with up or down polarization, depending on the direction of rotation. If the two components are in phase, $\phi_1 - \phi_2 = 0$, then the movement of the electric field is linear, with the direction of electric field oscillations defined by the E_{0x} and E_{0y} components, this type of polarization is said to be linear. It can be seen as an equal contribution from photons with spin up and down. In the more general case of $\phi_1 - \phi_2 \neq 0$ and $E_{0x} \neq E_{0y}$, or in the case of $\phi_1 - \phi_2 \neq \pm\frac{\pi}{2}$ or 0, the electric field oscillation will describe an ellipse.

For synchrotron radiation, a linear motion of the electrons, as present in wiggler

and undulators for the transversal motion, will result in a linear polarization of the emitted photons, in the same direction as the direction of motion of the electrons. This can be understood classically by the radiation of an electron in the presence of an alternate electric field. If the electrons have an helical motion, and thus their transversal motion is circular, the emitted photons will have a circular polarization. This helical trajectory of the electrons is possible to obtain modifying the configuration of the two arrays of magnets in an undulator. Circular photon polarization can thus be obtained. For bending magnets, looking away from the orbit plane of the electrons, the projected movement can be seen as an ellipse and thus an elliptical polarization is observed. Looking in the orbit plane of the electrons, the motion is similar to horizontal oscillations, thus the photons emitted in this plane have horizontal polarization. In this case it is possible to use mostly circularly polarized photons selecting the out of plane emitted photons, the two circular polarization are available, selecting the photons above or below this plane.

2.4.3 U11 beamline

The U11 beamline at the Brazilian National Synchrotron Light Laboratory (LNLS) uses an elliptical undulator with a spatial period for the magnets of 50 mm and producing a magnetic field of around 1 tesla. The dispersive element used is a plane grating monochromator, which also focus the beam vertically (thanks to a variable line spacing) into the exit slit placed after the monochromator. A toroidal mirror collimates the beam vertically before it gets to the monochromator, and after the monochromator another toroidal mirror collimates the beam vertically and horizontally into the sample. Before the grating, a plane mirror is used to have the possibility to change the incident angle on the grating [71]. The energy range available is between 100 and 1500eV. The

resolution in energy $\Delta E/E$ is adjustable by selecting the opening of the exit slit of the monochromator. In general this resolution is better for low energy photons, going from a few meV at 100 eV up to almost 1 eV at higher energies. One can always improve the energy resolution reducing the aperture of the exit slit, but this also reduces the X-ray intensity at the sample. The user must always trade between energy resolution and X-ray intensity, optimizing for the specific experimental requirements.

In the next sections we will see that synchrotron radiation is widely used for two electron emission techniques, X-ray absorption spectroscopy (XAS) and Photoemission electron microscopy (PEEM).

2.5 X-ray spectroscopy: photoabsorption and photoemission

Synchrotron are extremely versatile materials science tools. One single machine normally offers several techniques. Here we will concentrate on those that have been used during this work. In the following sections we will discuss the basic aspects of X-ray absorption and X-ray photoemission spectroscopies, in the energy range named soft X-rays, where operates the beam lines used to study the samples we grew. This energy range covers roughly the spectral range of photons from a few hundreds up to a few thousands of electronvolts. We conclude this section discussing the photoemission electron microscopy (PEEM), which allowed us to obtain detailed information about the magnetic and ferroelectric domains in $Fe/BaTiO_3$ heterostructures.

2.5.1 Absorption of photons by matter

Both X-ray absorption spectroscopy (XAS) and X-ray Photoemission Spectroscopy (XPS) start with the absorption of a photon by an atom. The exact mechanism

involved in the interaction depends on the energy of the photon and atomic number of the atom. In the soft X-ray range, the photoelectric effect is by orders of magnitude stronger than the remaining interaction channels.

In the photoelectric effect the electric field of the photon interacts with one bound electron and transfers its energy to the electron. In this process the photon is annihilated and the electron will be excited from its ground states. The final state of the electron depends on the photon energy and must be one of the following:

The photon transfers enough energy to take the electron from the atom In this case the electron becomes free from the atomic binding. Once out of its original atom the electron can be reabsorbed by the material, or if it is close enough to the surface, the electron can be ejected from the sample to the vacuum. In this last case the electron will carry a kinetic energy that will be the difference between the original photon energy, $\hbar\nu$ and the binding energy of the electron-atom, E_B. To be exact, the ejected electron must also expend some energy to leave the material itself, which is called work function, ϕ.

The energy of the photon excites the electron within the same atom Here the photon energy $\hbar\nu$ is not enough to take the electron out of the atom. But still, the electron is excited to an empty state in the same atom. This process is resonant, which means that its cross section increases abruptly when the energy of the photon is exactly the difference in energy between the final and initial electron state. This means that the probability of absorbing photons with the right energy to promote internally one electron is much higher than to absorb a photon with arbitrary energy. The increase in the absorption probability is called absorption edge.

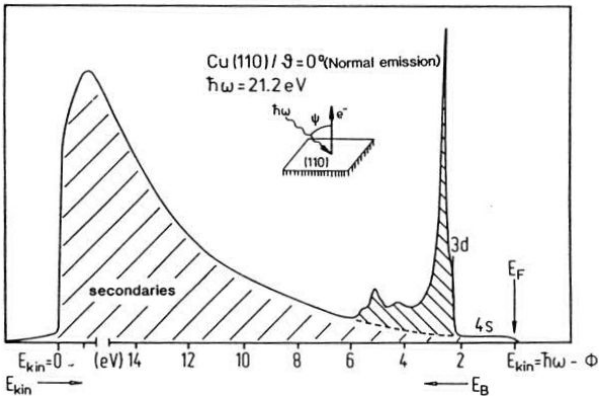

Figure 24 – An example of full photoemission spectrum. In this case the sample is pure cooper illuminated with ultra-violet source.

Each part of the process above gives rise to one spectroscopic technique: when the electron is ejected from the sample we have XPS. When the electron is excited within the same atom we have XAS. In the next sections we give more details about each of these techniques.

2.5.2 The photoemission process

In X-ray photoemission spectroscopy, XPS, the absorption of a photon results in a transition between a state of a core level electron to the continuum of energies represented by the vacuum. The emitted electron is then a photoelectron. Because of the conservation of energy in the absorption process, we can deduce the initial binding energy of the photoelectrons $E_b = \hbar\nu - E_k - \phi$, with E_b the binding energy, $\hbar\nu$ the photon energy, ϕ the work function which is material dependent, and E_k the kinetic energy of the photoelectron.

The photoemitted electron can be detected by hemispherical analyzers, which will measure their kinetic energy. A typical photoemission spectra is shown in Fig. 24. Various types of electrons are present in those spectrum. The fine peaks correspond to photoemission electrons, which did not get inelastically scattered. Their binding energy

is characteristic of the electronic transitions and thus of the chemical element. They also can correspond to Auger electrons, in this case, their kinetic energy is characteristic of the chemical element, and does not depend on the energy of the photon. Indeed, after the emission of an electron, the core level hole can be filled by electrons from higher energy levels which results in the emission of an Auger electron (see part Auger), or in the emission of a photon (in this case the process is called fluorescence).

The broader part on the right, corresponding to electrons with low binding energy, are electrons emitted from valence states. Also, the inelastic interactions of electrons with atoms lead to a cascade emission of low kinetic energy electrons (secondary electrons). They form a continuous background in the spectra with a peak at low energy. Synchrotron light is not a pre-requisite to perform XPS. One can use a UV lamp, which allows the high resolution in the low photon energy range. We speak then of UPS, Ultra-Violet Photoemission Spectroscopy), and then only the valence electrons part is present in the spectrum. One can also use standard X-rays sources.

As the mean free path of interactions between electrons and atoms is of the order of some nanometers for the range of energy considered, electrons emission techniques are surface techniques and are sensitive to the environment. Usually XPS is done under ultra high vacuum conditions to avoid surface contamination.

Photoemission spectroscopy has been widely used to check the chemical composition of samples and in this case is know by ESCA, which stands for electron spectrocopy chemical analysis. This is done quantifying the areas below the photoelectron peaks for each element in the sample. As one can know the cross-section for each transition, is possible to get the surface stoichiometry of the sample with good precision even for very light

element like carbon or oxygen, which are difficult to observe by other standard techniques.

2.5.3 X-ray absorption spectroscopy

The photon absorption coefficient of an atom is proportional to the probability of transition from the initial state to the final state within the same atom, which is given by the Fermi's golden rule [72]. This transition probability depends also on the density of unoccupied that can receive the excited electrons and respect the energy conservation. The possible final states of the electron are the unoccupied states that respect the selection rules for the dipolar approximation [72]. This means the orbital moment of the excited electron must change by ± 1 and the spin must be conserved.

The resonant energy where the absorption is maximum depends on the difference of the electron energy between final and initial states. As these energies are unique for each chemical species, XAS is element selective, and gives information on valence state, structure and chemical environment. It can also gives information on spin with x-ray magnetic circular dicroism as we discuss in the next section.

In order to measure XAS, one needs to change the photon energy and measure its absorption. This requires a broad photon energy range source, which in general is a synchrotron. In the soft X-rays range the photoabsorption is measured indirectly. When an electron is excited in the atom a core hole is created. This state is metastable. When the atom returns to its initial state some electrons on higher orbitals occupy the core hole and in the process loose energy to the system. This energy is dissipated with the emission of secondary electrons or with the emission of fluorescence photons. In the soft X-rays range secondary electrons are much stronger than fluorescence and they are used to have the indirect measurement of the absorption. To measure the number of secondary

electrons leaving the sample, the sample is grounded, so every time an electron leaves the sample, an electron from the ground arrives at the sample. The use of a current meter allows to measure, for each photon energy, the number of electrons per unit time that leave the sample and thus the absorption coefficient as function of the photon energy. This indirect way to measure the X-ray absorption is called total electron yield (TEY) detection.

2.5.4 X-ray magnetic circular dichroism

With synchrotron radiation it is possible to obtain X-rays with circular polarization. This allows to obtain the orbital and spin magnetic moments for the different elements of the sample. To do that, it is necessary to measure two X-ray absorption spectra, one with left circular polarization and the other with right circular polarization. The difference in absorption in the two spectra constitutes the X-ray magnetic circular dicroism (XMCD).

Here we will just consider a one electron picture to explain those XMCD effects. The transition probability to excite an electron (through the absorption of a photon by the atom considered) from initial state i to a non occupied final state f is given by the Fermi's golden rule, and is proportional to the squared transition matrix element, M_{fi}^2, with :

$$M_{fi}^2 = (|\langle f|\vec{\epsilon}.\vec{r}|i\rangle|)^2 \tag{2.2}$$

The factor $\vec{\epsilon}.\vec{r}$ corresponds to the interaction between the electron and the potential vector generated by the photon in the dipole approximation. Assuming the dipolar approximation for the electric field of the photon, an initial state described by the quantum numbers

$|n, l, m_l, s, m_s\rangle$, and a final state by $|n', l', m'_l, s', m'_s\rangle$, calculation shows that the transition matrix element is not null only if the following selection rules are satisfied :

$$l' = l \pm 1; m'_l = m_l + q; s' = s; m'_s = m_s \tag{2.3}$$

The selection rule $m'_l = m_l + q$ represents the conservation of angular momentum: the angular momentum of the incident x-rays is transferred to the excited photoelectron. From those rules it can be understood that, for a given final state, the absorption of a photon may satisfy those rules only for 1 circular polarization, because if the photon can not transfer its spin angular momentum to the core shell electron, there is no absorption. For example, for a transition from an initial 2p state (without considering the spin-orbit coupling in the 2p level) to a final 3d state with $m'_l = +2$, only a photon of positive helicity can be absorbed, which would correspond to a transition from an initial state with $m_l = +1$, thus respecting the selection rules. Nevertheless, this difference in absorption for the two circular polarizations of the photon leads to a circular dichroic signal only if the material has an orbital magnetic moment. If the available final states (the valence band empty density of states) have no imbalance of states for the angular momentum, there will be no dichroic signal when taking into account all initial and final states. This is coherent with the fact that circular dichroism measures the magnetism of the material.

For maximum effect, the photon propagation vector needs to be aligned with the magnetization direction, the magnetization measured is actually the projection of the magnetization on the photon propagation vector. This preferential absorption in function of polarization of the photon enables to measure the orbital moment from the XMCD signal, but while using $|n, l, m_l, s, m_s\rangle$ and $|n', l', m'_l, s', m'_s\rangle$ for describing initial and final

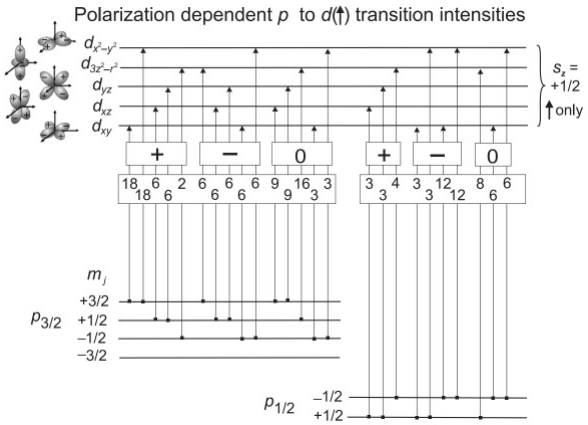

Figure 25 – Transition intensities from spin-orbit and exchange split p core states $|j, m_j\rangle$ to spin-up exchange split d valence orbitals. The + , - and 0 labels correspond to the value of allowed X-rays helicity in the transition. Taken from [73]

states, it is not possible to relate the XMCD signal to the spin moment.

Although the spin does not appear directly in the hamiltonian of (2.2) (which results in $m'_s = m_s$), the spin moment becomes involved in the dipole matrix element through the spin-orbit coupling in the core shell [72] (the spin-orbit coupling of the valence shell can usually be neglected). For example for the L_3 edge, the initial states are the $2p_{3/2}$ spin-orbit coupled states. As those levels have different proportion of spin up and down, for final states of a given spin, the probability of transition into a state of one spin ($+1/2$ or $-1/2$) will be different for the 2 circular polarizations, making the absorption process spin dependent. Fig. 25 shows the calculation of the individual contribution of transition intensities (to within a constant, see [73]) for transition from $2p$ states into $3d$ states. Only final states of spin up ($+1/2$) are represented, for transitions into $3d$ spin down states, the results are equivalent but with reversed photon helicity. The $2p$ initial states are assumed to be spin-orbit split (and are therefore described by their total angular momentum) and exchange split (which lift the degeneracy in m_j), the final states are the d valence orbitals (d_{xy}, d_{xz}, d_{yz}, $d_{x^2-y^2}$, $d_{3z^2-r^2}$ orbitals) also assumed to be exchange split.

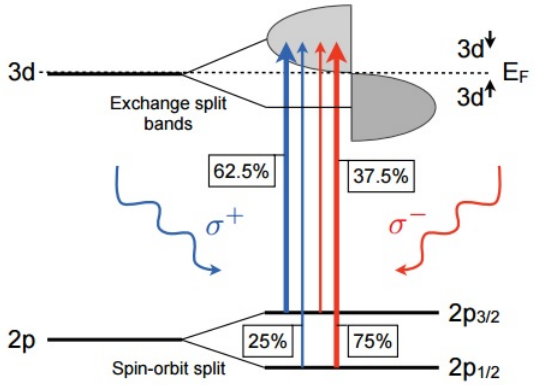

Figure 26 – Schematic XMCD effect for a strong ferromagnet (filled majority band) for transition from 2p spin-orbit splitted states to exchange split 3d states, σ^+ are photons with positive helicity and σ^- with negative helicity. [8]

From those individual contributions of Fig. 25, summing the contribution from all states, it is possible to calculate the probability of electronic transition from a $2p_{3/2}$ state (or a $2p_{1/2}$ state) with spin=+1/2 into the $3d$ final states of also spin=+1/2 (as the spin can not change). The transition probability are shown in Fig. 26 [8], for a strong ferromagnet (filled majority band). Since $2p_{3/2}$ and $2p_{1/2}$ levels have opposite spin-orbit coupling, the spin polarization will be opposite at the 2 edges [73], and so the spin contribution to the XMCD signal have opposite signal for those 2 edges.

It is possible to relate the difference of XAS signal with the two circular polarization independently to the spin and the orbital moment of the sample.

2.5.5 X-ray linear dichroism

XAS of single crystal with charge or magnetic moment anisotropies will show different absorption depending on the angle between crystalline axis and the direction of electric field E of the linearly polarized X-rays beam. This effect is know as linear dichroism.

For linear polarized X-rays, the electric field vector acts like a search light for the direction of the maximum and minimum of empty valence states. Thus the absorption will be stronger in the direction with more empty states. With this effect one can prove the anisotropy in electron occupation either by rotating the sample around the X-ray beam direction or by changing the polarization of the beam. Usually the last option is done.

Linear dichroism can also arise from magnetic effects within the atom. For a magnetic state with collinear spin alignment, spin-orbit coupling may lead to the deformation of the charge. This charge distortion is of uniaxial symmetry about the spin direction and will change the way X-rays of different polarizations will be absorbed.

The linear dichroism was heavily used to study the ferroelectric domains and we will discuss it further in the results section.

2.6 Photoemission electron microscopy

In photoemission electron microscopy (PEEM), atoms of a sample are excited through the absorption of photons (UV lamp, He lamp or synchrotron light in our case). This photon absorption results mostly in the emission of secondary electrons, which are accelerated (thanks to an high voltage applied to the sample) and collected into the microscope. Then a series of magnetic lenses enable to magnify the image of the sample formed by those electrons, while conserving information the spatial distribution of the electrons.

When an electron gun is used as a source instead, we speak about low energy electron microscopy (LEEM). Whereas PEEM is based on the photoemission process, for

LEEM, the electrons used for imaging come from an electron gun. As for other electron emission technique, the LEEM/PEEM is a surface technique.

Fig. 28 represents the LEEM/PEEM system from SPECS available in Campinas (although the electron gun is not available). Other measurements have been done in Berlin, at the UE56-SGM1 beamline of BESSY II, where a similar equipment is used (also from SPECS), but with an aberration-correction which uses a second magnetic prism and with an electron gun. It can be seen that the electron beam leaving the sample first go through the objective lens and then through the transfer lens. The combination of objective and transfer lens are used to image the sample in the diagonal of the magnetic prism (where field apertures can be inserted) and to image the diffraction plane (corresponding to the focal plane of the ensemble objective and transfer lens) into the entrance of the prism (where entrance slits can be inserted). For the diffraction plane at the entrance of the prism, electrons leaving the sample with parallel trajectory are focused at the same "point" within this plane. For the PEEM mode, this plane thus display the angular distribution (k_x , k_y) of the electrons leaving the sample. When using the LEEM mode (with the electron gun as the source), what is displayed for this diffraction plane will depends on the energy of the electrons reaching the sample. When the energy of the electrons leaving the electron gun is equal to the energy of acceleration from sample to objective lens (generally 15000 eV), the hight voltage on the sample will decelerate the electrons and they will reach the sample with almost no energy. In this mode (mirror electron microscopy mode), the electrons are reflected before hitting the sample surface. The contrast mechanism is based on local changes in the electric field on the sample surface. In this case the diffraction plane will only show a fine spot corresponding to the reflected electrons. When the energy of the electrons reaching the sample increases, the electrons can penetrate more

the sample, and so the diffraction plane will display, besides the reflected electrons spot and the angular distribution of the secondary electrons, a diffraction pattern if the sample is crystalline. In the magnetic prism, the electrons are 90° deflected into the center of the projector lenses, which will form the image in the fluorescent screen. The entrance plane of the prism is also imaged into the exit plane of the prism (where the contrast apertures can be inserted). The projectors lenses give the possibility to switch between the image mode (when imaging the diagonal of the prism) and the diffraction mode (when imaging the exit of the prism), and also to switch between different available magnifications for these two modes. The magnification determines the field of view (FOV) imaged. The prism can also be seen as an energy filter because of his dispersive properties [74]. Indeed, a slit can be placed at the entrance of the prism where is imaged the diffraction plane. With PEEM mode, this slit enables to select one component of the angular distribution of the electrons (the component perpendicular to the direction of the slit, let say k_x). After going through the prism, which has a dispersive field around the direction perpendicular to the slit, the diffraction plane imaged at the exit of the prism will present the energy dispersion on the x axis and the angular distribution k_y on the x axis. With a diffraction mode, it is thus possible to obtain angle-resolved photoelectron spectroscopy with this entrance slit, but a field apperture should be also inserted in the image plane to select a small region of the sample to avoid straight light. Then by changing the position of the entrance slit, and thus the selection of the k_x component it is possible to obtain the whole (E, k_x, k_y) phase space. With an entrance slit already inserted, it is possible to insert an aperture (the contrast aperture) in this plane (the exit plane of the prism) to select the energy of the electrons, and then to go back to the imaging mode so that the image corresponds to electrons of a selected energy (and angular distribution).

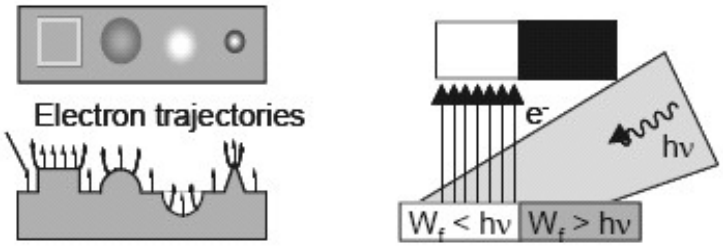

Figure 27 – PEEM topographical contrast on the left and workfunction contrast on the right [75]

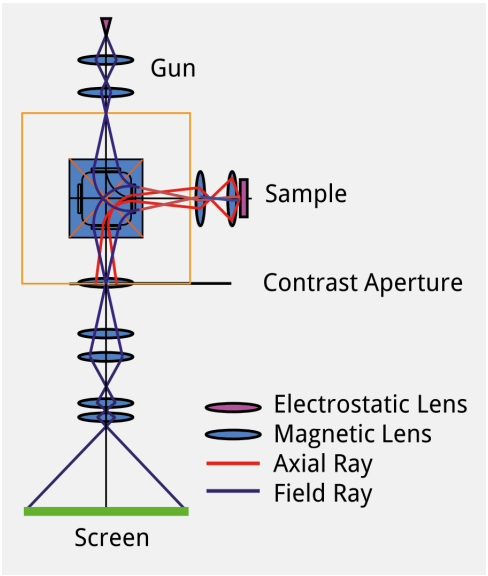

Figure 28 – Schematic of the LEEM/PEEM, SPECS P90 brochure

Using PEEM with UV lamp, the energy of the photons (around 5 eV) is quite similar to the work function contrast of most sample. Thus the electrons leaving the sample (corresponding to photo-electrons) have low energy. Using X-ray, the energy of the photons is much higher. Most of the electrons leaving the sample in this case will be secondary electrons, so most of the electrons emitted will still have low energy (some eV), but the dispersion in energy of the electrons will be much larger. That is why in order to improve the resolution with UV lamp, only the contrast aperture in the exit plane of the prism need to be inserted, to decrease the angular distribution dispersion of the electrons, whereas with X-rays, both entrance slit and contrast aperture have to be inserted to decrease angular distribution dispersion and energy dispersion. Without

aberration correction, a resolution of around 8nm was achieved by SPECS with UV lamp. With LEEM, generally neither entrance slit nor contrast aperture are needed to achieve a good resolution. Even without aberration correction, a resolution of around 2nm was achieved by SPECS.

2.6.1 Contrast

The contrast observed can be due, among others, to topography, workfunction, magnetic or electrical variation in the sample. Topographic contrasts occur for rough samples, this contrast is due to the curvature of the accelerator field around surface objects [75], as illustrated in Fig. 27, in the left image. This curvature of the field influences the trajectory of the electrons, and thus the image. Using UV lamp with energy close to the sample working function, the contrast that dominates is the working function contrast (shown in Fig. 27, in the right image). Since the photo-electrons emitted are low energy electrons, differences in the work function in the sample result in an important contrast. Ferroelectric domains may have charges in their surface, for example, out-of-plane ferroelectric domains with up polarization will present positive charges, and negative charges with down polarization. These charges result in a difference in the work function, it is possible to image ferroelectric domains with UV lamp. However, two in-plane ferroelectric domains with perpendicular polarization can not be differentiated. All types of in-plane domains are seen with the same contrast. Ferroelectric domains can also be observed with LEEM, using an electron gun, with a contrast also based on the surface charges. Using synchrotron light, which allows to select the energy and the polarization of the photon, it is possible to get elemental and chemical contrast (using an energy corresponding to an absorption peak of an element in a specific valence state), and using circularly or linearly

polarized light at a specific element energy it is also possible to observe ferromagnetic, anti-ferromagnetic or ferroelectric domains of the considered element, as will be explained below. It is also possible to get x-ray absorption spectra for a specific region of the sample (μ-XAS). For that, images at various photon energy are taken and the intensity dependence of a specific region of the image on the energy of the photon will constitute the spectra. Also with synchrotron light it is possible to do pump and probe experiments, which give information about the dynamics of the system. But the changes in the sample must be repetitive. A first pump pulse enable to initiate the dynamic of the system, and a second probe pulse to measure the state of the system. The evolution of the changes is determined by changing the time difference between pump and probe [76]. The probe pulse corresponds to a pulse of photons of the synchrotron, which has a width between 50 and 80 ps. The pump probe corresponds, for example, to a magnetic field pulse if we want to measure the dynamics of the magnetic domains. Other contrasts are available with LEEM. It is possible to get μLEED pattern, and selecting one diffraction point with the contrast aperture, it is possible to get dark-field imaging.

2.6.2 Observation of $BaTiO_3$ ferroelectric domains: XLD images

Besides UV lamp and electron gun, linearly polarized X-rays can also be used to image ferroelectric domains. We will explain here the observation of ferroelectric domains of a tetragonal ferroelectric like $BaTiO_3$ (BTO) cut along the (001) or (100) directions. For the observation of ferroelectric domain with PEEM, a treatment of the ferroelectric single crystal is necessary to clean it and make it conductive. This treatment is described in Ref [10], it consists first on a cleaning with ozone, in a chamber with a mercury lamp which produce ozone from the oxygen contained in atmospheric air, for 30 mn, in order

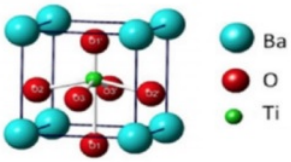

Figure 29 – BTO structure in the tetragonal phase

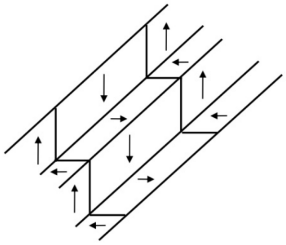

Figure 30 – Herringbone structure for ferroelectric domains, taken from [77]

to remove the carbon contamination. Then, after insertion of the sample in the PEEM which is operated in vacuum, an annealing of the substrate at 600 °C with an oxygen pressure of 4.10^{-6} mbar is done for 1 hour to obtain a good surface reconstruction of the BTO surface. Then an annealing of 2 hours at 700 °C in vacuum (base pressure of around 10^{-9} mbar) is done to create oxygen vacancies, which make the sample conductive [10].

There are 3 possible axis for the electric polarization in tetragonal BTO, with the polarization axis along the tetragonal distortion axis (Fig. 29). However, after annealing, most of domains are in-plane domains. For those domains, in order to avoid charges at the walls of the domains, the direction of the domain walls make a 45° angle with the electric polarization axis. Various patterns are possible, one of them being illustrated in Fig. 30 [77].

The linear dichroic contrast (XLD) uses structural differences of domains. Above 120°C, BTO is a cubic perovskite, with Ti atoms at the center of the oxygen octahedra. This octahedral environment leads to the lift of the degeneracy of the five $3d$ orbitals, with the e_g orbitals ($d_{x^2-y^2}$ and d_{z2} orbitals) which point on oxygen atoms having higher

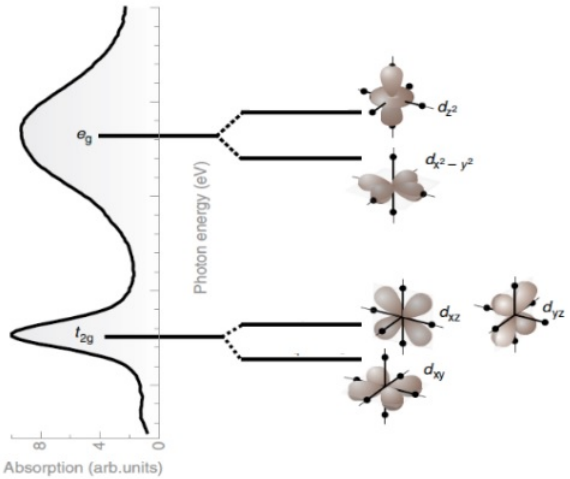

Figure 31 – Splitting of d Ti orbitals for a z domain of BTO, that is, along the c axis. [10]

energy, and the t_{2g} orbitals (d_{xy}, d_{xz} and d_{yz} orbitals) having lower energy. With cubic to tetragonal phase transition (occuring around 120°C), the Ti atom is displaced in direction of one oxygen (along x, y or z axis of BTO), responsible for ferroelectricity. This displacement of Ti atoms lifts the degeneracy of the t_{2g} and e_g orbitals through hybridization with the $2p$ oxygen orbitals (Fig. 31). The difference of energy between d_{xy}, d_{xz} and d_{yz} orbitals is not observable directly in a spectra of a BTO ferroelectric domain, and L_2 or L_3 edges present only 2 peaks related to t_{2g} (first peak) and e_g (second peak) orbitals (Fig. 31), but it is the splitting in the t_{2g} orbitals responsible for the ferroelectric contrast of the PEEM images as will be explained below.

For a z domain, the d_{xy} orbital is the one of lower energy, as shown in Fig. 31, whereas for x (y) domain, the orbital of lower energy is d_{yz} (d_{xz}). Those orbitals have an axis for which the density of hole available is minimum. For the orbitals of lower energy, those axis are respectively the x, y and z axis for the x, y and z domains. The PEEM images are taken with an energy of photons corresponding to the difference of energy between the $2p_{3/2}$ core level of Ti and those t_{2g} orbitals (first peak of the L_3 edge). The electronic transitions to these orbitals will have a lowest probability of occurring if the

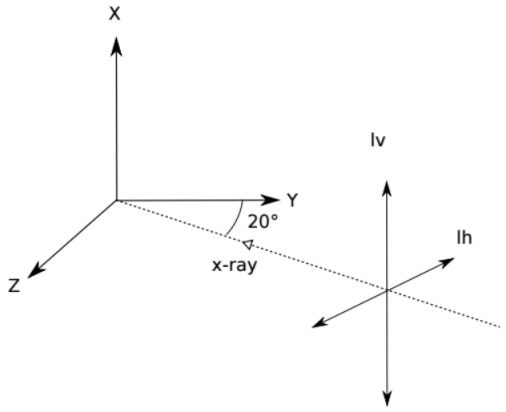

Figure 32 – Linear vertical polarization (lv), and linear horizontal polarization (lh). X and Y axis are along the surface of the sample, with X axis parallel to the vertical axis of photon polarization. lh axis make a 20° angle with the Z axis.

polarization of the photon is parallel to the axis of minimum density of hole available of the corresponding orbital (which also corresponds to the electric polarization axis for the orbitals of lower energy), this is because the electric field vector of the photon acts like a search light for the number of valence holes [10]. If the probability of transition is lower, less electrons will be emitted and the image will be seen darker. This contrast does not depend on the direction of the electric polarization, both opposite directions for the electrical polarization would give the same contrast. So it is possible to know the axis of the electric polarization but not its direction.

The geometry of the PEEM experiment is shown in fig. 32. Two linear polarization of the photons are available, vertical polarization of the photons corresponds to X-ray electric field, which determines the beam polarization, totally in the plane of the sample. Horizontal polarization corresponds to photons polarization mostly out of plane, with a small in plane component perpendicular to the vertical axis (Fig. 32).

For in-plane domains, the best contrast is obtained for electronic transitions into the t_{2g} orbitals of lower energy, and with linear vertical polarization of the photon. In this case one can rotate the sample along the normal to the surface axis. Doing so, it is possible

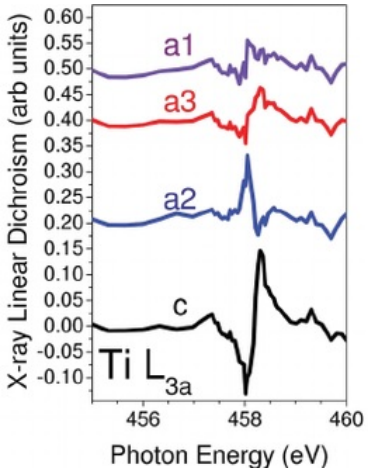

Figure 33 – X-ray linear dichroism ($lh - lv$ polarization) spectra for out of plane domains (c), in-plane domains parallel to lv polarization ($a2$), and the other perpendicular in-plane domain ($a1$ and $a3$), taken from [78].

to get the polarization of the photon beam parallel to the ferroelectric polarization axis for one of the 2 possible in-plane ferroelectric domains, (100) or (010). The domains which are seen darker (lower probability of transition) have their ferroelectric polarization parallel to the photon vertical polarization, whereas the other in-plane domains are perpendicular. It is thus possible to determine the axis of the electric polarization of the BTO domains. To verify that the domains seen are actually in-plane domains, it is possible to take an image with the UV lamp, with which a different contrast should be observed for out of plane domains. The fact that the domain are at 45° in relation to the electric polarization axis also shows that the domains are in-plane. Similarly, an inversion of the contrast happens when taking images for transitions to the t_{2g} orbitals of higher energy, with the same photon polarization, or with the same energy of the photon (i. e. for transitions to t_{2g} orbitals of lowest energy), but with an horizontal polarization of the photon, which then corresponds to a linear dichroic contrast. Thus it is possible to improve the contrast of the image taking the subtraction of 2 images, one with linear vertical (lv) polarization and lower photon energy and the other with the same photon energy and linear horizontal (lh) polarization, or with the same lv polarization and higher photon energy.

It is also possible to take X-ray absorption spectra (XAS) with PEEM, taking several images with different photon energy. Selecting an area in the image, it is possible to make a XAS for this specific area. Doing this for the 3 possible electric polarization axes of BTO domains, with lv and lh photon polarization, and taking the difference of the spectra, enables to get the dichroic contrast for each type of domain, as illustrated in Fig. 33 [78].

2.6.3 Observation of ferromagnetic domains: XMCD images

While taking a PEEM image, it is possible to observe a magnetic contrast (the projection of the magnetic moment on the direction of the X-rays beam) taking the differences of the image with left and the image with right circular polarization at the energy of maximum XMCD signal (corresponding usually to the peak of absorption of the considered edge).

2.7 Auger electron spectroscopy

Auger electron spectrocsopy (AES) is another emission electron technique, it can be used for determining the thickness of a deposited thin film. This method consists on exciting the atoms of a sample with an energetic beam of electrons (between 1 and 5 keV), and collecting the outgoing electrons resulting from the relaxation of those excited atoms.

The emission of Auger electrons is a three electron process. First, an electron from a core level is ionized by an incident electron. Then this hole is filled by another electron from a less energetic level, and the energy liberated during this process is transferred to another electron so that this energy is enough to emit this last electron from the

atom. This last electron corresponds to an Auger electron. The Auger process is named after the initial level of those three electrons, for example KLM, the first letter being the level of the initial hole, the second being the level of the electron which fill this hole and the third the level of the electron emitted. Thus, displaying the number of electrons in function of their energy, some peaks will be visible, corresponding to the emission of those Auger electrons. Auger peaks are characterized by the fact that the energy of those peaks does not depend on the energy of the incident electron beam, but are characteristic of the energy level of the three electrons involved in the process, thus they are characteristic of the corresponding chemical element. The emitted electrons are collected by a cylindrical mirror analyzer, composed of two coaxial cylinders. A negative potential is applied on the outer cylinder, deflecting the emitted electrons and selecting the energy of the electrons reaching the detector. Using a modulation of this potential and a lock-in amplifier to detect the signal enables to have directly the derivative of the number of electrons in relation to the energy, as function of the energy ($\frac{dN}{dE}$), which makes the signal less sensitive to the background of secondary electrons. As the mean free path of this electrons is only a few nanometers (as the energy band measured varies usually between 100 to 1000 eV), only the atoms of the surface are probed. Auger electron spectroscopy enables the characterization of the atoms of the surface and to study the nature of their bonding.

We can calculate the thickness of the film measuring the Auger signal before and after deposition. The thickness d of the film is then $d = -\lambda(E).ln(\frac{I_{AD}}{I_{BD}})$. With $\lambda(E)$ the inelastic mean free path of the of the emitted electron in the material under probe, which depends on its kinetic energy E. I_{AD} the signal of the Auger peak after deposition and I_{BD} the signal of the Auger peak before deposition. In practice, as we have the value

for the derivative of the number of electrons emitted in relation to the energy, instead of observing a unique peak we see a positive peak followed by a negative peak. The value we measure for the signal corresponds to the difference between the maximum of the positive peak and the minimum of the negative peak.

Chapter 3

Results on Multiferroic thin films growth

The first part of this PhD work was dedicated to grow ferroelectric and multiferroic films. For that we used the sputtering setup available as an open user facility at the Brazilian Nanotechnology Laboratory, LNNano. In this chapter we report on the results obtained, in particular section 3.2 describes the growth and characterization of $BiFeO_3$ thin films on $SrTiO_3$ substrates, which were published in reference [79].

3.1 Growth of multiferroic films on silicon substrates

The main reason to grow ferroelectric films on Si substrates was to get used with the sputtering system, once that this kind of substrate is widely available. These films were also used to get acquainted with the characterization techniques. Despite the fact that the following depositions had little success, they were the preparation for the more elaborated ones using more suitable substrates. In the following we describe the systems grew at the very beginning of this work and the results of their characterization.

3.1.1 Growth of $YMnO_3$ on silicon

$YMnO_3$ (YMO) presents two possible crystalline structures: i) hexagonal *h*-YMO: where the Mn ions are located inside an oxygen bipyramids; ii) orthorhombic *o*-YMO: in this case the compound shares the perovskite structure and the Mn ions lie inside oxygen octahedra. In the hexagonal phase it is a multiferroic material with ferroelectric transition at 900 K and antiferromagnetic Néel temperature at 90 K. An important point about the hexagonal phase is that contrary to the perovskite based ferroelectrics, *h*-YMO has a unique polarization axis along the *c* direction. Thus, its polarization can have only two orientations, either parallel or antiparallel to the *c*-axis. This characteristic makes it attractive to devices where the polarization is used to store information. At low temperature, in the antiferromagnetic phase, it presents a strong magnetoelectric effect that has been used to control the exchange bias direction [80].

The samples were grown by sputtering at the AJA system from the LNNano. We used untreated silicon substrates, with the natural oxide layer. To be able to measure the electrical polarization we deposited an aluminum bottom electrode of around 30 nm. Part of this electrode was covered to be exposed after the end of the deposition. We deposited iron as top electrode, which besides serving as electric contact, could eventually play the role of a soft magnetic layer in an exchange-bias device. To avoid the oxidation of the iron layer, another 5 nm of aluminum was finally deposited on the top of the structure.

The final structures were of the type:

Si/SiO_2[native]/Al[30nm]/$YMnO_3$[100nm]/Fe[30nm]/Al[5nm]

The YMO deposition was done at 0.4 Pa of 20 sccm argon and 1 sccm oxygen.

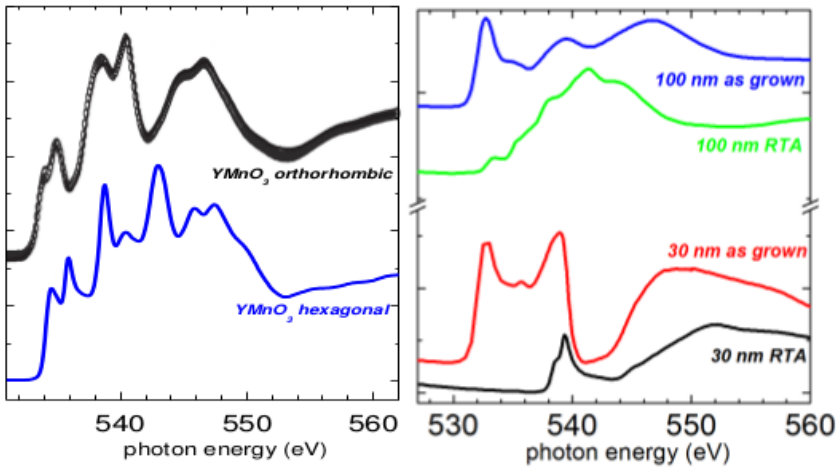

Figure 34 – Oxygen K edge absorption spectra on $YMnO_3$ films. At left is show the reference spectra for both h-YMO and o-YMO. At right the spectra obtained for our samples, as grown and treated by rapid thermal annealing (RTA).

We used a commercial YMO target, and employed 50W of RF power. In the case of Fe and Al the pressure was similar but with argon only, using 80 W of DC power.

The thickness of the several layers was measured with a perfilometer also at LNNano, in special samples where each layer was individually exposed. Some of the samples were subject to a rapid thermal annealing (RTA) in order to obtain the desired hexagonal phase as found in the literature [81]. The RTA treated samples have been annealed to 1123 K for 180 seconds. The warmup and cooldown ramps took less than a minute.

Figure 34 shows the oxygen K edge spectra measured by soft X-ray absorption at the PGM beam line. The results indicate that we did not succeed to obtain a pure YMO phase, neither the hexagonal or orthorhombic. The signal certainly has an important contribution from the natural formed oxide at the surface of the aluminum capping layer. This was the case for both as grown and annealed samples. Furthermore absorption spectra at the Fe L_{23} edges show a diffusion of Fe into the capping Al layer with the RTA procedure. Fig. 35 shows absorption spectra using two detection modes. At left is show

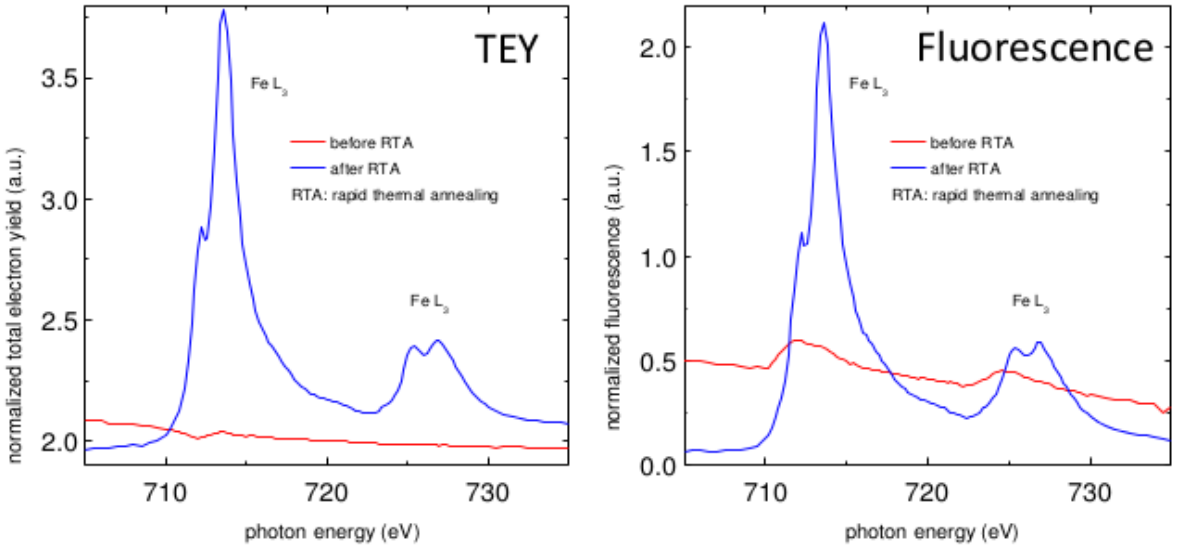

Figure 35 – Iron L_2 and L_3 absorption. The spectra at the left panel were detected using total electron yield (TEY) which gives extremely surface sensitivity to the signal. The right panel shows spectra measured by fluorescence, which are much more bulk sensitive. In both panes is indicated the spectra for the as grown and RTA treated samples.

total electron yield (TEY) results, which are very surface sensitive. In this case we can see that before the annealing the Fe signal was negligible whereas it was present after the RTA treatment. This is a strong indication that Fe migrated towards the surface of the sample. The same measurement was done detecting fluorescence signal (fig. 35-right) which probes more the bulk of the sample. In this case, before the annealing we were able to detect Fe, even if its signal is small. But again, after annealing the signal is much stronger, corroborating the information that Fe migrated to the surface of the sample.

3.1.2 Growth of $BaTiO_3$ on silicon

We grew also $BaTiO_3$ (BTO) films. In order to probe its ferroelectricity, we grew the BTO film on $SrRuO_3$ (SRO) buffer layers. SRO is a metallic oxide at room temperature and is widely used as electrode in complex oxides structures given that it has also the perovskite crystalline structure. Our samples had 100 nm of BTO, 30 nm of

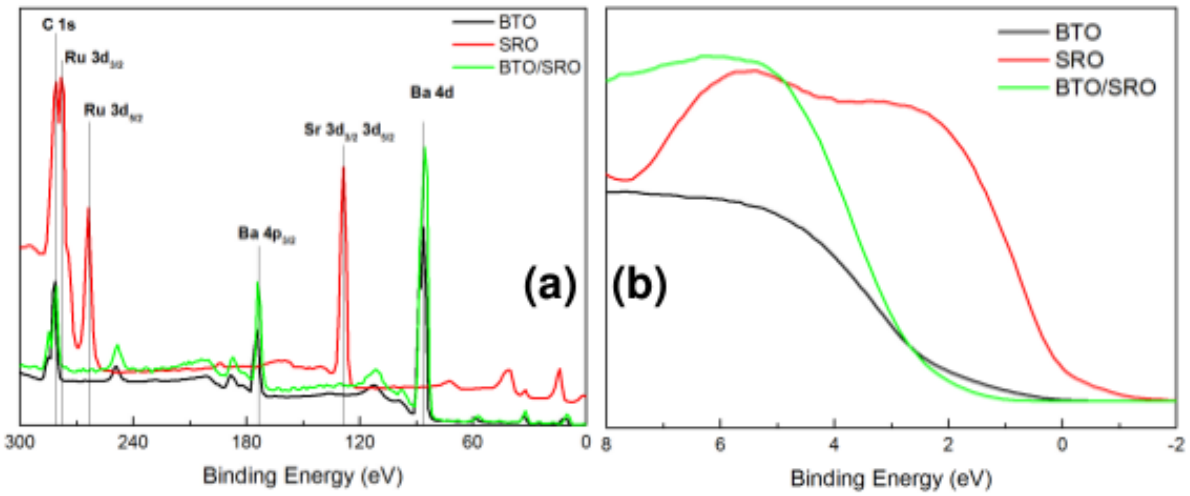

Figure 36 – In (a) we show XPS (X ray Photoemission Spectroscopy) and in (b) UPS (Ultra Violet Photoemission Spectroscopy) of the $BaTiO_3$ samples family.

SRO on SiO_2/Si substrates. We grew also pure BTO and pure SRO films for control. We did not used any capping layer in this case.

The deposition was made by sputtering at the AJA system of the LNNano. We used 0.4 Pa of a mixture of 20 sccm of argon and 1 sccm of oxygen. SRO layer was grew using 75 W of DC power, and BTO 50 W of RF power. The substrate temperature was kept at 573 K in all cases.

We used photoemission spectroscopy to characterize the films. Fig. 36 shows the core levels (XPS) and valence band (UPS) for one BTO/SRO film and the pure BTO and SRO control samples. Again, photoemission is a very surface sensitive technique and its signal arises mostly from the first atomic layers of the sample surface. Both XPS and UPS results show the expected behavior. BTO/SRO and BTO have the same line shape, including a bandgap at the valence band characteristic of insulating materials. On the other hand, SRO displays a metallic behavior with electron occupation up to the Fermi level.

Nevertheless, even if microscopically the samples behaved as expected, the macro-

scopic transport properties were of conducting films in all cases. Thus we were not able to characterize the ferroelectric properties of the BTO film. We believe that this discrepancy between microscopic and macroscopic properties is due to cracks in the BTO film, that allow short circuits between the bottom SRO electrode and the top indium contacts that are normally employed to wire the sample for transport measurements.

3.2 $BiFeO_3$ films on $SrTiO_3$ substrates

3.2.1 Description of the deposition conditions

$BiFeO_3$ (BFO), being one of the few room temperature multiferroic systems, has attracted much attention as thin films, in the view of its potential as magnetoelectric device. Here we report of the growth of BFO films on $SrTiO_3$ (STO) substrates, which share the same perovskite structure as BFO.

The instrument used for sputtering is an ATC Orion 8 from AJA International INC, available in the National Laboratory of Nanotechnology (LNNano).

Seven samples of $BiFeO_3$ have been grown on $SrTiO_3$ substrates, one of $SrRuO_3$ on $SrTiO_3$, and one with a layer of $BiFeO_3$ over a layer of $SrRuO_3$ on $SrTiO_3$. The conditions of sputtering are given in the table 1.

All the samples were grown with an oxygen flow of 3 sccm (Standard Cubic Centimeters per Minute), we did not used argon gas.

As the instrument used is a confocal sputtering system, the distance between the sample and the target is higher than the distance usually given in other references.

label	Target	Power	Thickness	Pressure	T	time	growth rate
S007	BFO	100W (RF)	50-60nm	4 Pa	773 K	7h42mn	8nm/h
S008	BFO	100W (RF)	45-55nm	4 Pa	673 K	6h	8nm/h
S009	BFO	100W (RF)	-	4 Pa	873 K	6h	8nm/h
S011	BFO	100W (RF)	45-55nm	4 Pa	973 K	6h	8nm/h
S013	SRO	150W (DC)	15-25nm	2.6 Pa	973 K	2h	10nm/h
	BFO	100W (RF)	45-55nm	4 Pa	973 K	6h	8nm/h

Table 1 – List of $BiFeO_3$ samples grew by sputtering.

The minimum distance available (that we used for all samples) is approximately 17 cm.

The thickness given in the table have been measured by X-Ray Reflectivity (XRR) for the BFO samples, and it was found to be around 50 nm for S011 and S013, and as the other samples have been grown with the same deposition conditions (except temperature), we suppose that they have a similar thickness. The thickness of sample S009 was not estimated because it shows an important roughness, what precludes us to define its thickness as was done for the remaining samples. For SRO samples, the thickness have been given by comparison of the thickness of other samples grown in the same conditions. Those other samples have been grown at room temperature on silicon substrates with felt pen mark which was easy to remove after the deposition. The difference of height between the film and the zone which had previously the felt pen mark, measured with a perfilometer, gives the thickness of the sample. Although our measurements are not accurate, they allow us to have an idea of the deposition rate value, which enable to compare it to other references.

For every sample, an annealing at the same deposition temperature have been performed. For that, after the deposition, we filled the sputtering chamber with oxygen at 133 Pa (maximum pressure available in the instrument). The duration of the annealing was one hour.

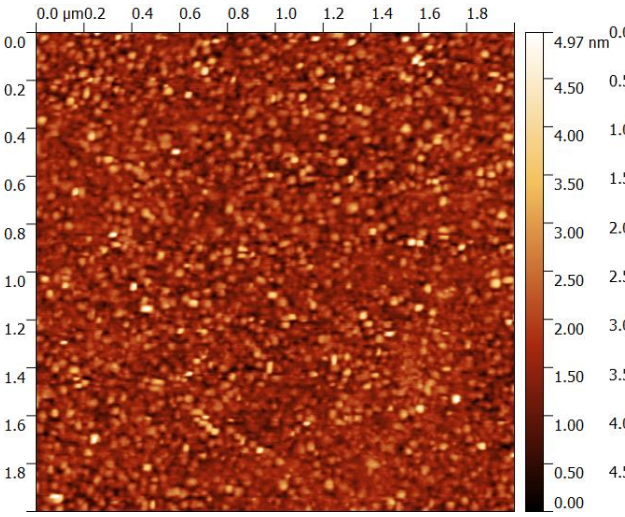

Figure 37 – AFM image of sample S008

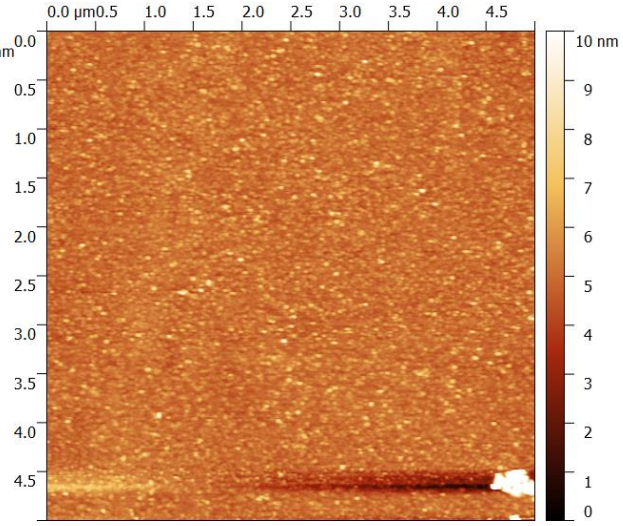

Figure 38 – AFM image of sample S008

3.2.2 Atomic Force Microscopy Results

The topography of the samples has been studied by Atomic Force Microscopy (AFM), with a Park NX10 atomic force microscope (for Fig. 37, Fig. 38, Fig. 39, and Fig. 40), and with a NanoSurf Flex atomic force microscope (for Fig. 41, and Fig. 42), which were available at the LNNANO.

Fig. 37 shows an area of 2μm x 2μm of sample S008 (grown at 673 K). This sample is composed of small grains (the image shows an area of about 50nm). Fig. 38 shows an area of 5μm x 5μm of the same sample. It shows that some grains are bigger than others. The vertical scale reaches around 10nm.

Fig. 39 shows an area of 10μm x 10μm of sample S007 (grown at 773 K). At higher temperature, some bigger grains start to form and result in an increase of the rugosity (the verticale scale reaches around 20nm). But the sample S007 is still mainly composed of small grains.

Fig. 40 shows an area of 10μm x 10μm of sample S009 (grown at 873 K). The S009 sample is mainly composed of squared shaped grains of around 200nm^2 area, and

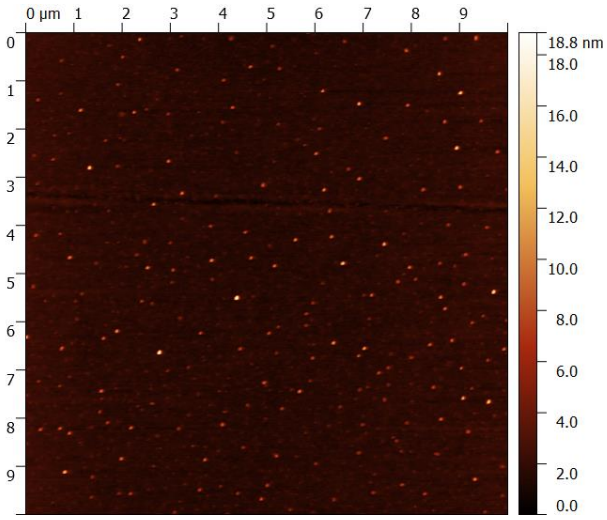

Figure 39 – AFM image of sample S007

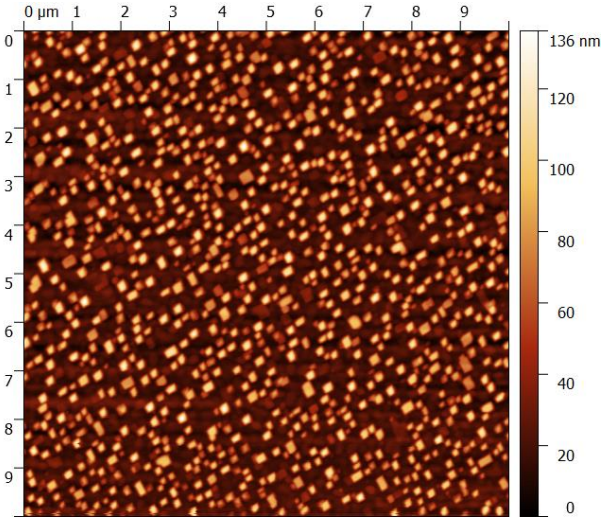

Figure 40 – AFM image of sample S009

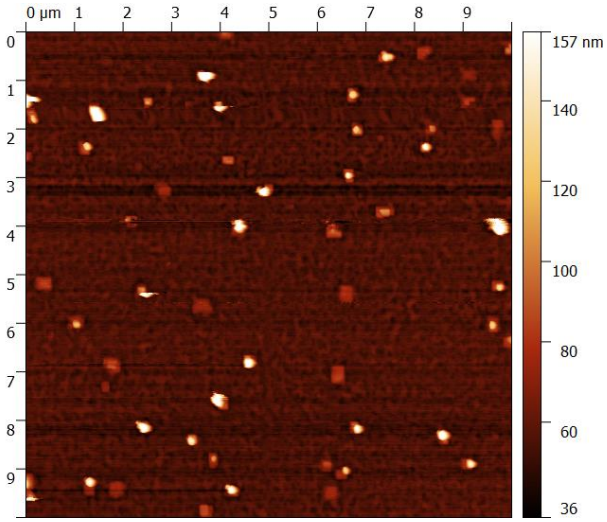

Figure 41 – AFM image of sample S011

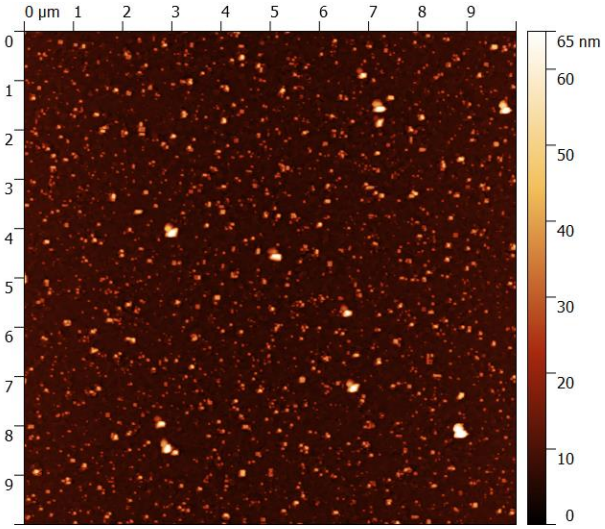

Figure 42 – AFM image of sample S013

with a high thickness (the vertical scales reaches around 100nm). Those squared shaped grains are characteristics of the Bi_2O_3 phase, as can be found in Ref. [82], [83], and [53].

Fig. 41 shows an area of 10μm x 10μm of sample S011 (grown at 700°C). Squared shaped grains are still presents but their number greatly decreased.

Fig. 42 shows an area of 10μm x 10μm of sample S013 (grown at 973 K), composed of one layer of SRO and one of BFO. The topography is similar to the one of sample S011, but with smaller square shaped grains.

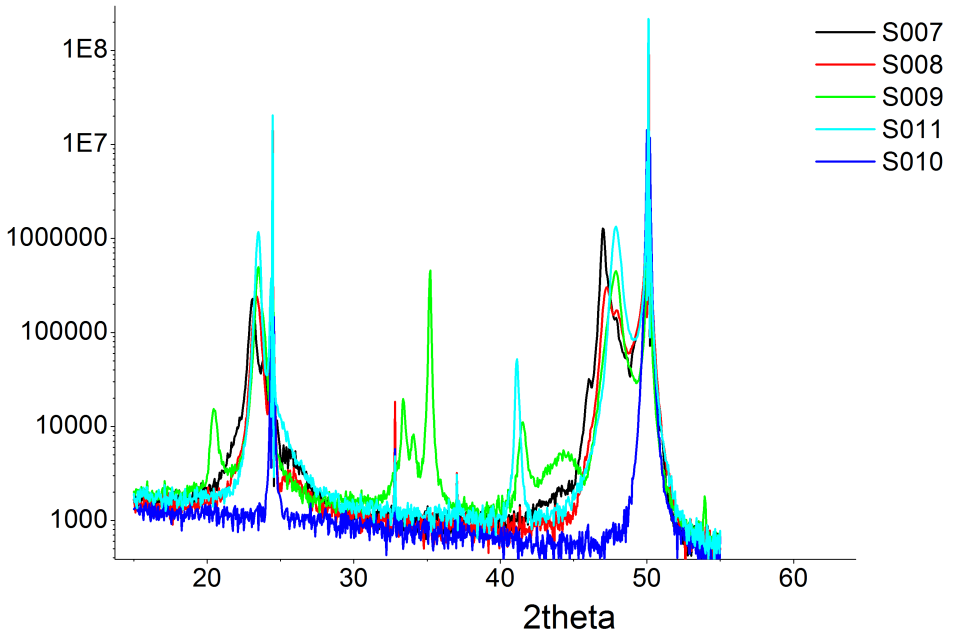

Figure 43 – Diffraction spectra taken with the XRD2 beamline, the vertical scale is given with arbitrary units, and the horizontal in degrees

3.2.3 Diffraction data

Diffraction spectra have been performed for S007, S008, S009, and S011. Two equipments were used, a PANanalytical X'Pert3 MRD, available in the LNNANO, and the equipment of the XRD2 beamline (in the synchrotron of Campinas). As the measurements with synchrotron source gave much more intensity, they are the ones we will present.

We will use the pseudocubic miller index of the crystals, designated in the brackets $(hlk)_c$.

Fig. 43 show all the diffraction spectra. To identify the different peaks, we will use three zooms of this diffraction spectra. Fig. 44 and Fig. 45 shows the first part and third part. We related the Bragg angle θ to the distance between diffracting planes using the Bragg law and the (001)STO peak (lattice parameter of 390.5 pm) to calibrate the

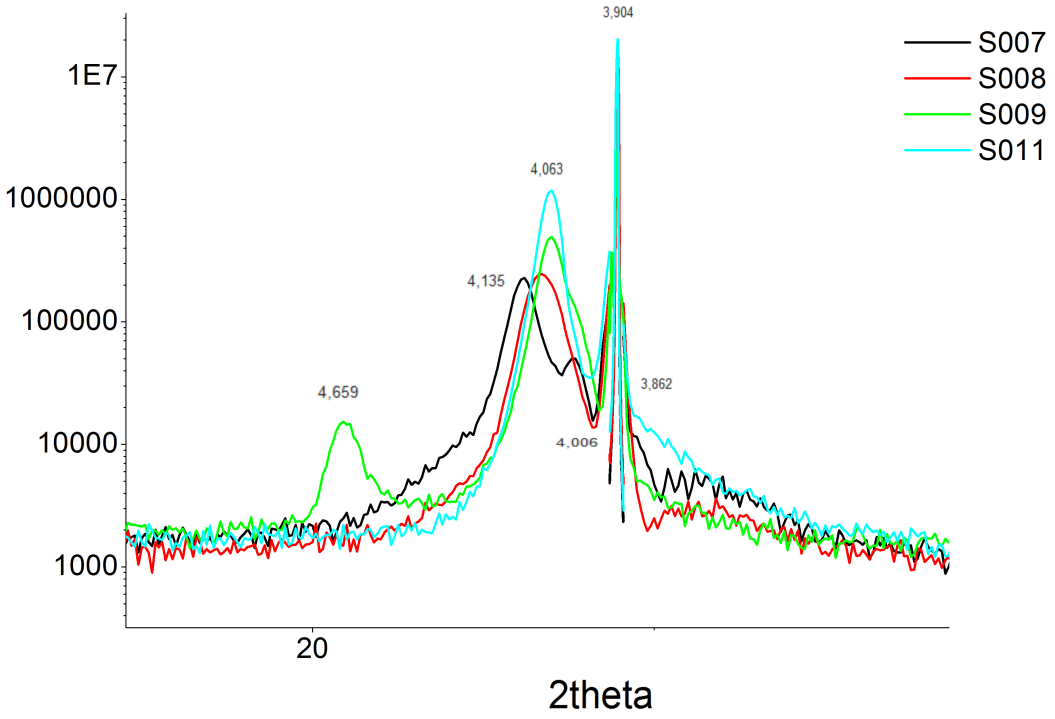

Figure 44 – Diffraction spectra taken with the XRD2 beamline, the distance between the diffraction planes corresponding to the peaks are given in Angtrom

energy. Indeed, we can see two higher and thinner peaks (for which we changed the measurement condition in order to not damage the detector), corresponding to a distance between planes of 195.3 pm for the (002) STO peak and 390.6 pm for the (001) STO peak, in agreement with the theoretical value.

The peaks present on the left of those STO peaks represent the (001) or (002)BFO peaks of the Rhombohedral phase (R-BFO). The evolution with increasing temperature, where at lower temperature (for S008) two peaks are appearing, then for S007, one peak become much more important and then the peak moves to higher values of 2θ, is similar to Ref. [48]. For the samples grown at 873 K and 973 K, the distance between plane for this (001)R-BFO peak, which correspond to the c lattice parameter is 406.3 pm, which is in agreement with other experimental values [46], [48].

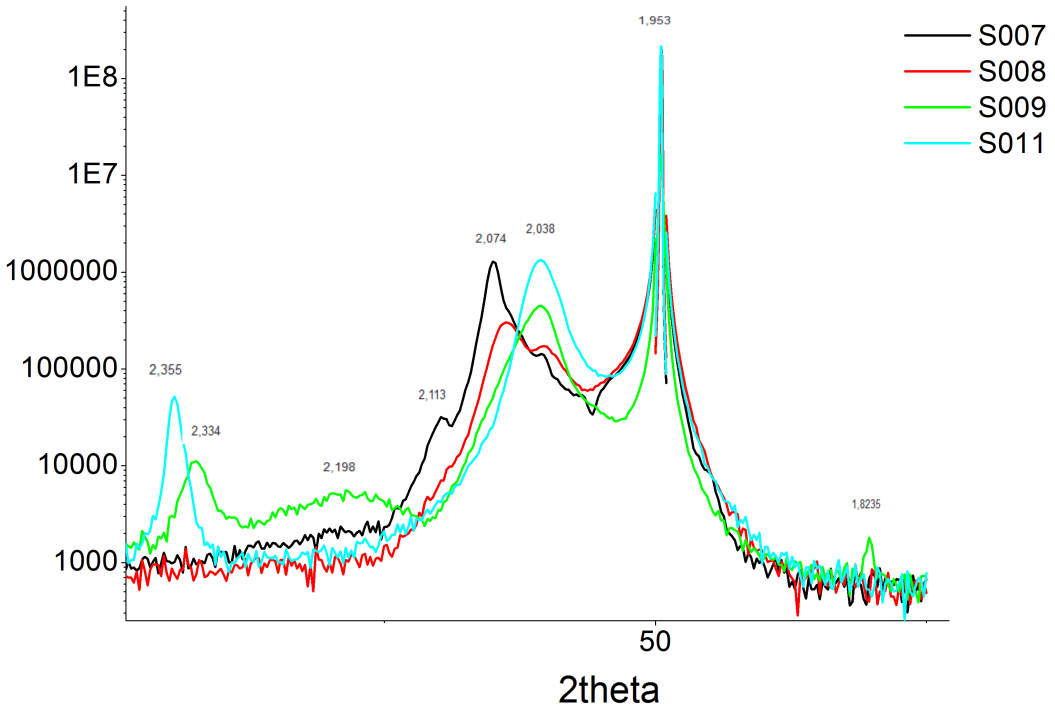

Figure 45 – Diffraction spectra taken with the XRD2 beamline, the distance between the diffraction planes corresponding to the peaks are given in Angtrom

For the sample grown at 873 K two peaks are present related to 469.5 and to 233.4 pm (almost the half of 469.5 pm). Those peaks are not present in the other samples. They seem to correspond to the (001) and (002) tetragonal BFO (T-BFO) peak as the value is coherent with the experimental value of Ref. [48] (1 per cent of difference). This tetragonal phase seems to be related to the presence of Bi_2O_3 phase [48].

Indeed, as we already conclude with the topography results, the S009 sample should contain the Bi_2O_3 phase, whereas the the S007 and S008 samples should not, and the S011 sample should barely contain it (as it contains few square shaped grains). So we expect that some diffraction peaks will be present for the S009 sample and not for the others.

Fig. 46 shows three peaks appearing for the S009 sample and not for the others.

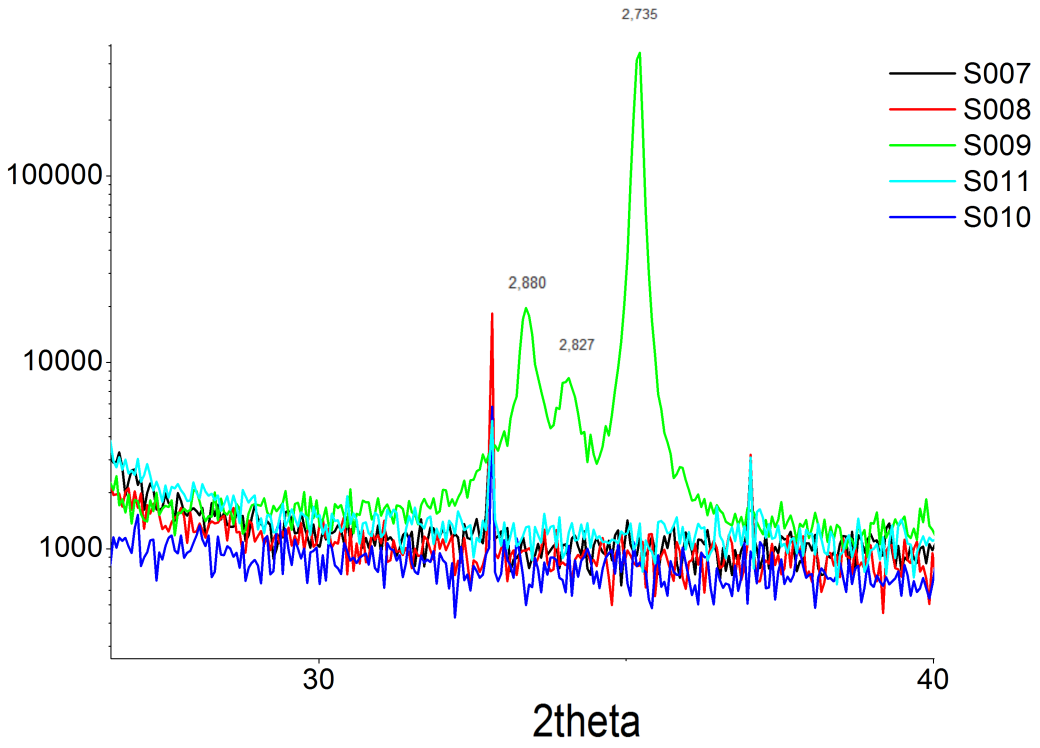

Figure 46 – Diffraction spectra taken with the XRD2 beamline, the distance between the diffraction planes corresponding to the peaks are given in Angtrom

We suppose that those peaks correspond to the Bi_2O_3 phase, at least the thinner and more intense peak related to a diffraction plane distance of 273.5 pm, as the square shaped grains are relatively large and should give thin and intense peaks. It seems coherent with the peaks of Ref. [83]. The peaks related to a diffraction plane distance of 386.2 and 182.3 pm may correspond α- or γ Fe_2O_3 phase [53].

For the S011 sample, grown at higher temperature, the T-BFO, Bi_2O_3, and Fe_2O_3 phases disappear. The (001)R-BFO peak is more intense and thinner, which means the crystallinity of BFO improved. However, an other diffraction peak appeared, related to a diffraction plane distance of 235.5 pm, which were not present in the other samples. Although topography results also showed the presence of square shaped grains, we suppose those grains will not result in diffraction peak as there are really few. We suppose that

this peak comes from (111) oriented R-BFO grains [84].

Part of these samples have their magnetic behavior characterized by SQUID. For some of them we observed a ferromagnetic behavior. Let's remember that BFO bulk in antiferromagnet, but it has been report that in thin films one cold break its cycloidas spins and develop the ferromagnetism from a canted moment. Anyway, it is always advisable to check for spurious origins of such ferromagnetic moment. In our case, from the characterization we presented, we could conclude that it arose from the development of spurious Fe oxide phases. These conclusions were published on [79].

3.3 Growth of $SrRuO_3$ buffer/electrode layers

In order to measure the transport or dielectric properties of a ferroelectric film, it is very important to have suitable electrodes on the sample. To measure the ferroelectric polarization across the film thickness, one can use a top layer electrode of almost any metal, and usually gold is used for this purpose. On the other hand, the bottom electrode must allow the epitaxial growth of the ferroelectric/multiferroic film. In this sense, $SrRuO_3$ is a widely used solution, once that this oxide is metallic at room temperature and shares the same perovskite structure with several oxides. Here we report on the results of fabricating thin $SrRuO_3$ films to be used as bottom electrodes in ferroelectric heterostructures. Thus it is important to obtain a low roughness of the SRO layer.

Ionic bombardment occuring in growth by sputtering is a complex phenomenon, it can improve crystallinity as well as it can introduce defects. For $SrRuO_3$ (SRO) thin films grown with RF magnetron sputtering, it was shown that it could result in the

exchange of Sr ions with Ru ions [41]. Ionic bombardment is increased with lower pressure, higher power voltage and lower substrate/target distance. Here we present the results of $SrRuO_3$ thin film growth on $SrTiO_3$ single crystal substrates by RF magnetron sputtering, with a deposition pressure of 2.6 Pa. We studied the influence of substrate/target distance, temperature and power voltage on the crystallinity and the morphology of $SrRuO_3$ thin films.

We choosed to limit the time of SRO deposition to three hours for most of the samples, so that it will be possible to grow a SRO layer and a BFO layer above it during a same day. For the growth we used an AJA Orion sputtering system, from the Brazilian Nanotechnology Laboratory - LNNano.

3.3.1 Description of the deposition conditions

For most of the samples, we used an oxygene and argon flux of respectively 6 standard cubic centimeters per minute (sccm) of O_2 and 24 sccm of Ar. This low partial pressure of oxygen prevents too much O_2^- anion bombardment into the substrate. Before deposition, the STO single crystal substrates were heated for 30 mn in deionized water with ultrasound and were then annealed for 3 hours at 1073 K. After deposition, a 30 mn post annealing was done inside the sputtering system, with 133 Pa of oxygen, and then the temperature was decreased by 1°C every 10 seconds.

In the following table we present the deposition conditions for each sample. We used an Argon flux of 24 sccm for all samples.

Sample name	S033	S035	S036	S037	S039	S017	S018	S020
Power (W)	100	100	100	80	100	100	100	125
O_2 flux (sccm)	6	4	6	6	6	6	6	6
deposition T (K)	850	850	850	850	850	1023	923	923
deposition time (h)	3	3	3	3	5	3	3	3
S/T distance (cm)	17	17	18	17	19	17	17	17
annealing T (K)	973	973	973	973	973	1023	923	923

Table 2 – Growth conditions of the $SrRuO_3$ samples. Details about deposition temperatures and argon flux are given in the main text.

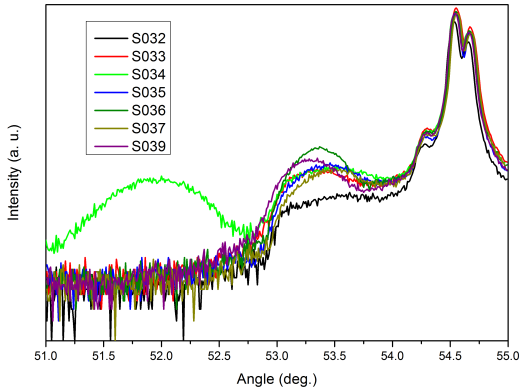

Figure 47 – Diffraction measurements of SRO samples with the Panalytical diffractometer

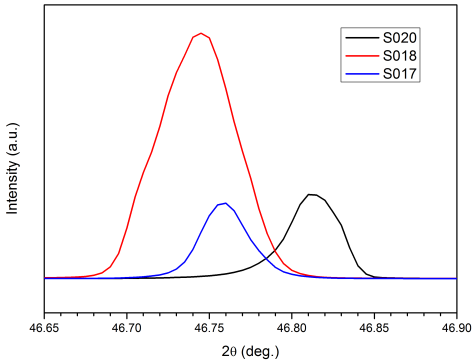

Figure 48 – Diffraction measurements of SRO samples at XRD2 beamline

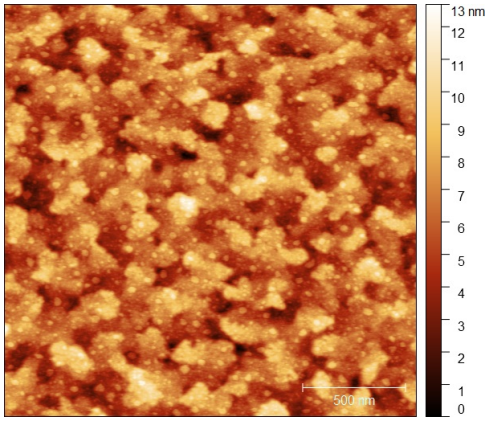

Figure 49 – AFM measurement of a 2x2 μm region of sample S033

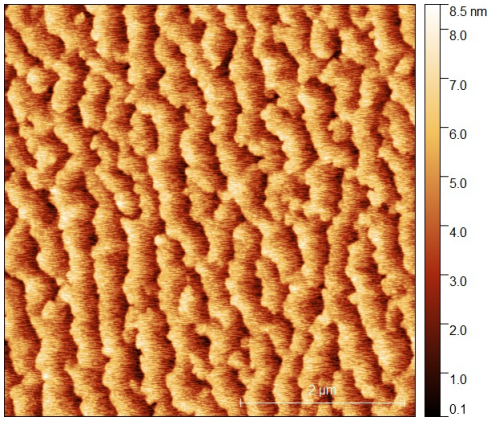

Figure 50 – AFM measurement of a 5x5 μm region of sample S035

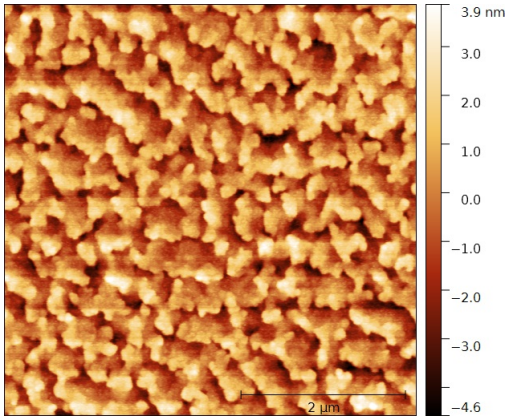

Figure 51 – AFM measurement of a 5x5 μm region of sample S036

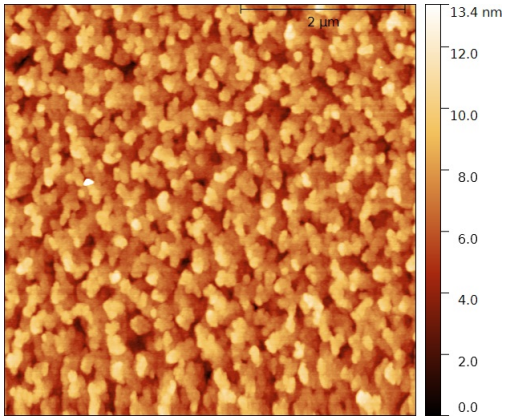

Figure 52 – AFM measurment of a 5x5 μm region of sample S037

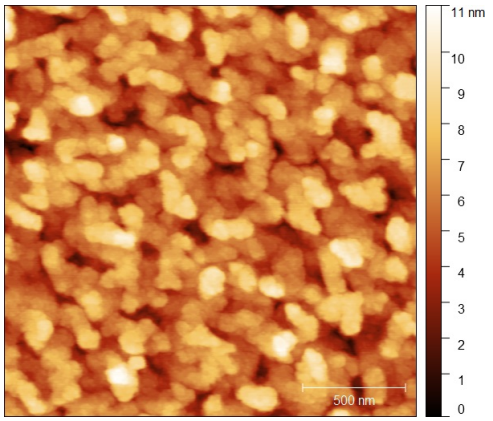

Figure 53 – AFM measurment of a 2x2 μm region of sample S039

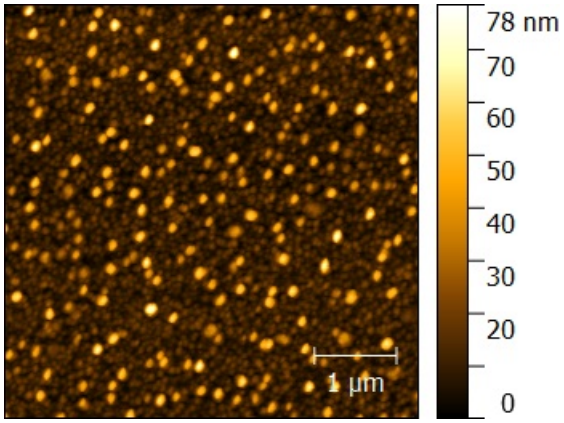

Figure 54 – AFM measurment of a 5x5 μm region of sample S017

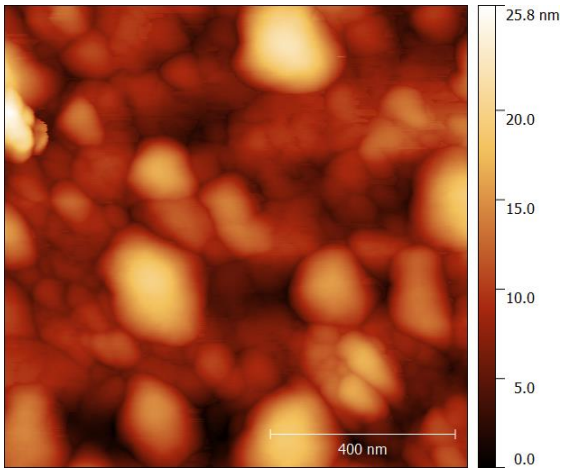

Figure 55 – AFM measurment of a 1x1 μm region of sample S018

Sample name	S033	S035	S036	S037	S039	S017	S018	S020
FWHM of SRO (002)	0.6	0.7	0.5	0.6	0.55	0.6	0.5	0.6
c lattice parameter (pm)	395.8	395.5	395.8	395.4	396.3	394.5	396.2	394.6
Rugosity RMS (nm)	1.7	1.4	1.4	1.7	1.5	10	4	
Thickness (nm)			34	26	27			

Table 3 – Outline of the results obtained for the $SrRuO_3$ films.

3.3.2 Results of SRO growth

Fig. 48, present the θ-2θ diffraction scans taken at the XRD2 beamline of the LNLS. Fig. 47 presents the θ-2θ diffraction scans taken with a Panalytical X pert Pro diffractometer at the LNNano laboratory. Fig. 49, Fig. 50, Fig. 51, Fig. 52,Fig. 53, Fig. 54, Fig. 55, present AFM measurements of the samples.

In the table 3 we sum up the results on the samples morphology and crystallinity, with the full width at half maximum (FWHM), the out of plane lattice parameter c, the rugosity and the thickness.

The thickness of the film was calculated from X-ray reflectivity (XRR) measurements, but not all XRR measurements were good enough to be used.

For samples S033 to S039, the XRD2 beamline of the Brazilian Synchrotron Light Laboratory (LNLS), with which it is possible to have a more intense X-ray source, was not available anymore so we used a Panalytical X pert Pro diffractometer. The full width at half maximum (fwhm) measured from the diffraction experiments gives an indication on the crystallinity of the SRO film.

Comparing samples S033 and S035 (with a slight lower O_2/Ar ratio for S035), we observe from the AFM measurements that the S035 sample grew along terraces, which is characteristic of a 2D mode, whereas it is not the case for the S033 sample. The SRO

out of plane parameter calculated from the SRO (002) diffraction peak is closer to the poder value (0.393 nm [40]) for sample S035, and this peak is also more intense even though this could be due to the fact that sample S035 is thicker (we could not use the XRR measurment for those sample). But the fact that sample S033 has a lower full width at half maximum (fwhm) indicates that sample S035 has not a better crystallinity than sample S033. We did not make AFM measurements for all substrates before the growth, so we suppose that the difference between the 2D and the 3D mode is due to the STO substrate quality, and not to the small changes in the O_2/Ar ratio.

We observe that sample S036 also grow with terraces, so with a 2D mode. Comparing to S033, S036 was done for a higher substrate/target distance, we thus expect a lower thickness for the S036 film. Despite of that, we observe that the SRO (002) peak of the S036 sample is more intense than the S033 one, and it is also thinner, whith a lower FWHM, thus the crystallinity is improved for sample S036. We also grew another sample (S039) increasing even more the substrate/target distance, to see if crystallinity would still be improved. For this sample the deposition time was increased to 5 hours to compensate for the lower deposition rate due to the increase of target/substrate distance. In spite of increasing the time of deposition, the peak of sample S036 was still more intense and thinner, so the optimum target/substrate distance is the one of sample S036.

Comparing sample S039 and S037, sample S037 having the higher target/substrate distance, and sample S039 having a lower power of 80 W, we can observe that the 002 SRO peak of sample S039 is more intense and thinner, and the two samples have a similar thickness. Thus we can conclude that increasing target/substrate distance is more efficient that decreasing the RF power for improving SRO crystallinity, althought it gives a lower deposition rate.

Comparing S033 and S018, with S018 having a higher deposition temperature, we see that the FWHM is reduced at higher temperature, but the roughness also dramatically increase. For S017, grown at even higher temperature, the roughness increased and the crystallinity get worse. Comparing S018 to S020 we see that an higher power pressure lead to a slight increase in the FWHM, and a less intense diffraction peak, although the SRO thin film is expected to be thicker.

3.3.3 Conclusion

In conclusion, the best sample we grew, with better crystallinity and a low roughness with a 2D growth mode, was sample S036. It was grown with an optimized substrate/target distance of 18 cm, a deposition temperature of 853 K,an optimized power of 100 W RF, with an O_2 flux of 4 sccm and an Argon flux of 6 sccm, 2.6 Pa deposition pressure for 3 hours. It was then post-annealed at 973 K (deposition temperature of BFO), for 30 minutes. A higher deposition temperature may improve crystallinity but increase dramatically the roughness. On the other hand our results were not conclusive to see if a lower O_2/Ar ratio would improve the SRO film.

3.4 Growth of $BiFeO_3/SrRuO_3$ on $SrTiO_3$ substrates

We also grew a $BiFeO_3$ layer above a $SrRuO_3$ layer. This time we also used argon gas to grow $BiFeO_3$ as it happened to improve its crystallinity. $SrRuO_3$ was deposited for 2.5h by RF-sputtering with 24 sccm of argon and 6 sccm of oxygen and a total pressure of 2.7 Pa, at 750 K. This deposition was followed by in-situ annealing at the same temperature with 133 Pa of oxygen for 30 minutes. Then $BiFeO_3$ was deposited by RF-sputtering for 3h at a deposition temperature of 973 K, with 9 sccm of argon

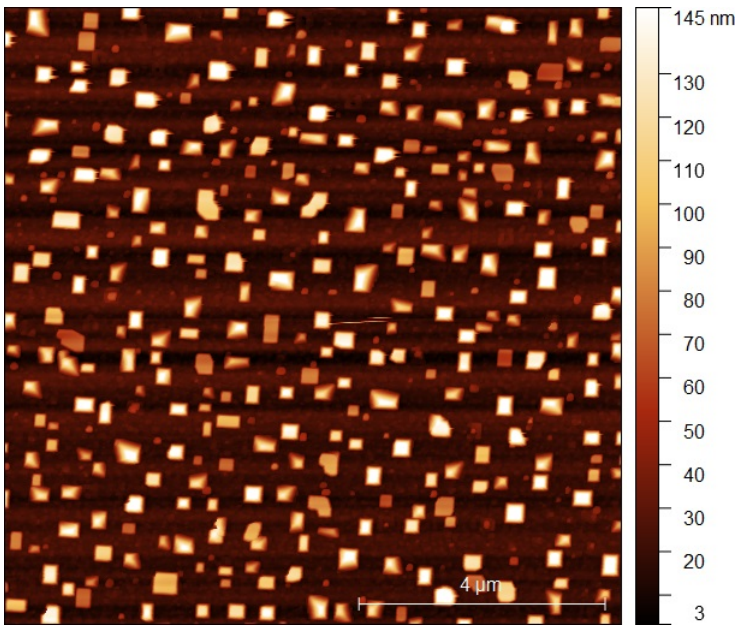

Figure 56 – AFM measurment of a 10x10 μm region of sample S034

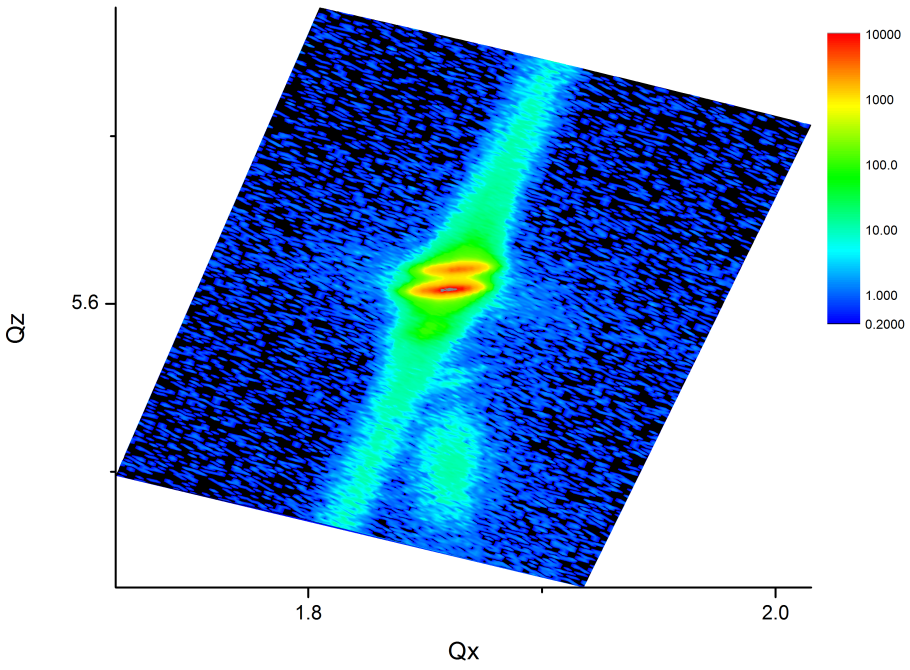

Figure 57 – Reciprocal space mapping around STO peak [103] of sample S034

and 3 sccm of oxygen, and a total pressure of 4 Pa. Both deposition were done with a substrate/target distance of 17 cm and using 100 W. After $BiFeO_3$ deposition, another annealing was done in-situ at 973 K and with 133 Pa of oxygen for 1h.

AFM measurments (Fig. 56) shows the presence of square grains, as for the other $BiFeO_3$ samples described previously. Fig. 47 presents the θ-2θ diffraction scans taken with a Panalytical X pert Pro diffractometer at the LNNano laboratory of sample S034 along with other samples with $SrRuO_3$ only. Besides, a reciprocal space mapping was done for this sample around the [103] STO peak. Fig. 57 shows that both $BiFeO_3$ and $SrRuO_3$ grew epitaxially on $SrTiO_3$ substrates, as they have the same in-plane lattice parameter Q_x than the substrate. The two brigher spots correspond to the STO [103] peak, the peak below these ones, with lower intensity, corresponds to the [103] $SrRuO_3$ peak, and the other peak below, more extended, corresponds to the [103] $BiFeO_3$ peak. We can see that although the $SrRuO_3$ deposition conditions are not exactly optimized as described in the previous part, we succeed in obtaining an epitaxial growth of $BiFeO_3$ and $SrRuO_3$ with good crystallinity.

Chapter 4

Results: magnetoelectric coupling in $Fe/BaTiO_3$ heterostructures

In this chapter we report on what we consider are the most important contribution of this PhD work. We will present the results on the magnetoelectric coupling between the magnetic and ferroelectric domains of the Fe thin films grew on $BaTiO_3$ monocrystalline substrates.

This study has been done in collaboration with the group leaded by Prof. Claus M. Schneider, from the Forschungszentrum Jülich, Germany, and Dr. Slavomir Nemsăk, beam line responsible of the UE56 SGM beamline of the synchrotron BESSY II, an instrument from the Helmholtz Zentrum Berlin, Germany. This group runs a photoemission electron microscopy (PEEM) program at BESSY II lab, with an instrument of the same model of that installed at the PGM beam line, LNLS, Campinas, Brazil.

The collaboration included a 5 months internship of the student at the synchrotron in Berlin. This period had a two fold purpose: i) get experience in the use of the instrument that is available at Campinas, within a specialized group; ii) learn how

to apply PEEM techniques to study ferroelectric/multiferroic materials. The research performed during this internship complemented that of Hatice Doganay 's [10], a PhD student in that group.

One must notice that these results depend on the use of synchrotron radiation both at Berlin and Campinas. The access to beam time is always reduced and for what follows the measurements were concentrated on a couple of weeks of beam time (shared with other projects) during the first half of 2016 at BESSY, one week of beam time in Campinas in the second half of 2016 and finally another week of beam time at BESSY at the end of May, 2017.

In sample preparation strategy was the following:

1. Prepare the surface of the $BaTiO_3$ (BTO) substrate;
2. In the case of the first experiment in Berlin, we observed the BTO ferroelectric domains with X-ray linear dichroism (XLD) at Ti L_3 edge using the PEEM.
3. Grow an Fe thin film on the BTO substrate. This was done *in-situ* for the first measurements in Berlin and *ex-situ* for next ones;
4. Observe the Fe ferromagnetic domains using X-ray circular dichroism (XMCD) at the Fe L_3 edge using the PEEM, as was mentioned in section 2.6.3 and will be further detailed below.

We did not pre-characterize the ferroeletric domains for the *ex-situ* experiments because the annealing ends up changing the domain configuration.

One observation concerning all the PEEM results: in several PEEM images the X-ray beam direction is represented by an arrow drawn on the image. This arrow does not point to any particular feature of the figure. This indication is important and will help in the data interpretation in following way:

XLD X-ray linear dichroism is sensitive to the variations in the BTO's lattice parameter due to the ferroelectric polarization. Notice that XLD is sensitive only to the orientation of the polarization axis, and not the direction in which the polarization points. The contrast will depend on which feature of the absorption spectra will be used. It is important to keep in mind that the electric field direction of the X-rays photons is perpendicular to the direction indicated by the arrow, completely in the plane of the image for liner vertical photon polarization and mostly out of plane for linear horizontal polarization, as explained sketched in fig. 32.

XMCD X-ray circular dichroism is sensitive only to the magnetization component projected along the X-ray beam direction. This is valid in any case. Furthermore, within our definition, the contrast is brighter for magnetization parallel to the beam, darker if the magnetization is antiparallel to the X-ray beam direction. Magnetization perpendicular to the X-ray beam will result in a mid-shade of gray contrast.

A second point about PEEM images: in their caption we indicate the field of view (FOV) of the images. This corresponds to the diameter of the area imaged on the sample and it is bounded by the circular area in the images. Out of the field of view the image is fully dark.

In the next sections we will separate the results by each round of beam time.

There were earlier attempts for the *in-situ* experiments while in Berlin, but they were not conclusive and are not reported here. We conclude the chapter discussing the results.

4.1 First experiment: *in-situ* growth of Fe on $BaTiO_3$

Here we report on the results obtained in our first visit to the synchrotron BESSY when we actively participated in all the steps of the sample preparation, instrument and beam line operation.

4.1.1 Observation of ferroelectric domains

For the experiments we used single crystals BTO, one side polished, from SurfaceNet GmbH. After the crystal treatment, ferroelectric domains were observed with PEEM around the Ti L_3 edge. Fig. 58 shows stripes domains for photon energies of 456.9 eV (left panel) and 457.4 eV (right panel), with vertical photon polarization. The contrast is weak but it is reverted for the two images. In the following we recall how the ferroelectric orientation is obtained from the XLD measurements based on the discussion of section 2.6.2.

Ti in $BaTiO_3$ has 4+ ionization state and thus it has a $3d^0$ occupation. This implies that all the t_{2g} orbitals contribute to the X-ray absorption signal, remembering that at this energy range we are probing the $2p$ to $3d$ transitions. Nevertheless, from fig. 31 in section 2.6.2, one sees that the Ti t_{2g} levels split due to the tetragonal distortion that takes place at room temperature. The t_{2g} orbital perpendicular to the tetragonal distortion has the lowest energy, and consequently is located to the low energy scale of the t_{2g} absorption peak show in fig. 31, which in our case corresponds to 456.9 eV. On the other hand, the high energy side of the t_{2g} absorption peak, at 457.4 eV, is related to the

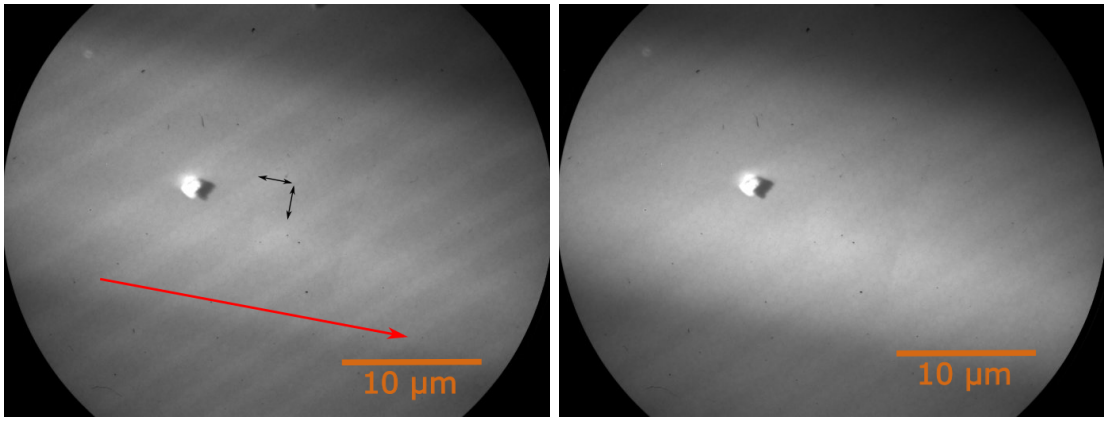

Figure 58 – 40 μm field of view (FOV) PEEM images using linear vertical polarized photons. In this case the X-ray electric field is in the plane of the sample, perpendicular to the X-ray beam direction indicated on the left panel by the red arrow. The black double arrows indicate the electric polarization direction for each region. At left it was used a photon energy of 456.9 eV, whereas at right it was used 457.4 eV. Each of these energies probes empty states in a given Ti t_{2g} orbital (section 2.6.2). Notice the inversion in the contrast between the two images. See text for details.

other two t_{2g} orbitals. Thus if the tetragonal distortion and consequently the ferroelectric polarization is aligned with the photon propagation direction, then electric field of the photons will be aligned with the lower energy t_{2g} orbitals, making the transition at 456.9 eV stronger than that at 457.4 eV.

This means that using 456.9 eV, the domains with ferroelectric polarization along the beam will be brighter than domains perpendicular to the X-ray beam. Similarly, tuning the X-ray energy to 457.4 eV will make brighter domains with ferroelectric polarization perpendicular the X-ray beam. The contrast is not very strong but is noticeable in fig. 58. One can notice that changing only the energy of the photons the contrast is reversed. In order to improve this information, fig. 59 shows the subtraction of the two images. In this case, the image with 457.4 eV (right panel of fig. 58), was subtracted pixel by pixel from the image taken at 456.9 eV, in such way that brighter regions denote domains with ferroelectric polarization aligned with the X-ray beam.

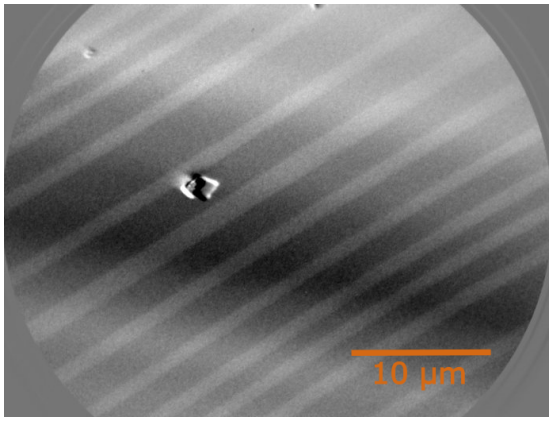

Figure 59 – subtraction of the 2 PEEM images, with 40 μm FOV

The difference shown in fig. 59 is typical of ferroelectric domains in the plane of the BTO substrate, denoted a_1, a_2 domains, each one along either the (100) or (010) crystallographic directions along the surface of the sample. Notice that as expected from previous results (see section 1.5.1) the ferroelectric polarization is at 45°from the domain wall. From these XLD results we are able only to know the axis of the ferroelectric polarization, but not the direction it points. It is worth noting that in these images there is also some broad variations of intensity, which are easily seen in the difference image 59. This is an instrumental effect, given that at the U56-SGM beam line at BESSY, the vertical beam size was around 40μm, being of the order of the used FOV. The broad variations are related with the intensity structures within the X-ray beam.

At 456.9 eV photon energy and with linear vertical photon polarization, the sample was rotated around its surface normal until getting the best contrast. We can thus identify the darker domains of Fig. 58, left panel, as domains with their electrical polarization parallel to the photon polarization. The stripe structure corresponds to in-plane domains, with their axis of polarization at 45° of the domains boundaries to avoid charge accumulation at the domain walls, as represented in fig. 5. In plane ferroelectric domains usually show also 180° domain walls, (Fig. 30), which we can not observe here because

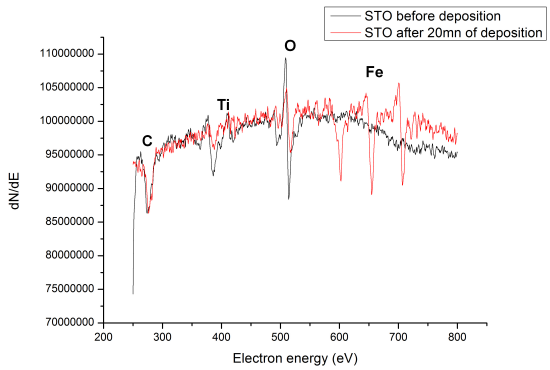

Figure 60 – Auger spectra of an STO sample before and after 20 mn deposition of Fe

the XLD contrast is not sensitive to opposite directions of the ferroelectric polarization. In other words, XLD-PEEM allow us to visualize in plane a_1 and a_2 domains, which are at 90°from each other, but does not give information about the potential 180°domains within the same a_1 or a_2 region.

4.1.1.1 Thin Fe film deposition

The LEEM/PEEM in Berlin is connected to a preparation chamber, containing, among others, evaporators and an Auger electron spectrometer. This allows to grow Fe thin films without breaking the vacuum. After observing the ferroelectric domains of BTO, we transfered the sample to the preparation chamber to deposit Fe *in-situ*. In order to know the thickness of Fe that we deposited we did Auger electron spectroscopy *in-situ* on a $SrTiO_3$ substrate with the same conditions of deposition that we used for the deposition of Fe on BTO, namely e-beam evaporator high voltage of 990 V and 1.90 A for the filament, corresponding to 12 mA of emission. We observe that prior to loading the substrate into the PEEM instrument, we did a scratch on the substrate to use as reference guide. Thus, we can image the same region before and after the deposition.

We calculated the thickness of the Fe film measuring the Auger signal before and after deposition. The thickness d of the film is then $d = -\lambda(E).ln(\frac{I_{AD}}{I_{BD}})$. With $\lambda(E)$

the inelastic mean free path (in Fe) of the emitted electron at its corresponding energy, I_{AD} the signal of the Auger peak after deposition and I_{BD} the signal of the Auger peak before deposition.

The values of inelastic mean free path in Fe were read in a graph from [85], which gave around 1 nm for an energy of the electrons of around 510 eV (energy of the emitted Auger electrons for the oxygen peak) and 0.8 nm for electron energy of around 380 eV (Ti peak).

During the deposition on the STO sample, the current of emission was 11.5 mA, and we deposited for 20 minutes. The calculation gave a thickness of 0.67 nm from the Ti contribution, and 0.78 nm from the O contribution. We assumed a mean value of 0.72 nm for 20 minutes of deposition.

The deposition on the BTO sample was controlled in 40 minutes of deposition with similar parameters, so we expect a thickness of around 1.5 nm.

4.1.2 Observation of ferromagnetic domains

The magnetic domains of Fe were observed with X-ray magnetic circular dichroism (XMCD) contrast at the Fe L_3 edge, corresponding to photon energy of 707.7 eV. The final images are an average of 50 acquisitions, each one taken during 4 seconds. To improve the spatial resolution, a 20 μm aperture was used. In fig. 28 this aperture is named *entrance slit*.

Fig. 61 show XMCD-PEEM images at Fe L_3 edge for three different azimuthal angles of the sample. By azimuthal here we mean rotation of the sample around its surface normal. We define here the angles relative to the XLD-PEEM image of the ferroelectric

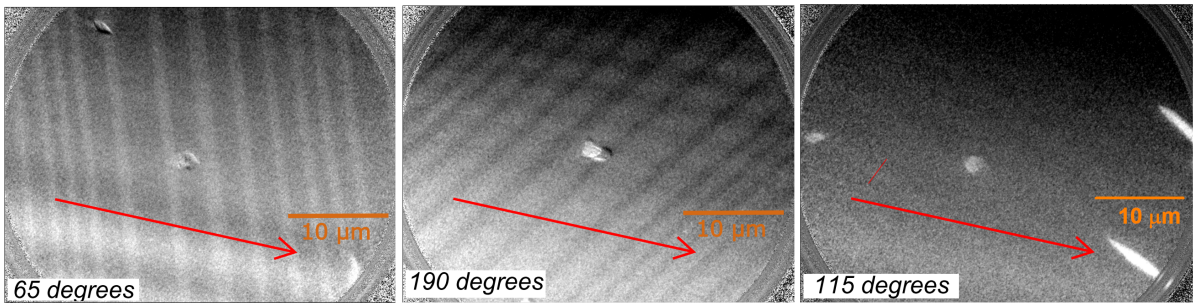

Figure 61 – XMCD PEEM image taken at Fe L_3 edge with the sample rotated at several angles relative to the image of ferroelectric domains. Images taken with 40 μm FOV.

domains show in fig. 59. The intention was to rotate the sample until the magnetic contrast was maximized. Then rotating it again until it gets to a minimum, and keep rotating until the contrast is reversed. This would allow us to determine the direction of the magnetization within the magnetic domains. We would like to point out that given the limited amount of beam time, we had no possibility to fine tunning the rotation.

We can see in the XMCD images on Fig. 61 a weak ferromagnetic contrast, which is reverted for the two images at 65 and 190°, reproducing the contrast of the ferroelectric domains. The matching between the ferroelectric and ferromagnetic can be checked in fig. 62, where we put together part of the image in fig. 59 and part of the XMCD image at 190°. This last one was rotated accordingly. We can notice a one-to-one correspondence in the domains, despite the fact that the magnetic contrast is much weaker. This is an important result, showing that for Fe films of around 1.5 nm the ferroelectric domains really determine the shape of the magnetic ones. We noticed that a similar result have been obtained previously in the same group during the PhD thesis the of Hatice Doganay 's [10]. But in that case it was used an Fe film of 3.2 nm, and even if it was clear the dependence of the magnetic domains on the ferroelectric configuration, the correspondence was not complete. This is probably due to the thicker Fe film, where the Fe atoms further away from the interface are less sensitive to the ferroelectric domain

imprint.

Now we discuss about the magnetization direction in the domains. The panel for the image at 115° in fig. 61 shows a very faint indication of the magnetic domains, with a very low contrast. Nevertheless, given that even at this angle we can still observe the domains, we can not deduce the direction of the magnetization unequivocally with only these three images. But the contrast seen for the different angles of rotation of the sample would be coherent with a difference of magnetization perpendicular to the stripes (and so it would not be parallel, nor perpendicular, to the direction of electric polarization of the ferroelectric domains above). From the image at 115°, given the homogeneous lack of contrast, one could say that the magnetization in all the image is almost perpendicular to the X-ray direction, given that XMCD is sensitive only to the magnetization component project in the X-ray direction. This would mean 180° magnetic domain walls at the stripes boundaries. If this is the case, then the magnetization direction would be 45° of the ferroelectric polarization. But again, more measurements would be needed to fully determine the magnetization of such domains. This would require synchrotron beam time beyond what as available at the time of this experiment.

4.2 Second experiment: *ex-situ* measurements in Campinas

We also did those experiments in Campinas, but instead of depositing Fe *in-situ* the deposition was done *ex-situ* in Jülich by Thomas Jansen (Forschungszentrum Jülich). The BTO sample used for this deposition had already been used for a Fe *in-situ* deposition and was cleaned by argon sputtering for 2 hours and 40 minutes with 1.3 keV energy within a pressure of 4×10^{-4} Pa of argon and 10 mA emission current, followed by 1 hour of annealing at 973 K with 4×10^{-4} Pa of O_2.

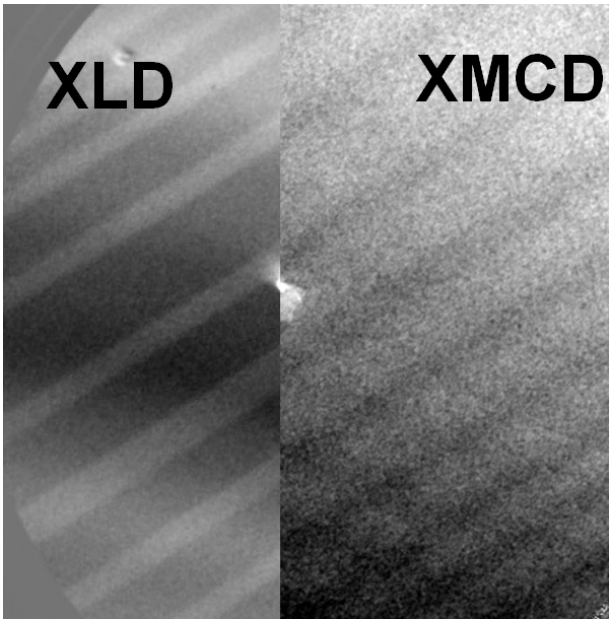

Figure 62 – Comparison of the XLD and XMCD contrast from images taken with 40 μm FOV

The BTO substrate was heated at 923 K for 120 minutes in a MBE chamber and then cooled down to room temperature. The deposition consisted of a wedge of Fe, with thickness ranging from 0 to 5 nm, with a MgO capping layer of 0.8 nm. All this procedure was done by our collaborators in Jülich.

In this case we were not able to directly probe the ferroelectric domains by XLD at the Ti L_3 edges as we did before. We tried to observe the Ti signal, but it was too noisy to be useful. This is due to the PEEM surface sensitivity. As we have the Fe and MgO on top of the BTO in this case, these top layers prevented us from measuring XLD to determine the ferroelectric domains. But as we have already confirmed in the previous *in-situ* experiment that there is effectively a coupling between the ferroelectric and magnetic degrees of freedom, we searched directly for Fe domains in the form of parallel stripes similar to those observed during the *in-situ* experiment.

At first it was hard to see ordered magnetic domain in XMCD images. For most of the regions we observed not ordered domains like fig. 63, which are characteristic of

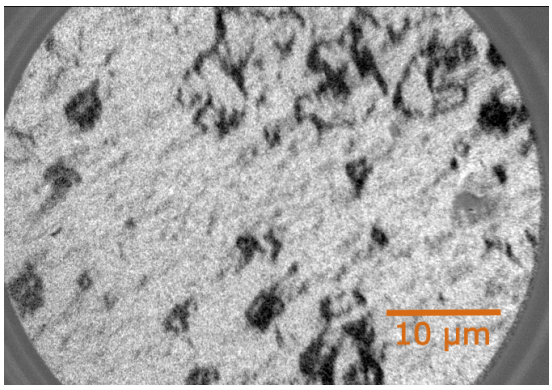

Figure 63 – XMCD PEEM image taken at Fe L_3 edge in a region without magnetoelectric coupling. In this case we see random magnetic domains. This was taken at the thicker region of the Fe wedge.

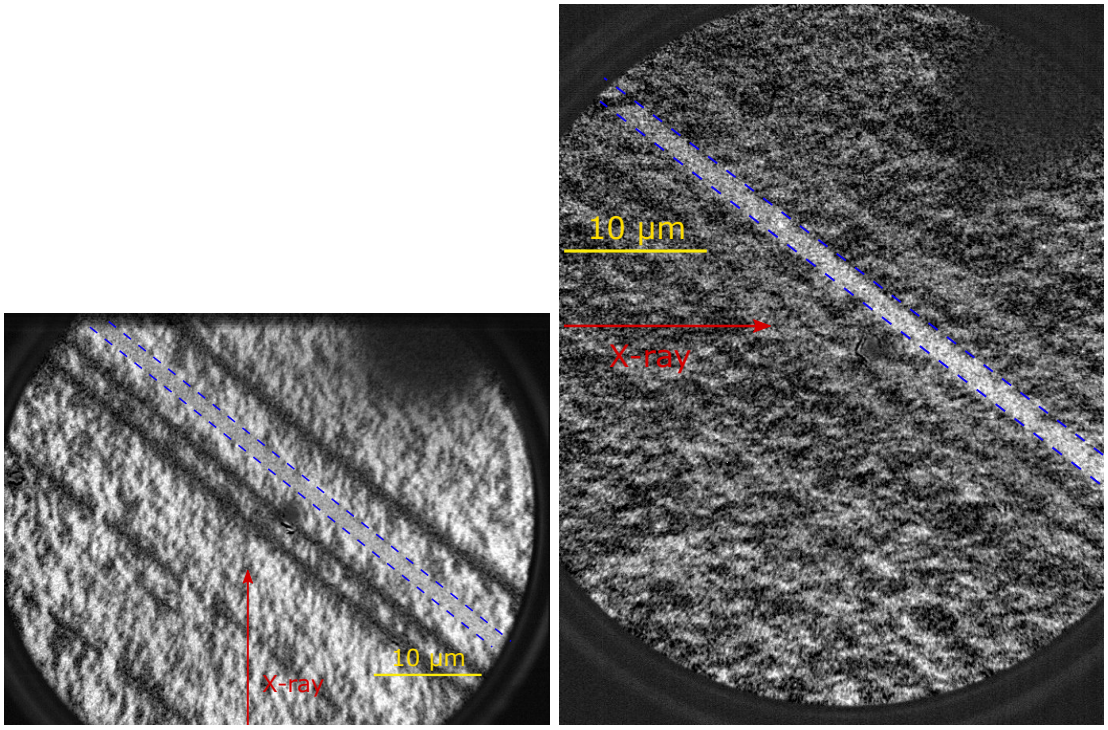

Figure 64 – XMCD PEEM image taken at Fe L_3 edge. At left the region between the blue lines shows a region without contrast compared to the other regions which show white and black contrast. At right, the sample was rotated by 90° in relation to its previous position at left. The region between the blue line is now much brighter than the other regions. Notice the different X-ray beam direction in each panel, indicated by the arrows. In this case we rotated the left image to make it directly comparable with the right one.

magnetic domains not coupled with the ferroelectric substrate. This kind of domains pattern was observed in most of the sample with thicker Fe layers.

For a region with a thinner Fe layer, we observed some order in the pattern of the domains. Fig. 64 presents the image of the Fe domains of this region for two azimuthal angles rotated by 90°. In those figures, some ordered domains are visible (black or white lines) for one angle, whereas they show almost no contrast for a rotation of the sample of 90°. This enable us to determine the direction of the magnetic moment in those lines. This direction would be in accordance with a coupling with the ferroelectric domains of BTO (with the axis of the ferroelectric domains at 45° from the stripes). But we notice a granularity in the images that can not be associated with its topography, which means that it is of magnetic origin. This can be an indication that the magnetoelectric coupling is not complete in this sample.

The incomplete magnetic coupling could be due a low crystallinity of the Fe layer. In order to check for that, we tried a soft annealing on the sample at around 423 K. This procedure was done directly on the PEEM and was following by imaging. During the annealing we saw an improvement of the magnetic contrast and after decrease of the temperature below the BTO tetragonal phase transition, we saw a completely different domain pattern coherent with the fact that after going back to a temperature inferior to the transition temperature, the ferroelectric domains of BTO changed. Also, after the annealing the iron oxidation considerably decreased (Fig. 65), indicated by the reduction of the structure at the high energy side of the L_3 edge. As mentioned, the improvement of the magnetic contrast could be due to an improvement of Fe crystallinity during annealing.

Fig. 66 shows the Fe magnetic domains after annealing for the same region as in

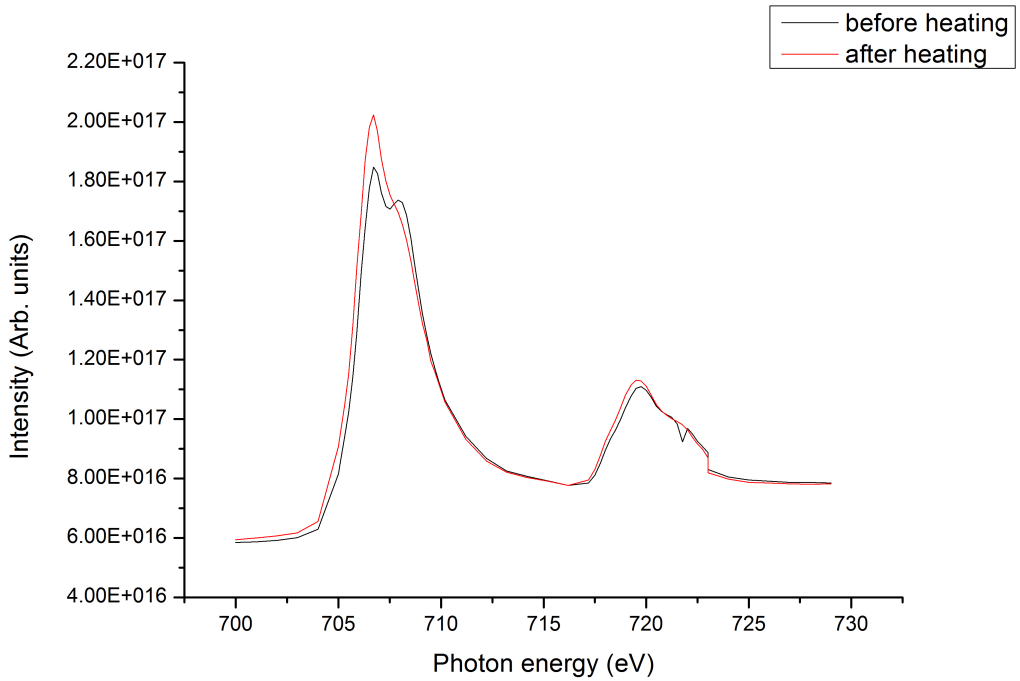

Figure 65 – XAS of Fe L_3 and L2 edges before and after heating, the spectra were taken from images of $70\mu m$ FOV

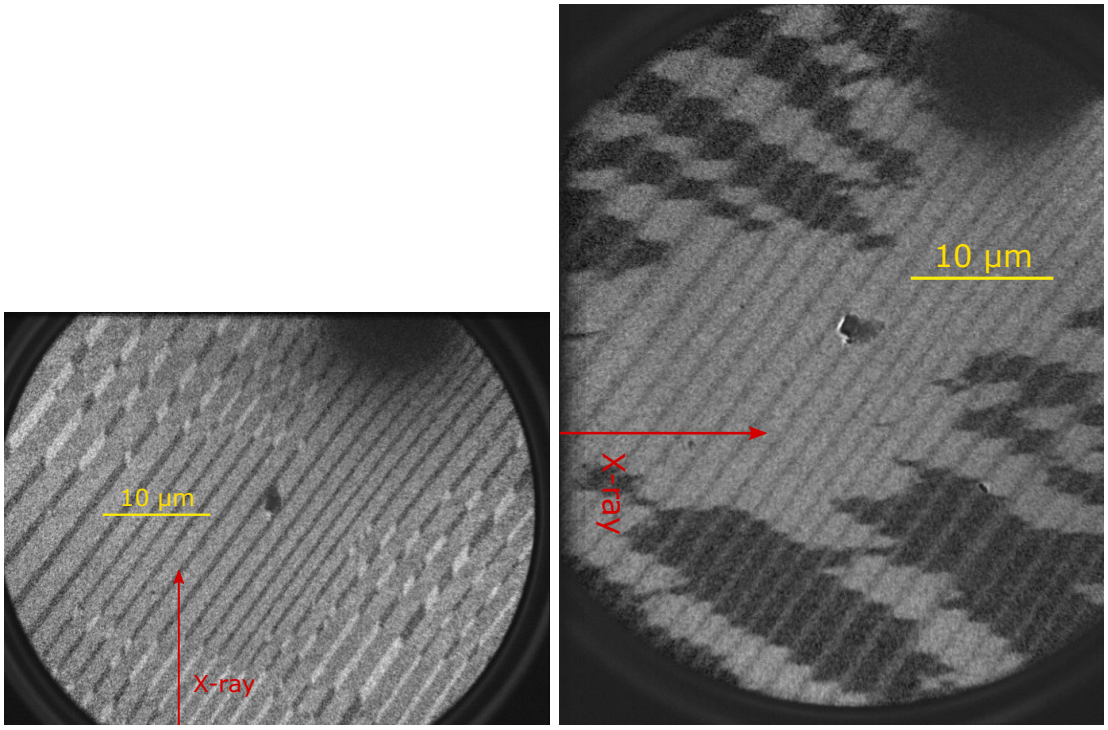

Figure 66 – XMCD PEEM image taken at Fe L_3 edge after annealing. The quality of the magnetic contrast increased and one can observe several *hering bone* type structures.

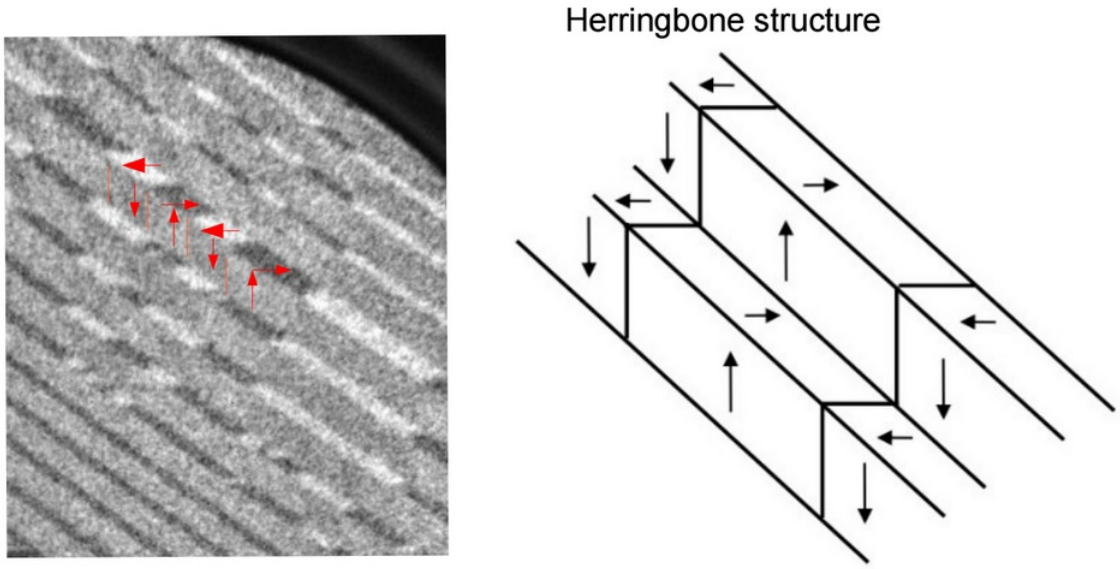

Figure 67 – Image of the Fe ferromagnetic domains with the direction of some domains (red arrows) and at right the similar herringbone structure

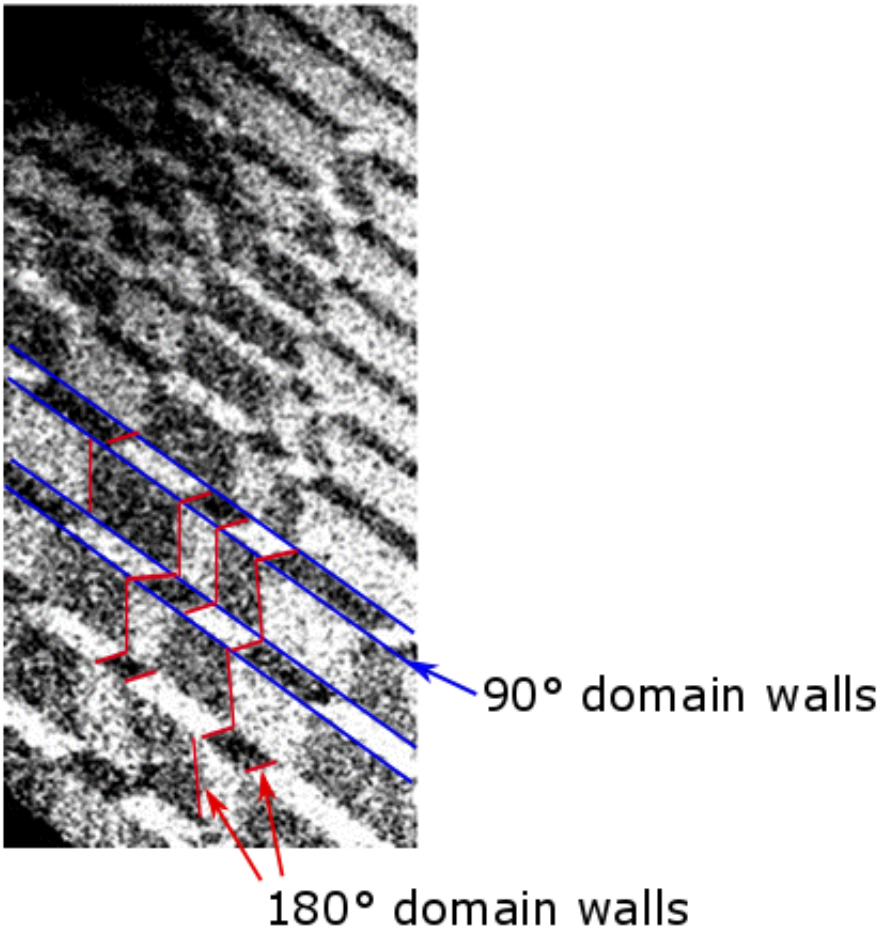

Figure 68 – Superposition of the 2 xmcd images with 90°diferent angle.

Fig. 64. We see that some regions have no contrast, whereas other have black and white contrast. After turning the sample by 90°, the contrast changed, the regions which had no contrast before shows a white and black contrast whereas the regions which before had contrast do not have contrast after rotating. We can thus deduce the direction of the magnetic domains. Fig. 67 shows that the Fe domain pattern have an *herring bone* structure which is a possible domain pattern for ferroelectric domains. We have thus an imprint of the BTO ferroelectric domains to the Fe ferromagnetic domains.

From fig. 67, we observed several magnetic domains with opposite magnetization within the same stripe. These domains have 180°walls, and we have two possible explanations for their appearance:

Minimization of magnetostatic energy The creation of several smaller domains could decrease the overall magnetostatic energy of the system. To check that it would be interesting to perform micromagnetic simulations;

magnetoelectric couplig As observed in section 4.1.1 XLD is able to determine only the axis of the ferroelectric polarization and its direction. Thus it would be possible to have 180°ferroelectric domains within one stripe. In this case, then the ferromagnetic domains could be reflecting the underlying ferroelectric configuration.

We believe that the most plausible explanation is the reduction in the magnetostatic energy. But this must be further verified, because if the second possibility proves to be correct, then the magnetic domains depend not only on the orientation of the ferroelectric polarization, but also on the direction it points. This would be a very interesting behavior for eventual devices based on this kind of system.

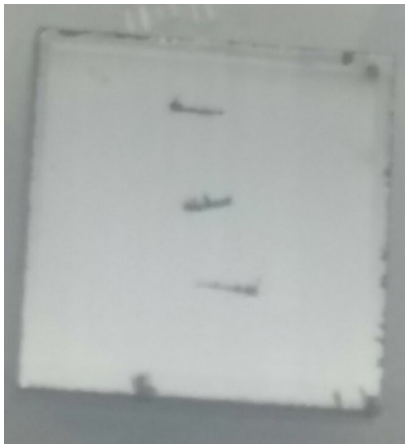

Figure 69 – BTO substrate with the 3 scratches, before deposition.

Fig. 68 is a superposition of the 2 XMCD images with 90° rotation between them. It shows the 90° and 180° domain walls. As we were not able to determine the orientation of the BTO ferroelectric domains under the Fe wedge, it is not possible to determine if the magnetization of Fe is parallel or perpendicular to the electrical polarization of BTO. Anyway, the fact that we get this imprint after annealing (and so after changing the ferroelectric domains) suggests it would be possible to change the ferromagnetic domains when switching the ferroelectric domains, with potential use to the development of devices based on the magnetoelectric coupling.

It was not possible to know exactly the thickness of Fe for those images, but knowing the position of this region, with the fact that the sample is a wedge of Fe with thickness from 0 to 5 nm, we can estimate the thickness of Fe to be around 1 nm, thus similar to the thickness of the film measured *in-situ* in Berlin.

4.3 Third experiment: *ex-situ* measurements in Berlin

Another BTO substrate was used to deposit an Fe wedge by our collaborators in Jülich. This time it was a BTO (001) with area $5.5mm^2$, and the wedge ranged from

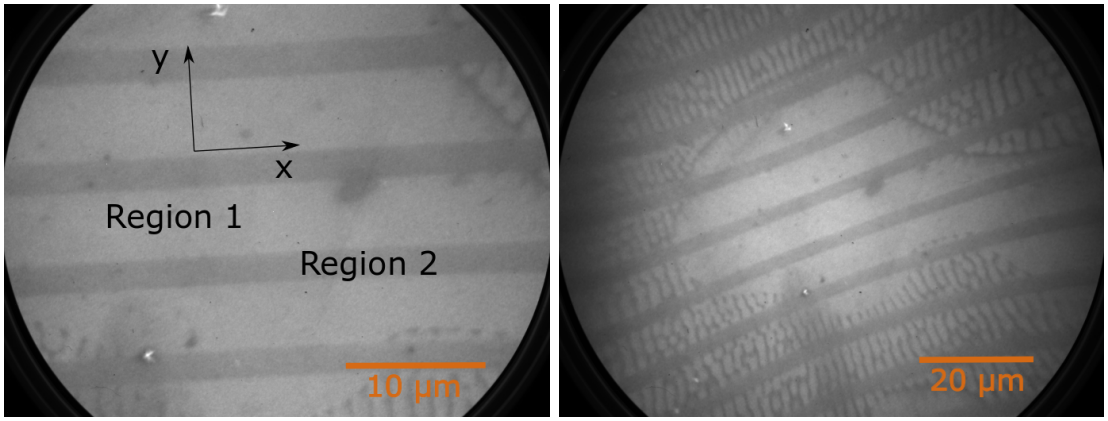

Figure 70 – UV PEEM image with $40\mu m$ (left) and $100\mu m$ FOV. The image with greater FOV is distorted at their outer region.

0 to 3.7 nm, with a deposition temperature of 100 °C for better crystallinity of the Fe layer [86]. An MgO capping layer of 0.8 nm was deposited to avoid oxidation. Before deposition, the BTO sample was annealed at 650 °C for 120 minutes in a MBE chamber and then cooled down to room temperature. We made 3 scratches before deposition, as shown in Fig. 69, which have their direction perpendicular to the gradient of the Fe edge. Doing these scratches before deposition also permits to have a/c-type ferroelectrics domains formation in the proximity of the scratch after annealing. After Fe deposition, the first scratch corresponds to around 1.2 nm of Fe, the second to 2 nm and the third to 3 nm.

4.3.1 Region around the first scratch, with 1.2 nm of Fe

4.3.1.1 Images with mercury lamp

Mercury lamps provide photons in the UV region, of around 5 eV. As described in 2.6.1, with such UV beam we can differentiate between in-plane and out-of-plane ferroelectric domains by their difference in work function, but in what follows we use this kind of illumination to obtain the topographic information only.

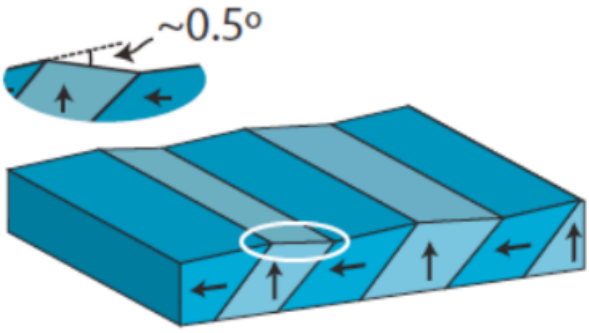

Figure 71 – Sketch of in-plane a and out-of-plane c ferroelectric domains configuration. Notice that to minimize the elastic energy, there is 0.5° deviation on the c domains relative to the a domains.

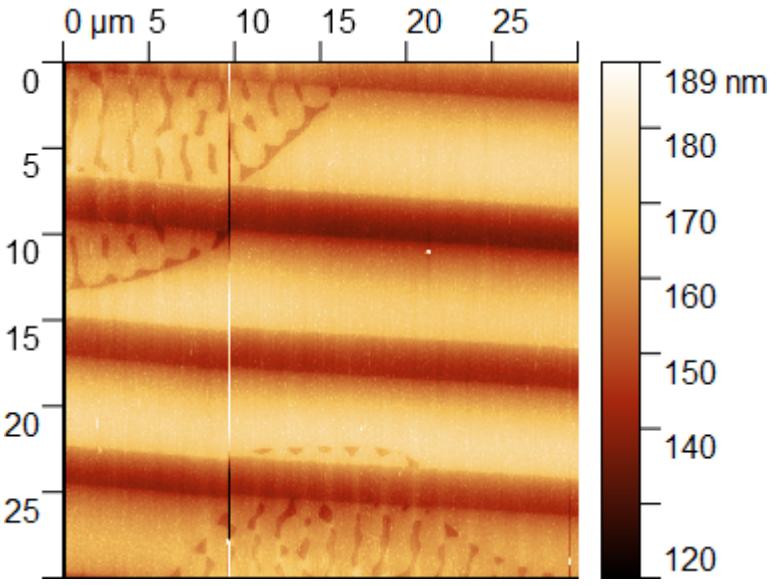

Figure 72 – AFM image of the same region than Fig. 70

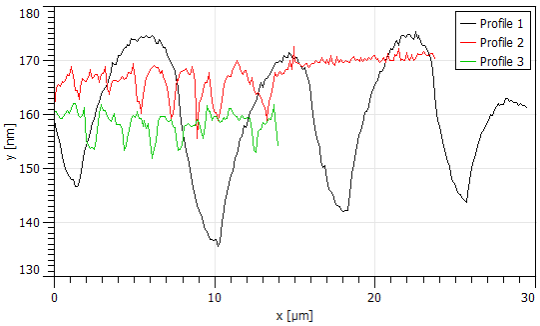

Figure 73 – Plot of the topography of the AFM image of Fig. 72, of a/c domains (black line) and of worm-like channels (red and green lines)

UV lamp PEEM images of the sample (Fig. 70 of 40μm FOV and 100μm, this last FOV giving some distortions) showed typical topography of a/c ferroelectric domains, which are a succession of out-of-plane c and in-plane a domains, as illustrated in Fig. 71. Brighter bands, which we will refer as region 1, are separated by dark, smaller bands (regions 2). The bands direction do indeed corresponds to the direction of one BTO axis. We will name x and y two crystalline axis at the surface of the BTO single crystal, as shown in Fig. 70. The region 1 bands are also characterized by the presence of black worm-like channels, this can be explained for out-of-plane domains by a preferential etching, performed before we get the sample, for negatively charged domains, thus the domain pattern of up and down out-of-plane domains are reproduced in the topography.

AFM measurements confirmed that those features were present in the topography of the sample, as it can be seen by comparing Fig. 70, the UV lamp PEEM image, to Fig. 72, an AFM image of the same region. Fig 73 shows a plot of the topography for a/c domains (black curve), and for the region 1 with worm-like channels. We can see that regions 2 are deep hollow areas, with a depth of around 15 nm, and the worm-like channels have a depth of around 5 nm, thus they are much deeper than the thickness of the Fe thin film.

Because of the Fe and MgO layer deposited on BTO, and because of the strong topographical contrast, it was not possible to visualize BTO ferroelectric domains with x-ray images at Ti edge. But it was possible to compare the UV lamp image (giving a topographical contrast) with the XMCD image at Fe edge showing the magnetic domains of Fe. This will be treated in the next section.

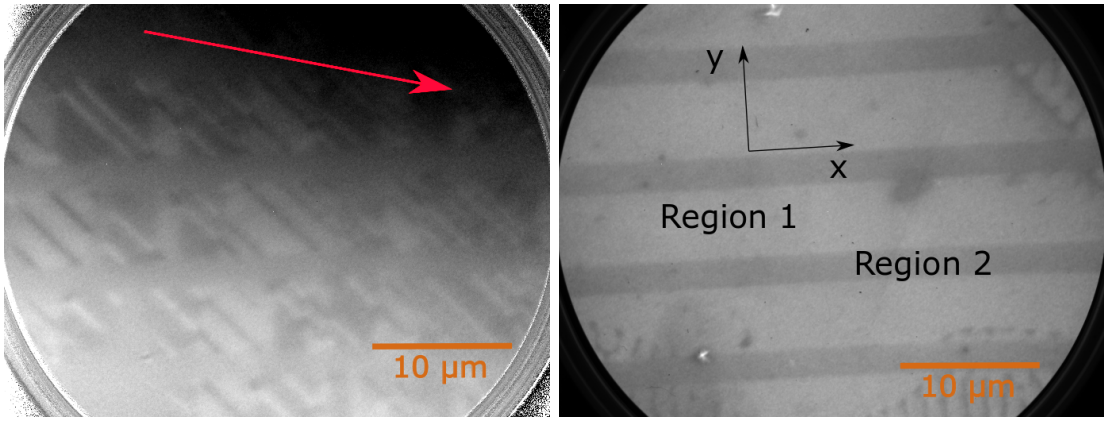

Figure 74 – XMCD PEEM image at the Fe L_3 edge, $40\mu m$ FOV. The red arrow represents the direction of the x-ray. At right we repeated the topography from fig. 70 for comparison.

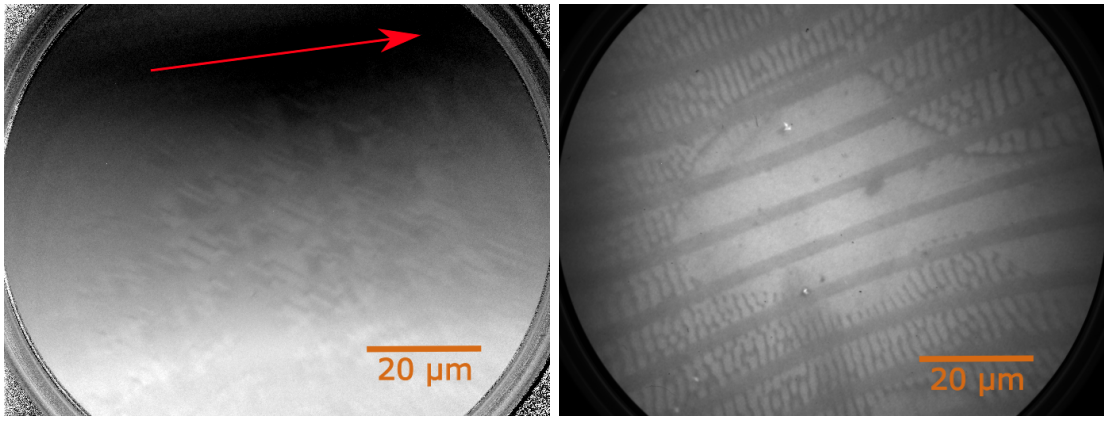

Figure 75 – XMCD PEEM image at the Fe L_3 edge, $100\mu m$ FOV. The red arrow represents the direction of the x-ray. At right we repeated the topography from fig. 70 for comparison.

4.3.1.2 XMCD-PEEM at Fe L_3 edges

Fe spectra gave a peak energy for the Fe edge of 706.8 eV, all XMCD images were done at this energy. The XMCD images corresponds to $\frac{I_- - I_+}{I_- + I_+}$, I_+ and I_- corresponding respectively to the images at the Fe edge with circular plus and minus polarization.

The magnetic contrast in this sample was not very strong, but the topographical contrast of the a/c domains is reproduced in the Fe magnetic contrast as can be seen in Fig. 74 (for $40\mu m$ FOV), and Fig. 75 (for $100\mu m$ FOV). In those figures we repeated the images obtained with UV lamp to make easier the comparison. Indeed, regions 1 show

magnetic contrast whereas regions 2 does not. For regions 1, stripes of ferromagnetic domains are visible at 45°from the BTO axis.

We saw in the previous experiment that those stripes ferromagnetic domains were imprinted by strain transfer from in-plane ferroelectric stripe domains of BTO, and are characterized by a magnetization at 45° from the direction of the stripes. Two types of domain walls are observed in the image. Domain walls parallel to the y axis correspond to 180° domain walls, with the magnetization of the domains along the y axis (because tail to tail or head to head domain wall would be rather improbable), and domain walls at 45°from BTO axis are 90°domain walls. Similar to the Campinas experiment, we can say that those 90°domain wall are due to Fe magnetic anisotropy imprinted by strain transfer by the BTO ferroelectric domains, and the 180°domain walls are present to minimize the magnetostatic energy, or to follow the underlying 180°ferroelectric domains withing the same stripe. At this moment we can not determine the exact nature of the 180°walls.

From this information and knowing the direction of projection of the X-ray beam we can deduce the direction of the magnetic vector of Fe domains, as shown in Fig. 76. The magnetic contrast of the domains should correspond to the projection of the magnetization into the direction of the X-ray beam. However, it is not what is observed, but this unexpected contrast can be explained by stronger dependence on focus for the thinner domains, as it is discussed below.

On the 100 μm FOV image, we also see that stripes appear in region 1 only where no worm-like channels are present. This is consistent with the fact that a rough topography could prevent a good Fe deposition, and thus no magnetism is seen in those regions either.

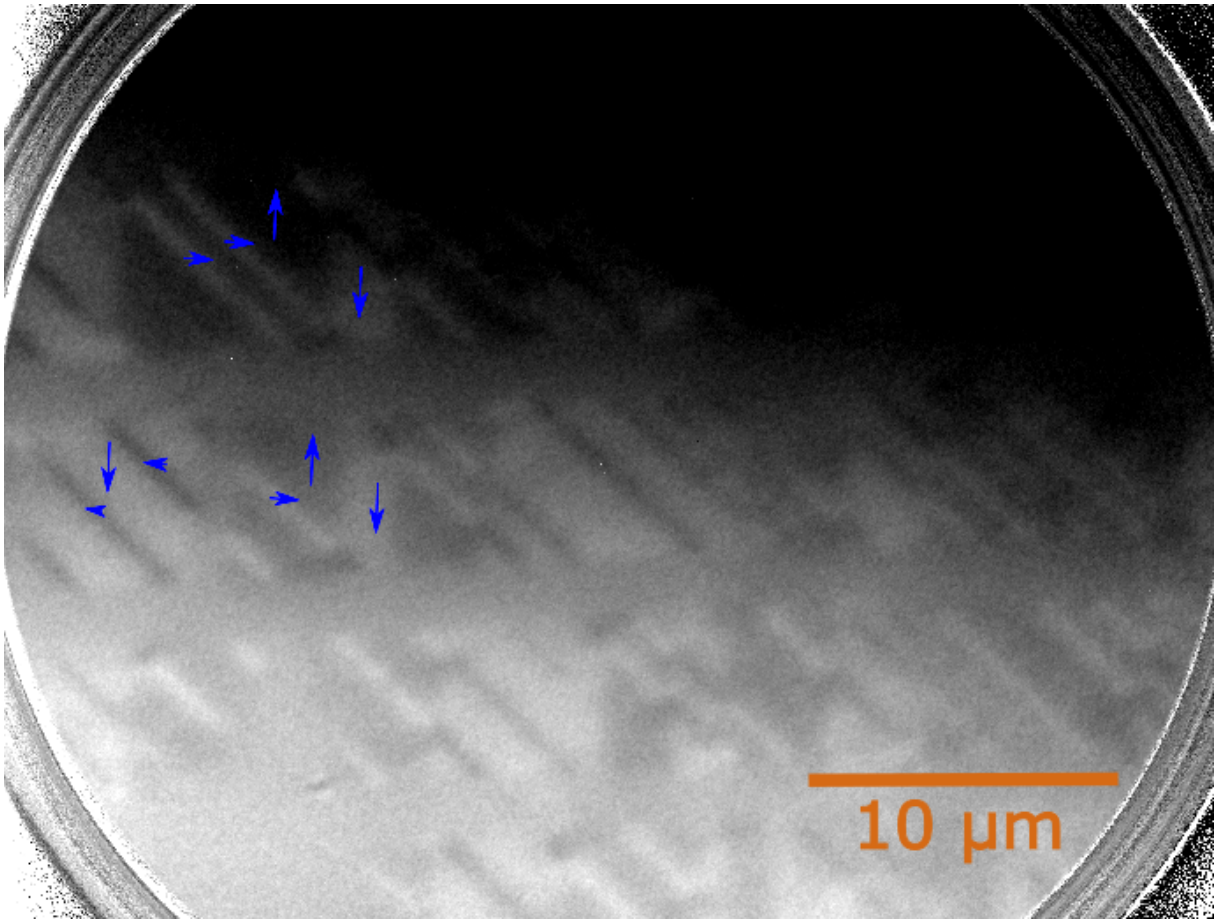

Figure 76 – XMCD PEEM image at the Fe L_3 edge, $40\mu m$ FOV. The blue arrows represent the direction of the magnetization.

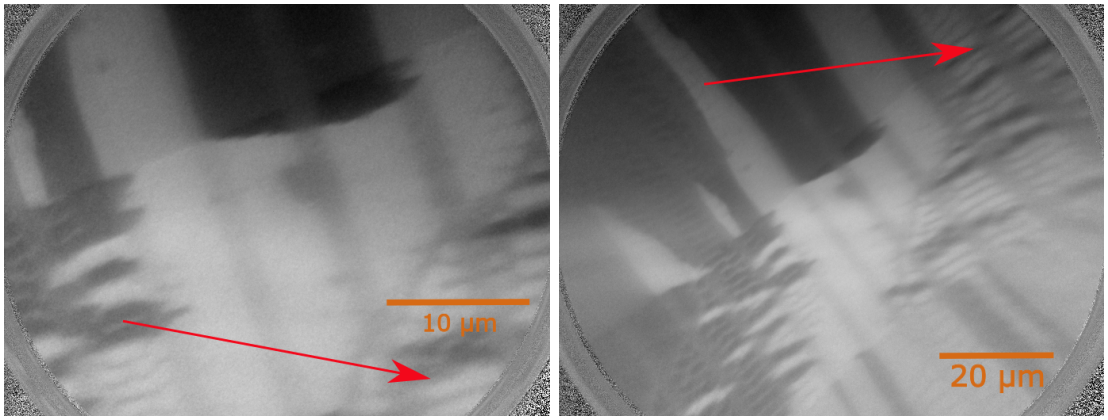

Figure 77 – XMCD PEEM image at the Fe L_3 edge with 40 and $100\mu m$ FOV. The red arrow represents the direction of the x-ray

We took XMCD images at other angles. After turning the sample of 45°, we saw that the ferromagnetic domain pattern radically changed. Fig. 77 is the XMCD image with 40 and 100 μm FOV. Besides the changes in the domain pattern, the magnetic contrast increased by at least a factor 3 (see the discussion on contrast below). After going back to almost the same first angle, we checked that domain pattern and magnetic contrast were different from the initial state. Fig. 78 show the new pattern.

In the next section we analyze the new pattern and discuss possible reasons for the change.

4.3.1.3 Description of the new domain pattern

The new domain pattern is now consisted of nearly homogeneous magnetization for most of regions 1. But in Fig. 78, in the left panel with 40 μm FOV, we can split the image in two: one with horizontal bright and dark stripes separated by gray ones, and the right part of the image is a grey background with some thin magnetic domains indicated by the inclined brigh and dark regions. Looking carefully to the grey background one can still notice that the large horizontal stripes are still present. The same figure at right, with 100 μm FOV, shows that this gray region with the thin stripes is actually a vertical band with $\approx$30 μm laterally. We do not see the thin stripes in the gray region in the 100 μm FOV image because the focus is not good enough. Also the gray band appear a bit curved because of the distortion present when using the 100 μm FOV, but the image with the 40 μm FOV clearly shows that the interface between the two regions is a straight line along the y axis.

The magnetic contrast increased in all the measured region but not in the worm-like channels, which continue to present no contrast, so we can clearly distinguish them

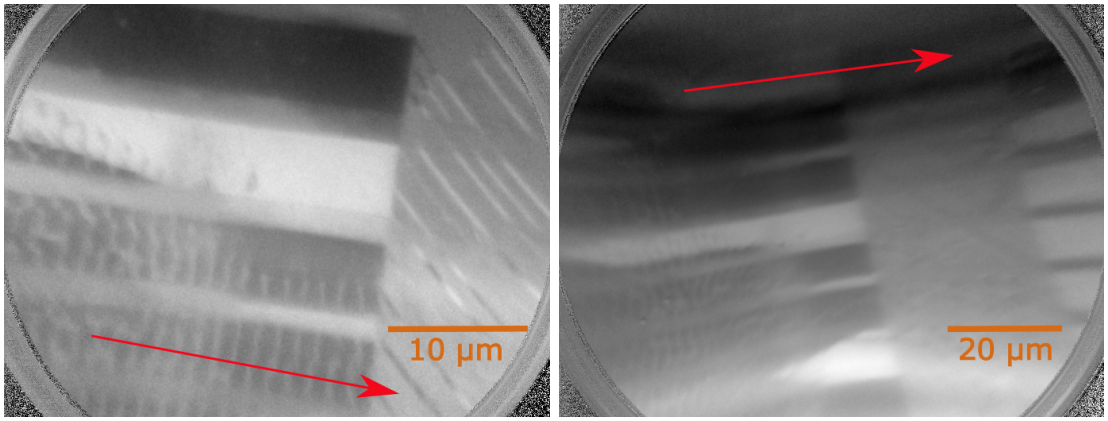

Figure 78 – XMCD PEEM image at the Fe L_3 edge, 40 μm and 100 μm FOV after return to the original azimuthal angle. The domain pattern did not reproduced those seem at the left side of figs. 74 and 75.

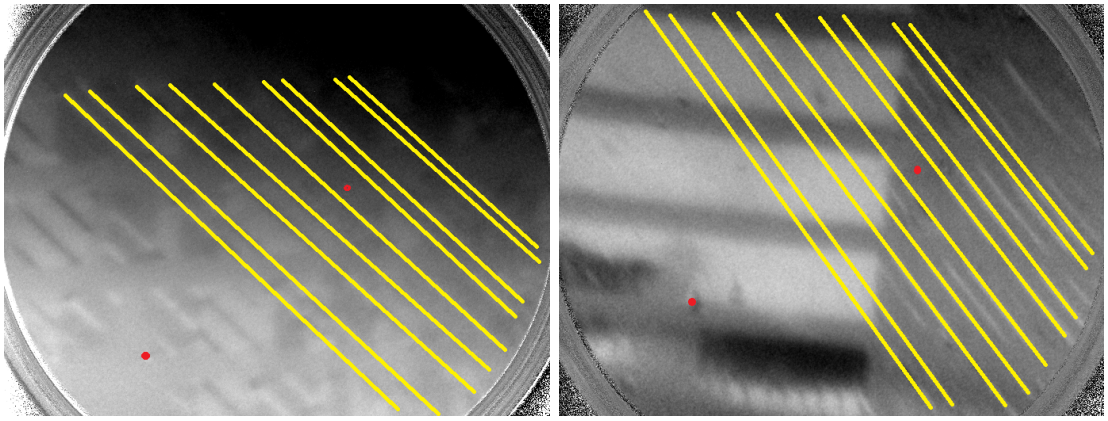

Figure 79 – Position of the stripes the (left) and after (right) turning the sample by 45°.

and thus the magnetic contrast reproduce the topographical contrast. Most of regions 2 continue to present no contrast neither, but some of regions 2 at the edge of the band with stripe contrast present now some magnetic contrast, as it can be seen in Fig. 78 although still lower than the contrast of other domains.

In the Fig. 79 at left, we repeated the initial 40 μm FOV image shown in fig. 74 and include some yellow guide lines to show the position of some of the domains. At the right side of fig. 79, we show the same region after the changing in contrast with the yellow marks at the same place. We notice that the position of the stripes is the same. Also, the direction of the magnetization did not change for those stripes, the small stripes still have a magnetization direction along the x axis and the larger stripes along y. Thus,

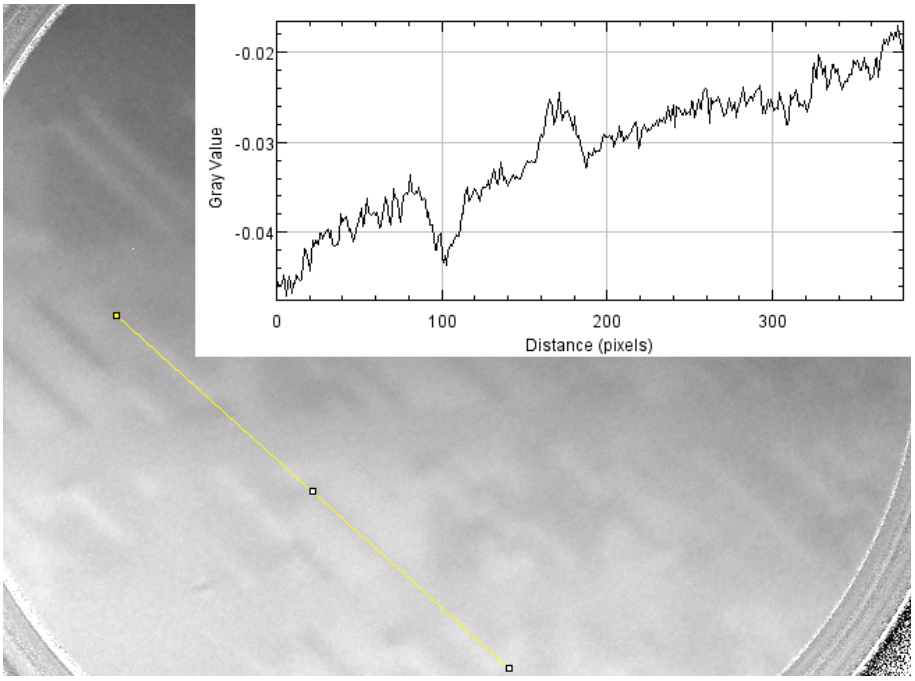

Figure 80 – XMCD PEEM image at the Fe L_3 edge, $40\mu m$ FOV. A plot of the magnetic contrast amplitude along the yellow line (for small stripes domains) is showed.

it seems that the gray area that we see after the change of contrast corresponds to the initial condition, except that the magnetic contrast is more intense. The change happened in the region of the large horizontal stripes.

4.3.1.4 Discussion on the magnetic contrast of the small stripes

The contrast should be proportional to the projection of the magnetic moment direction along the direction of the X-ray beam. With the first domain pattern presented in Fig. 74 and Fig. 75, as the magnetization direction of the small stripes is along the y axis, and the one of the bigger stripes is along the x axis, the ratio of magnetic contrast for the two types of stripes should be $\frac{cos(15)}{cos(75)} = 3.7$, as 15° is the angle between the X-ray direction and the x axis and 75° the angle between the X-ray direction and the y axis. But in Fig. 80 and Fig. 81 which represent the plot of the magnetic contrast along the yellow line in the image, we see that the contrast of the smaller stripes (Fig. 80, the contrast amplitude between bright and dark small stripes is around 0.011) is just a bit higher than

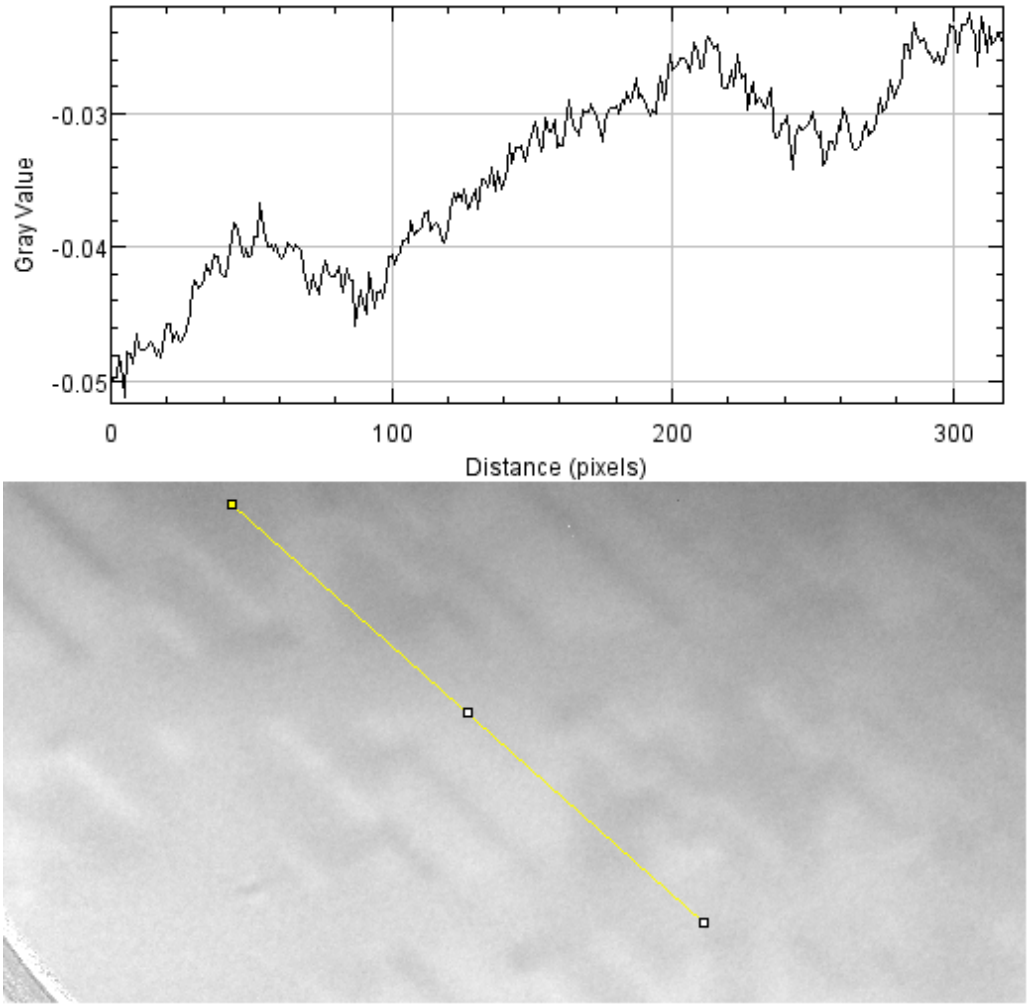

Figure 81 – XMCD PEEM image at the Fe L_3 edge, $40\mu m$ FOV. A plot of the magnetic contrast amplitude along the yellow line (for small stripes domains) is showed.

the contrast of the bigger stripes (Fig. 81, the contrast amplitude is around 0.008).

In Fig. 78, with the new domain pattern and the X-ray direction almost parallel to the x direction, the thinner stripes, which have their magnetization along the x axis appear white or black, as well as the regions 1 where the stripe domain pattern disappeared, becoming large, continuous domains. Due to the strong contrast present in those regions 1 we can suppose that for those domains the magnetization is also along the x direction. The contrast of the large horizontal domains in regions 1 is around three times the one of the small stripes in the gray area (see Fig. 82). This is consistent with the factor 3.7 that was expected for the small stripe domains in Fig. 74.

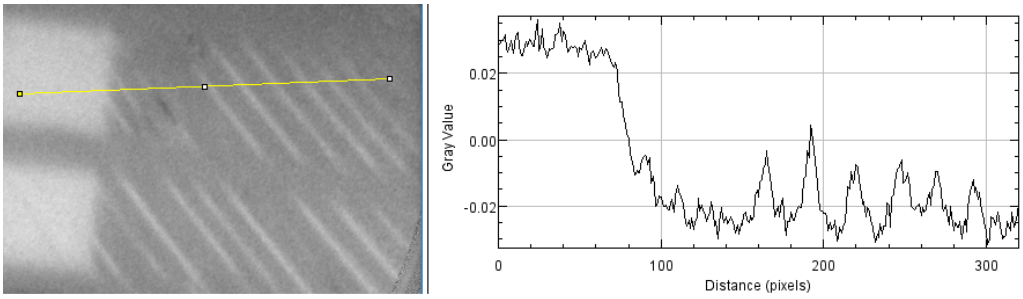

Figure 82 – XMCD PEEM image at the Fe L_3 edge, $40\mu m$ FOV. A plot of the magnetic contrast amplitude along the yellow line is showed.

4.3.1.5 Origin of the modification in the magnetic domain pattern

We believe that the modification of the ferromagnetic domain pattern after rotating the sample can be explained by a change of the BTO ferroelectric domain pattern, which changed from one kind of a/c configuration into another a/c configuration, except for the gray band in the center that kept its initial state.

A possible reason for the modification is an electrical discharge during the rotation. During PEEM measurements, the sample is maintained at an electric potential of -15000 V relative to the PEEM objective. It is not uncommon to happen discharges between sample and objective. In particular, during the change of azimuth, the internal mechanical motions make the internal pressure increase and this can help the occurrence of discharges. If this happened, then the energy would be delivered at the region being imaged by the objective which is exactly the region under study. This could have the effect of a localized annealing, reorganizing the ferroelectric domains. We did not notice any discharge during the rotation, but we can not rule out its possibility. These discharges are quite fast and could happen without our notice. There were occasions when this happened in bare BTO substrate, and the images were completely different before and after the discharge.

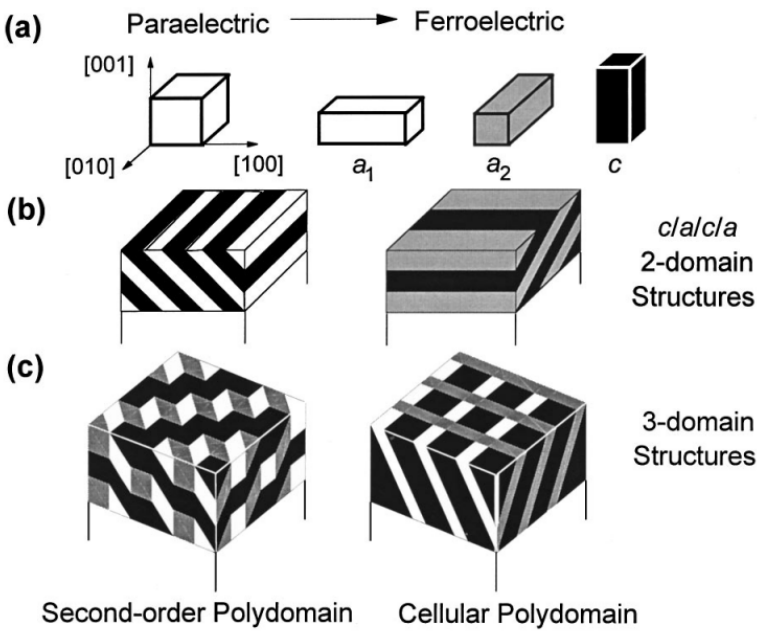

Figure 83 – Representation of the possible polydomains configurations in tetragonal ferroelectric materials from reference [62]. In (a) it is defined the direction of the three types of domains, a_1, a_2 and c. (b) shows the configuration having two kind of domains invoved. (c) shows possible configurations involving all the three kinds of ferroelectric domains.

The configuration of the magnetic domain that we probe by XMCD-PEEM are still related with the underlying ferroelectric domains of the BTO substrate. We were not able to image directly the ferroelectric domains, but we can deduce that they are quite intricate. Indeed, it is know that in tetragonal ferroelectric material like BTO, the ferroelectric domain structure can be the association of all the three possible directions, a_1, a_2 and c, as show in fig. 83 from reference [62].

The new ferroelectric BTO domains corresponding to fig. 78 are modeled in Fig. 84. In this configuration, domain walls separating in plane domains are not at 45° from the electric polarization but along the y axis, thus generating strain and charges at the wall, but those domain walls are only at the interface with the band of stripe domains.

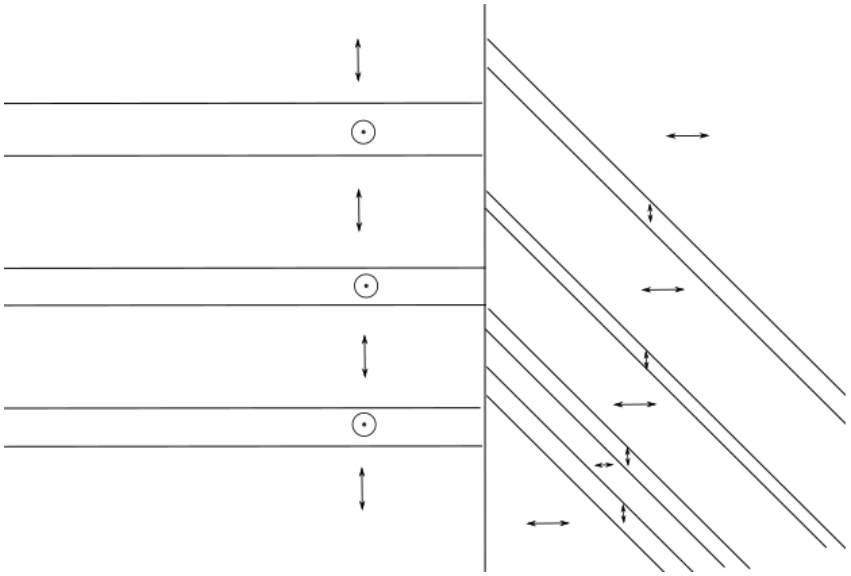

Figure 84 – New BTO ferroelectric domain pattern corresponding to the ferromagnetic pattern of Fig. 78

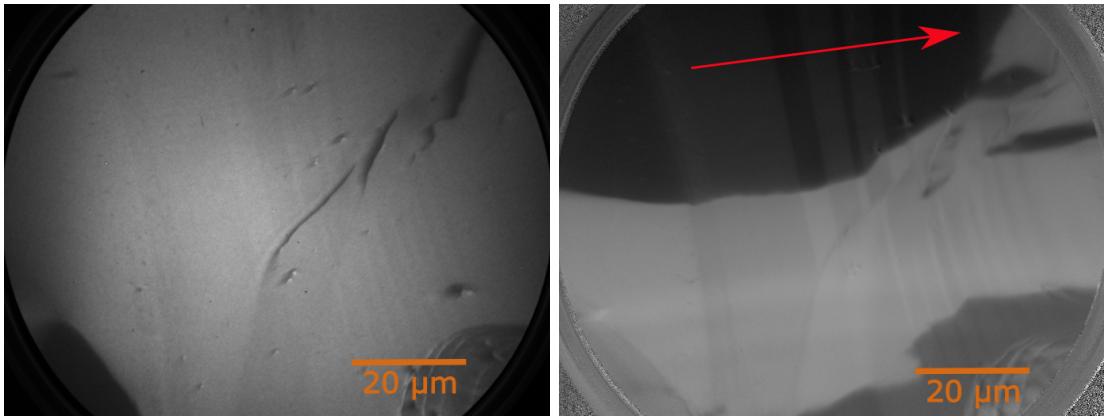

Figure 85 – Images of the region with Fe thickness of around 2 nm. At left the topography using UV lamp and at right the XMCD-PEEM. Both images of the same region with $100\mu m$ FOV.

Comparing this figure to the direction of the ferromagnetic domains, we can say that the magnetization of Fe is perpendicular to the ferroelectric polarization of BTO for BTO in-plane domains. We could not determine the direction of magnetization for Fe above BTO out of plane domains as it corresponded to regions 2 domains, which are above deep hollow areas and did not permit a good growth of Fe.

4.3.2 Region around the second scratch, with 2 nm of Fe

Fig. 85 shows the topography and XMCD just above the scratch in the 2 nm thick Fe region. The scratch is at the bottom of the images. As we saw before, a/c BTO domains appears near the scratch after annealing of the BTO (before deposition of Fe), generating a stripe contrast in the topography. Here thin stripes appear along the y axis with a very faint contrast. The a/c domains appearing near the scratch are much smaller than the a/c domains already present initially, so the topographical contrast associated is much weaker. Nevertheless, we can see a correspondence between this topographical contrast and the contrast of the magnetic Fe domains, but this magnetic contrast is rather weak compared to the magnetic contrast of the area around the 1 nm of Fe thickness. This suggest that the strain transfer from the BTO substrate is present only for the first layers of Fe, or that the induced magnetoelastic anisotropy is not sufficient to overcome the other contributions of anisotropy. This is an interesting result, showing that one really needs an Fe thickness of 1.5 nm at most to observe a complete magnetoelectric coupling.

As we did not observe the full coupling between ferroelectric and ferromagnetic domains in this region, we did not investigate it further.

4.4 Conclusions on the magnetoelectric coupling in Fe/BaTiO$_3$ heterostructures

We saw that an imprint of the BTO ferroelectric domains on the Fe magnetic domains was possible for a very thin Fe layer, with thicknesses of 1.5 nm or less. This is an important observation that could open possibilities to the use of this kind of heterostructures in devices. The magnetoelectric coupling seems to be by strain transfer from

the tetragonal BTO distortion to the Fe film. The ferroelectric domain configuration is extremely dependent on the annealing history of the sample and must be better studied in other experiments to gain a better control on the determination of initial ferroelectric domain configuration.

We observed 90° and 180° magnetic domains walls. Whereas the former were directly associated with the ferroelectric imprint, the 180° could simply be due to a reduction in the magnetostatic energy. Nevertheless, we did not rule out that also these walls are determined by the underlying ferroelectric domains. Further studies are needed to clarify this point.

When we grew the Fe layer *ex-situ* the magnetic contrast was strong as expected for Fe, whereas *in-situ* we have a weaker contrast. The weak contrast for the *in-situ* experiment could be due to the growth conditions, and the fact that the film was deposited at room temperature and was not post-annelead. Another point is that the analysis chamber, where is done the PEEM images, have usually a good pressure (low 10^{-8} Pa range), as well as the preparation chamber, but to transfer to the preparation chamber the sample has to go through the transfer section which has usually an worse pressure (low 10^{-6} Pa range). The exposition of the clean BTO substrate to such pressure might be sufficient to degrade the BTO surface and prevent a good coupling.

Chapter 5

Conclusions and perspectives

In this work we have grown and investigated the properties of multiferroics systems. We obtained little success in the growth of $YMnO_3$ and $BaTiO_3$ thin films. But these were very first growth attempts in our group and after that other members have continued this research and arrived in good samples, mostly employing pulsed laser deposition on $SrTiO_3$ substrates. Nevertheless, the approach of growing by sputtering on Si substrates is still valid, once that for applications this has an enormous potential. Sputtering is a scalable growth technique, already in use in several industrial segments. And if one succeeds to grow these films on Si, this is the first step to integrate potential devices based on such materials directly in the present microelectronic technology.

In the case of $BiFeO_3$ and $SrRuO_3$, we managed to find the good growth conditions to obtain epitaxial quality films on $SrTiO_3$ by sputtering. For $BiFeO_3$, we narrowed down the phase space of deposition parameters and found that outside these optimized conditions one obtains spurious Bi and Fe oxides, that could lead to ferromagnetic behavior. Having the good recipe to grow $BiFeO_3$ is the first step to use it as component in more complex heterostructures that would allow to explore its intrinsic multiferroicity and magnetoelectric coupling to develop technological applications. We stress that to find

the good deposition conditions we explore a new sputtering route, namely deposition at high pure oxygen pressure and with high substrate-target distance.

The most important results of this PhD thesis are those related with the magnetoelectric effect in a Fe/$BaTiO_3$ (Fe/BTO) heterostructures. These samples are artificial multiferroic systems, and the magnetoelectric coupling between the Fe magnetic layer and the BTO ferroelectric substrate is done by strain transfer from the BTO ferroelectric domains to the Fe layer, creating preferential magnetization directions.

We were not the first group to observe and image such system, but the originality of this work arises from the use of PEEM, which allows to have a detailed description of both ferroelectric and ferromagnetic domains, including element specific information. We observed that for in-plane ferroelectric domains of $BaTiO_3$, the coupling with the Fe layer above resulted in a preferential magnetization direction perpendicular to the electric polarization. Also, we determined a maximum value of around 1.5 nm for the thickness of the Fe layer in order to assure a full coupling between the ferroelectric and ferromagnetic order. From our results we can observe also the rich domain configuration of the ferroelectric $BaTiO_3$ substrates. Finally, we showed the important dependence on the quality of the Fe film on the magnetoelectric effect, given that after a recrystallization under a soft annealing the sharpness of the magnetoelectric coupling was greatly enhanced.

This work answered a few questions about the systems studied, but also leaves some other to be still investigated. In the continuation of this work we could say that one of the most important tasks is to determine with precision the magnetic domain orientation relative to the ferroelectric polarization. For that, many more PEEM images will be necessary at several azimuthal angles. Also following with imaging the magnetoelectric

coupling around the BTO tetragonal transition could give some insights on its properties. One of the most interesting consequences of this work would be extending it to study Fe on BTO thin films, instead of BTO monocrystals as done here. Thin film heterostructures have a larger appealing for integration in devices. One important open question is the eventual coupling of the Fe magnetization with the direction of the ferroelectric domains. As linear dichroism is of no help here, other multi techniques approaches will have to be used to clarify this point. One possibility is a systematic use of piezoforce response microscopy (PFM) to investigate the BTO ferroelectric domains.

Finally, here we concentrate on the Fe/BTO system, but there are several other possibilities of materials association that could be employed to investigate and eventually develop devices based on artificial magnetoelectric structures.

Bibliography

[1] P Muralt. Ferroelectric thin films for micro-sensors and actuators: a review. *Journal of Micromechanics and Microengineering*, 10(2):136, 2000. URL: http://stacks.iop.org/0960-1317/10/i=2/a=307. Cited on page 14.

[2] M. Dawber, K. M. Rabe, and J. F. Scott. Physics of thin-film ferroelectric oxides. *Rev. Mod. Phys.*, 77:1083–1130, Oct 2005. URL: http://link.aps.org/doi/10.1103/RevModPhys.77.1083, doi:10.1103/RevModPhys.77.1083. Cited 2 times on page(s) 14 and 15.

[3] J.F. Scott. *Ferroelectric Memories*. Advanced microelectronics. Springer, 2000. URL: http://books.google.com.br/books?id=9FT06UFHWZwC. Cited on page 15.

[4] Rainer Waser, editor. *Nanoelectronics and Information Technology: Advanced Electronic Materials and Novel Devices*. John Wiley & Sons, Inc., New York, NY, USA, 2003. Cited on page 16.

[5] Jason R. Hattrick-Simpers, Liyang Dai, Manfred Wuttig, Ichiro Takeuchi, and Eckhard Quandt. Demonstration of magnetoelectric scanning probe microscopy. *Review of Scientific Instruments*, 78(10):106103, October 2007. doi:10.1063/1.2777197. Cited on page 16.

[6] Rudolf Pfeiffer" "Michael A. Gottlieb. The magnetism of matter. URL: http://www.feynmanlectures.caltech.edu/II_34.html. Cited on page 17.

[7] Erik Koch. *Exchange Mechanisms*. Lecture Notes of the Autumn School Correlated Electrons 2012. Forschungszentrum Jülich GmbH, 2012. URL: http://www.cond-mat.de/events/correl12/manuscripts/koch.pdf. Cited on page 18.

[8] Daniel Marius Gottlob. *Spin-reorientation transition in epitaxial NixPd1-x fims on Cu(001): a microscopic analysis*. PhD thesis, 2014. Cited 2 times on page(s) 19 and 81.

[9] M. Cyrot Étienne du Trémolet de Lacheisserie. *Magnétisme. Tome 1, Fondements*. Collection Grenoble sciences. EDP Sciences, 2000. Cited on page 20.

[10] Hatice Doganay. *Magnetoelectric Interactions in Multiferroic Thin-film Heterosystems and Nanostructures*. PhD thesis, not published yet. Cited 8 times on page(s) 20, 37, 87, 88, 89, 90, 118, and 125.

[11] L.W. Martin, Y.-H. Chu, and R. Ramesh. Advances in the growth and characterization of magnetic, ferroelectric, and multiferroic oxide thin films. *Materials Science and Engineering: R: Reports*, 68, 2010. URL: http://dx.doi.org/10.1016/j.mser.2010.03.001, doi:10.1016/j.mser.2010.03.001. Cited on page 21.

[12] K.M. Rabe, C.H. Ahn, and J.M. Triscone. *Physics of Ferroelectrics: A Modern Perspective*. Topics in Applied Physics. Springer, 2007. URL: http://books.google.com.br/books?id=-QhVI8JTvwwC. Cited 6 times on page(s) 22, 24, 25, 26, 30, and 32.

[13] M.E. Lines and A.M. Glass. *Principles and Applications of Ferroelectrics and Related Materials*. International series of monographs on physics. Clarendon Press, 1979.

URL: http://books.google.com.br/books?id=Mv5LPgAACAAJ. Cited 2 times on page(s) 23 and 30.

[14] Wikipedia. Lead zirconate titanate. URL: http://en.wikipedia.org/wiki/Lead_zirconate_titanate. Cited on page 23.

[15] Daniel Khomskii. Classifying multiferroics: Mechanisms and effects. *Physics*, 2:20, Mar 2009. URL: http://link.aps.org/doi/10.1103/Physics.2.20, doi:10.1103/Physics.2.20. Cited 2 times on page(s) 24 and 33.

[16] G. Catalan, J. Seidel, R. Ramesh, and J. F. Scott. Domain wall nanoelectronics. *Rev. Mod. Phys.*, 84:119–156, Feb 2012. URL: http://link.aps.org/doi/10.1103/RevModPhys.84.119, doi:10.1103/RevModPhys.84.119. Cited 4 times on page(s) 25, 26, 27, and 28.

[17] Julien Rault. *Chemical and electronic structure of the metal : ferroelectric interface as a function of ferroelectric polarization*. PhD thesis, 2013. Thèse de doctorat dirigée par Barrett, Nicholas Physique Paris 6 2013. URL: http://www.theses.fr/2013PA066797. Cited on page 26.

[18] G. Burns and A.M. Glazer. *Space groups for solid state scientists*. Academic Press, 1990. URL: http://books.google.com.br/books?id=a7_vAAAAMAAJ. Cited 2 times on page(s) 27 and 30.

[19] M. Y. Gureev, A. K. Tagantsev, and N. Setter. Head-to-head and tail-to-tail 180° domain walls in an isolated ferroelectric. *Phys. Rev. B*, 83:184104, May 2011. URL: http://link.aps.org/doi/10.1103/PhysRevB.83.184104, doi:10.1103/PhysRevB.83.184104. Cited on page 27.

[20] Hans Schmid. Some symmetry aspects of ferroics and single phase multiferroics *. *Journal of Physics: Condensed Matter*, 20(43):434201, 2008. URL: http://stacks.iop.org/0953-8984/20/i=43/a=434201. Cited 3 times on page(s) 29, 31, and 32.

[21] W. Eerenstein, N. D. Mathur, and J. F. Scott. Multiferroic and magnetoelectric materials. *Nature*, 2006. URL: http://dx.doi.org/10.1038/nature05023, doi:10.1038/nature05023. Cited on page 30.

[22] D. B. Litvin. Tensor distinction of domains in ferroic crystals. *The European Physical Journal B - Condensed Matter and Complex Systems*, 71(3):315–320, 2009. URL: http://EconPapers.repec.org/RePEc:spr:eurphb:v:71:y:2009:i:3:p:315-320. Cited on page 30.

[23] Kêitsiro Aizu. Possible species of ferromagnetic, ferroelectric, and ferroelastic crystals. *Phys. Rev. B*, 2:754–772, Aug 1970. URL: http://link.aps.org/doi/10.1103/PhysRevB.2.754, doi:10.1103/PhysRevB.2.754. Cited 3 times on page(s) 30, 31, and 32.

[24] D. I. Khomskii. Multiferroics: Different ways to combine magnetism and ferroelectricity. *J. Magn. Magn. Mater.*, 306:1–8, 2006. Cited on page 33.

[25] Shuai Dong, Jun-Ming Liu, Sang-Wook Cheong, and Zhifeng Ren. Multiferroic materials and magnetoelectric physics: symmetry, entanglement, excitation, and topology. *Advances in Physics*, 64(5-6):519–626, 2015. URL: http://dx.doi.org/10.1080/00018732.2015.1114338, arXiv:http://dx.doi.org/10.1080/00018732.2015.1114338, doi:10.1080/00018732.2015.1114338. Cited on page 33.

[26] Chun-Gang Duan, S. S. Jaswal, and E. Y. Tsymbal. Predicted magnetoelectric effect in Fe/batio$_3$ multilayers: Ferroelectric control of magnetism. *Phys. Rev. Lett.*,

97:047201, Jul 2006. URL: https://link.aps.org/doi/10.1103/PhysRevLett.97.047201, doi:10.1103/PhysRevLett.97.047201. Cited 2 times on page(s) 34 and 40.

[27] Nien Ti Tsou. *Compatible domain structures in ferroelectric single crystals.* PhD thesis, 2011. Cited on page 36.

[28] Prashant R. Potnis, Nien-Ti Tsou, and John E. Huber. A review of domain modelling and domain imaging techniques in ferroelectric crystals. *Materials*, 4(2):417–447, 2011. URL: http://www.mdpi.com/1996-1944/4/2/417, doi:10.3390/ma4020417. Cited on page 36.

[29] Tuomas H. E. Lahtinen, Yasuhiro Shirahata, Lide Yao, Kévin J. A. Franke, Gorige Venkataiah, Tomoyasu Taniyama, and Sebastiaan van Dijken. Alternating domains with uniaxial and biaxial magnetic anisotropy in epitaxial fe films on batio3. *Applied Physics Letters*, 101(26):262405, 2012. URL: http://dx.doi.org/10.1063/1.4773482, arXiv:http://dx.doi.org/10.1063/1.4773482, doi:10.1063/1.4773482. Cited 3 times on page(s) 38, 39, and 40.

[30] Remya Kunjuveettil Govind. *Growth, magnetic properties and interface effects of Fe and Fe-oxide ultrathin films on BaTiO3(001) substrates.* PhD thesis, 2013. Cited 2 times on page(s) 38 and 39.

[31] Laura Bocher, Alexandre Gloter, Arnaud Crassous, Vincent Garcia, Katia March, Alberto Zobelli, Sergio Valencia, Shaïma Enouz-Vedrenne, Xavier Moya, Neil D Mathur, Neil D Marthur, Cyrile Deranlot, Stéphane Fusil, K Bouzehouane, Manuel Bibes, Agnes Barthelemy, C Colliex, and Odile Stéphan. Atomic and electronic struc-

ture of the batio3/fe interface in multiferroic tunnel junctions. 12:376–82, 12 2011. Cited on page 40.

[32] Inc. AJA INTERNATIONAL. What is sputtering? URL: http://www.ajaint.com/what-is-sputtering.html. Cited on page 43.

[33] Thiago José de Almeida Mori. *MATERIAIS E TÉCNICAS PARA NANOESTRUTURAS MAGNETOELÉTRICAS COMPÓSITAS*. PhD thesis, 2014. Cited 3 times on page(s) 43, 46, and 62.

[34] E Alfonso, J Olaya, and Cubillos. Thin film growth through sputtering technique and its applications. *Crystallization - Science and Technology*, 2012. URL: http://www.intechopen.com/books/crystallization-science-and-technology/thin-film-growth-through-sputtering-technique-and-its-applications, doi:10.5772/35844. Cited on page 44.

[35] R.J. Sanderson and K.C. Hewitt. Stoichiometry control of magnetron sputtered bi2sr2cayxcu2oy thin film, composition spread libraries: Substrate bias and gas density factors. *Physica C Superconductivity*, 425, 2005. URL: http://www.sciencedirect.com/science/article/pii/S0921453405004466, doi:http://dx.doi.org/10.1016/j.physc.2005.06.002. Cited 2 times on page(s) 45 and 49.

[36] P. KELLY and R. ARNELL. Magnetron sputtering: a review of recent developments and applications. *Vacuum*, 56(3):159–172, 2000. URL: http://www.ingentaconnect.com/content/els/0042207x/2000/00000056/00000003/art00189. Cited on page 45.

[37] Takafumi Kamo, Ken Nishida, Kensuke Akiyama, Joe Sakai, Takashi Katoda, and Hiroshi Funakubo. Rf magnetron sputtering growth of epitaxial srruo 3 films with high conductivity. *Japanese Journal of Applied Physics*, 46(10S):6987, 2007. URL: http://stacks.iop.org/1347-4065/46/i=10S/a=6987. Cited on page 47.

[38] Sanghyun Park, Young-Jin Son, Sung-Sil Cho, Sung-Yeon Hwang, Ae-Kyoung Lee, Hae-Chan Park, Suk-Kyoung Hong, Sung Joo Hong, Min-Ho Kang, Sung Kyu Lim, Wan-Gyu Lee, Ji-Hye Choi, and Soon-Yong Kweon. Characterization of polycrystalline srruo3 thin films deposited by dc magnetron sputtering method. *Journal of the Korean Physical Society*, 51(2):710–714, 2006. Cited 2 times on page(s) 47 and 48.

[39] Ying Wang, Weijin Chen, Biao Wang, and Yue Zheng. Ultrathin ferroelectric films: Growth, characterization, physics and applications. *Materials*, 7(9):6377, 2014. URL: http://www.mdpi.com/1996-1944/7/9/6377, doi:10.3390/ma7096377. Cited on page 47.

[40] Kenji Takahashi, Takahiro Oikawa, Keisuke Saito, Hironori Fujisawa, Masaru Shimizu, and Hiroshi Funakubo. Thermal stability of srruo 3 bottom electrode and electric property of pb(zr, ti)o 3 thin film deposited on srruo 3. *Japanese Journal of Applied Physics*, 41(11S):6873, 2002. URL: http://stacks.iop.org/1347-4065/41/i=11S/a=6873. Cited 2 times on page(s) 47 and 113.

[41] Takeshi Tai, Masamichi Nishide, Masashi Matsuoka, Takafumi Kamo, Hiroshi Funakubo, Takashi Katoda, Hiromi Shima, Ken Nishida, and Takashi Yamamoto. Investigation of sputtering damage in srruo 3 films prepared by sputtering with raman and x-ray photoemission spectroscopies. *Japanese Journal of Applied Physics*,

51(9S1):09LA19, 2012. URL: http://stacks.iop.org/1347-4065/51/i=9S1/a=09LA19. Cited 2 times on page(s) 47 and 109.

[42] C B Eom, R J Cava, R M Fleming, Phillips, Julia M, R B Vandover, J H Marshall, J W P Hsu, J J Krajewski, and W F Peck. Single-crystal epitaxial thin films of the isotropic metallic oxides sr1-xcaxruo3. *Science*, 258(5089):1766–1769, 1992. doi:10.1126/science.258.5089.1766. Cited on page 47.

[43] M. K. R. Khan, M. Ito, and M. Ishida. Epitaxial growth of srruo3 thin films by rf sputtering and study of surface morphology. *Frontiers of Materials Science in China*, 4(4):387–393, 2010. URL: http://dx.doi.org/10.1007/s11706-010-0098-9, doi:10.1007/s11706-010-0098-9. Cited on page 48.

[44] Y. K. Wang, T. Y. Tseng, and Pang Lin. Enhanced ferroelectric properties of pb(zr0.53ti0.47)o3 thin films on srruo3/ru/sio2/si substrates. *Applied Physics Letters*, 80(20):3790–3792, 2002. URL: http://scitation.aip.org/content/aip/journal/apl/80/20/10.1063/1.1480099, doi:http://dx.doi.org/10.1063/1.1480099. Cited on page 48.

[45] J. Li, J. Wang, M. Wuttig, R. Ramesh, N. Wang, B. Ruette, and et al. Pyatakov, A. P. Dramatically enhanced polarization in (001), (101) and (111) bifeo3 thin films due to epitaxial-induced transitions. *Applied Physics Letters*, 84(25):5261–5263, 2004. Cited on page 48.

[46] J. Wang, J. B. Neaton, H. Zheng, V. Nagarajan, S. B. Ogale, B. Liu, D. Viehland, V. Vaithyanathan, D. G. Schlom, U. V. Waghmare, N. A. Spaldin, K. M. Rabe, M. Wuttig, and R. Ramesh. Epitaxial bifeo3 multiferroic thin film heterostructures.

Science, 299(5613):1719–1722, 2003. doi:10.1126/science.1080615. Cited 2 times on page(s) 48 and 105.

[47] Dae Ho Kim, Ho Nyung Lee, Michael D. Biegalski, and Hans M. Christen. Effect of epitaxial strain on ferroelectric polarization in multiferroic bifeo3 films. *Applied Physics Letters*, 92(1), 2008. URL: http://scitation.aip.org/content/aip/journal/apl/92/1/10.1063/1.2830799, doi:http://dx.doi.org/10.1063/1.2830799. Cited on page 48.

[48] Seiji Nakashima, Hironori Fujisawa, Masafumi Kobune, Masaru Shimizu, and Yasutoshi Kotaka. Growth and local structure of bifeo 3 thin films with giant tetragonality on srruo 3 -buffered srtio 3 (001) substrate by ion beam sputtering. *Japanese Journal of Applied Physics*, 53(5S1):05FE05, 2014. URL: http://stacks.iop.org/1347-4065/53/i=5S1/a=05FE05. Cited 3 times on page(s) 48, 105, and 106.

[49] D. Lebeugle, D. Colson, A. Forget, and M. Viret. Very large spontaneous electric polarization in bifeo3 single crystals at room temperature and its evolution under cycling fields. *Applied Physics Letters*, 91(2), 2007. URL: http://scitation.aip.org/content/aip/journal/apl/91/2/10.1063/1.2753390, doi:http://dx.doi.org/10.1063/1.2753390. Cited 2 times on page(s) 48 and 49.

[50] Kwi Young Yun, Dan Ricinschi, Takeshi Kanashima, and Masanori Okuyama. Enhancement of electrical properties in polycrystalline bifeo3 thin films. *Applied Physics Letters*, 89(19), 2006. URL: http://scitation.aip.org/content/aip/journal/apl/89/19/10.1063/1.2385859, doi:http://dx.doi.org/10.1063/1.2385859. Cited on page 49.

[51] J. M. Grace, D. B. McDonald, M. T. Reiten, J. Olson, R. T. Kampwirth, and K. E. Gray. Effect of oxidant on resputtering of bi from bi–sr–ca–cu–o films. *Journal of Vacuum Science and Technology A*, 10(4):1600–1603, 1992. URL: http://scitation.aip.org/content/avs/journal/jvsta/10/4/10.1116/1.578051, doi:http://dx.doi.org/10.1116/1.578051. Cited on page 49.

[52] Yibin Li, Thirumany Sritharan, Sam Zhang, Xiaodong He, Yang Liu, and Tupei Chen. Multiferroic properties of sputtered bifeo3 thin films. *Applied Physics Letters*, 92(13), 2008. URL: http://scitation.aip.org/content/aip/journal/apl/92/13/10.1063/1.2901871, doi:http://dx.doi.org/10.1063/1.2901871. Cited on page 49.

[53] H. Béa, M. Bibes, A. Barthélémy, K. Bouzehouane, E. Jacquet, A. Khodan, J.-P. Contour, S. Fusil, F. Wyczisk, A. Forget, D. Lebeugle, D. Colson, and M. Viret. Influence of parasitic phases on the properties of bifeo3 epitaxial thin films. *Applied Physics Letters*, 87(7), 2005. URL: http://scitation.aip.org/content/aip/journal/apl/87/7/10.1063/1.2009808, doi:http://dx.doi.org/10.1063/1.2009808. Cited 3 times on page(s) 49, 103, and 107.

[54] R. R. Das, D. M. Kim, S. H. Baek, C. B. Eom, F. Zavaliche, S. Y. Yang, R. Ramesh, Y. B. Chen, X. Q. Pan, X. Ke, M. S. Rzchowski, and S. K. Streiffer. Synthesis and ferroelectric properties of epitaxial bifeo3 thin films grown by sputtering. *Applied Physics Letters*, 88(24), 2006. URL: http://scitation.aip.org/content/aip/journal/apl/88/24/10.1063/1.2213347, doi:http://dx.doi.org/10.1063/1.2213347. Cited on page 49.

[55] S. Nakashima, Y. Takada, T. Ito, S. Seto, H. Fujisawa, M. Kobune, and M. Shimizu. Preparation and characterization of high quality lead-free bifeo3 thin films by sputtering process. In *Emerging Trends in Engineering and Technology (ICETET), 2012 Fifth International Conference on*, pages 128–131, Nov 2012. doi:10.1109/ICETET.2012.12. Cited on page 49.

[56] R. K. Kotnala, Rekha Gupta, and Sujeet Chaudhary. Giant magnetoelectric coupling interaction in batio3/bifeo3/batio3 trilayer multiferroic heterostructures. *Applied Physics Letters*, 107(8), 2015. URL: http://scitation.aip.org/content/aip/journal/apl/107/8/10.1063/1.4929729, doi:http://dx.doi.org/10.1063/1.4929729. Cited on page 50.

[57] R. Y. Zheng, X. S. Gao, Z. H. Zhou, and J. Wang. Multiferroic bifeo3 thin films deposited on srruo3 buffer layer by rf sputtering. *Journal of Applied Physics*, 101(5), 2007. URL: http://scitation.aip.org/content/aip/journal/jap/101/5/10.1063/1.2437163, doi:http://dx.doi.org/10.1063/1.2437163. Cited on page 50.

[58] Afm (atomic force microscope). URL: http://www3.physik.uni-greifswald.de/method/afm/eafm.htm. Cited on page 51.

[59] Piezoresponse force microscopy. URL: http://en.wikipedia.org/wiki/Piezoresponse_force_microscopy. Cited on page 51.

[60] Igor Stolichnov, Ludwig Feigl, Leo J. McGilly, Tomas Sluka, Xian-Kui Wei, Enrico Colla, Arnaud Crassous, Konstantin Shapovalov, Petr Yudin, Alexander K. Tagantsev, and Nava Setter. Bent Ferroelectric Domain Walls as Reconfigurable

Metallic-Like Channels. *Nano Letters*, 15(12):8049–8055, December 2015. doi:10.1021/acs.nanolett.5b03450. Cited on page 53.

[61] Piezoresponse force microscopy (pfm) - introduction, principles and instrumental aspects of piezoresponse force microscopy by nt-mdt. URL: http://www.azonano.com/article.aspx?ArticleID=2682. Cited on page 53.

[62] C. S. Ganpule, V. Nagarajan, B. K. Hill, A. L. Roytburd, E. D. Williams, R. Ramesh, S. P. Alpay, A. Roelofs, R. Waser, and L. M. Eng. Imaging three-dimensional polarization in epitaxial polydomain ferroelectric thin films. *Journal of Applied Physics*, 91(3):1477–1481, February 2002. doi:10.1063/1.1421219. Cited 2 times on page(s) 54 and 145.

[63] André Marino Goncalves. *Visualização, Caracterização e Manipulação de Paredes de Domínios em Filmes Finos Ferroelétricos*. PhD thesis, Universidade Federal de São Carlos - UFSCAR, 2017. Cited on page 54.

[64] Anne Lamirand. *Epitaxial growth, atomic structure and exchange coupling of ultrathin bilayers of oxides on metals.* PhD thesis, 2014. Cited 3 times on page(s) 55, 56, and 62.

[65] Wikipedia. Bragg's law. URL: https://en.wikipedia.org/wiki/Bragg's_law. Cited on page 58.

[66] X-ray diffraction. URL: http://encyclopedia2.thefreedictionary.com/x-ray+diffraction. Cited on page 58.

[67] Miho Yasaka. X-ray reflectivity measurement. *The Rigaku Journal*, 26(2), 2010. URL: http://www.eng.uc.edu/~beaucag/Classes/Characterization/

ReflectivityLab/X-ray%20thin-film%20measurement%20techniques_V_X-ray%20reflectivity%20measurement.pdf. Cited 3 times on page(s) 61, 62, and 63.

[68] M.A. Heald and J.B. Marion. *Classical Electromagnetic Radiation*. Saunders College Pub., 1995. URL: http://books.google.com.br/books?id=k7zvAAAAMAAJ. Cited 2 times on page(s) 66 and 67.

[69] J.D. Jackson. *Classical electrodynamics*. Wiley, 1975. URL: http://books.google.com.br/books?id=_7rvAAAAMAAJ. Cited 2 times on page(s) 67 and 70.

[70] P. Willmott. *An Introduction to Synchrotron Radiation: Techniques and Applications*. Wiley, 2011. URL: http://books.google.com.br/books?id=0P51ZEjvZYUC. Cited on page 68.

[71] J C Cezar, P T Fonseca, G L M P Rodrigues, A R B de Castro, R T Neuenschwander, F Rodrigues, B C Meyer, L F S Ribeiro, A F A G Moreira, J R Piton, M A Raulik, M P Donadio, R M Seraphim, M A Barbosa, A de Siervo, R Landers, and A Naves de Brito. The u11 pgm beam line at the brazilian national synchrotron light laboratory. *Journal of Physics: Conference Series*, 425(7):072015, 2013. URL: http://stacks.iop.org/1742-6596/425/i=7/a=072015. Cited on page 72.

[72] R. Nakajima, Stanford University. Dept. of Materials Science, and Engineering. *X-ray Magnetic Circular Dichroism Spectroscopy in Transition Metal Thin Films*. Stanford University, 1998. URL: http://books.google.com.br/books?id=_zOzGwAACAAJ. Cited 2 times on page(s) 77 and 80.

[73] Joachim Stöhr and HC Siegmann. Magnetism: From fundamentals to nanoscale dynamics. *Springer Series in Solid-State Sciences*, 152, 2006. Cited 2 times on page(s) 80 and 81.

[74] R M Tromp, Y Fujikawa, J B Hannon, A W Ellis, A Berghaus, and O Schaff. A simple energy filter for low energy electron microscopy/photoelectron emission microscopy instruments. *Journal of Physics: Condensed Matter*, 21(31):314007, 2009. URL: http://stacks.iop.org/0953-8984/21/i=31/a=314007. Cited on page 84.

[75] Tutorial - contrast using peem. URL: http://xraysweb.lbl.gov/peem2/webpage/Project/TutorialContrast.shtml. Cited 2 times on page(s) 85 and 86.

[76] Tutorial - time-resolved peem. URL: http://xraysweb.lbl.gov/peem2/webpage/Project/TutorialTRPEEM.shtml. Cited on page 87.

[77] Prashant R. Potnis, Nien-Ti Tsou, and John E. Huber. A review of domain modelling and domain imaging techniques in ferroelectric crystals. *Materials*, 4(2):417–447, 2011. URL: http://www.mdpi.com/1996-1944/4/2/417, doi:10.3390/ma4020417. Cited on page 88.

[78] R. V. Chopdekar, V. K. Malik, A. Fraile Rodríguez, L. Le Guyader, Y. Takamura, A. Scholl, D. Stender, C. W. Schneider, C. Bernhard, F. Nolting, and L. J. Heyderman. Spatially resolved strain-imprinted magnetic states in an artificial multiferroic. *Phys. Rev. B*, 86:014408, Jul 2012. URL: http://link.aps.org/doi/10.1103/PhysRevB.86.014408, doi:10.1103/PhysRevB.86.014408. Cited 2 times on page(s) 91 and 92.

[79] Parasitic phases at the origin of magnetic moment in $BiFeO_3$ thin films grown by low deposition rate RF sputtering. 122(12). doi:10.1063/1.5003764. Cited 2 times on page(s) 95 and 108.

[80] V. Laukhin, V. Skumryev, X. Martí, D. Hrabovsky, F. Sánchez, M. V. García-Cuenca, C. Ferrater, M. Varela, U. Lüders, J. F. Bobo, and J. Fontcuberta. Electric-field

control of exchange bias in multiferroic epitaxial heterostructures. *Phys. Rev. Lett.*, 97:227201, Nov 2006. doi:10.1103/PhysRevLett.97.227201. Cited on page 96.

[81] Yong Tae Kim, Ik Soo Kim, Seong Il Kim, Dong Chul Yoo, and Jeong Yong Lee. Atomic structure of random and c-axis oriented ymno3 thin films deposited on si and y2o3/si substrates. *Journal of Applied Physics*, 94(8):4859–4862, 2003. doi:10.1063/1.1604460. Cited on page 97.

[82] Seiji Nakashima, Yosuke Tsujita, Hironori Fujisawa, Jung Min Park, Takeshi Kanashima, Masanori Okuyama, and Masaru Shimizu. Characterization of epitaxial bifeo3 thin films prepared by ion beam sputtering. *Current Applied Physics*, 11(3, Supplement):S244 – S246, 2011. Joint International Conference on the 7th Asian Meeting on Ferroelectricity (AMF-7) and the 7th Asian Meeting on ElectroceramicsSpecial Issue: AMF/AMEC-7. URL: http://www.sciencedirect.com/science/article/pii/S156717391000430X, doi:http://dx.doi.org/10.1016/j.cap.2010.11.066. Cited on page 103.

[83] Seiji Nakashima, Hironori Fujisawa, Hiroyuki Suminaga, Jung Min Park, Hiroshi Nishioka, Masafumi Kobune, Takeshi Kanashima, Masanori Okuyama, and Masaru Shimizu. Preparation of bifeo 3 thin films on srruo 3 /srtio 3 (001) substrate by dual ion beam sputtering. *Japanese Journal of Applied Physics*, 50(9S2):09NB01, 2011. URL: http://stacks.iop.org/1347-4065/50/i=9S2/a=09NB01. Cited 2 times on page(s) 103 and 107.

[84] R. Y. Zheng, C. H. Sim, J. Wang, and S. Ramakrishna. Effects of sro buffer layer on multiferroic bifeo3 thin films. *Journal of the American Ceramic Society*, 91(10):3240–

3244, 2008. URL: http://dx.doi.org/10.1111/j.1551-2916.2008.02536.x, doi:10.1111/j.1551-2916.2008.02536.x. Cited on page 108.

[85] S. Tanuma, T. Shiratori, T. Kimura, K. Goto, S. Ichimura, and C. J. Powell. Experimental determination of electron inelastic mean free paths in 13 elemental solids in the 50 to 5000 ev energy range by elastic-peak electron spectroscopy. *Surface and Interface Analysis*, 37(11):833–845, 2005. URL: http://dx.doi.org/10.1002/sia.2102, doi:10.1002/sia.2102. Cited on page 124.

[86] G. Radaelli, M. Cantoni, Li Lijun, M. Espahbodi, and R. Bertacco. Two dimensional growth of ultrathin fe films on batio3 with sharp chemical interface. *Journal of Applied Physics*, 115(6):063501, 2014. URL: http://dx.doi.org/10.1063/1.4864375, arXiv:http://dx.doi.org/10.1063/1.4864375, doi:10.1063/1.4864375. Cited on page 134.

Appendix A

Events and publications

In the next section we list the opportunities we had to present our work and the scientific publications associated with this thesis.

A.1 Presentations and schools

- from 3/11/2013 to 9/11/2013, IX Brazilian School on Magnetism, Vitória, ES, poster presentation "Study of domain walls in ferroelectrics and multiferroics thin films: the sample growth"
- from 11/03/2014 to 12/03/2014, Brazilian Synchrotron Radiation Laboratory (LNLS) Users Meeting, Campinas, SP
- from 12/05/2014 to 16/05/2014, XXXVII Brazilian Physics Society Condensed Matter Meeting, Costa do Sauípe, BA, poster presentation "Structural characterization of multiferroic/magnetic multilayers"
- from 14/09/2014 to 18/09/2014, LEEM/PEEM-9, Berlin
- from 6/01/2014 a 17/01/2014, V Curso Teorico-Pratico de Microscopia Eletrônica

de Transmissao, Campinas, SP. Evento organizado pelo Laboratório Nacional de Nanotecnologia (LNNano), totalizando 120 horas de cursos teóricos e experimentais

- de 1/09/2014 a 12/09/2014, School on UV and X-ray spectroscopy of strongly correlated electrons systems, les Houches, France
- from July 13^{th} to 24^{th}, 2015 : São Paulo School of Advanced Sciences on Recent Developments in Synchrotron Radiation (SyncLight2015), held by the Brazilian Synchrotron Light Laboratory (LNLS) at the Brazilian Center for Research in Energy and Materials, Campinas, Brazil.
- from July 30^{th} until August 1^{st} 2015 : Second International Workshop on Advances in Multifunctional Multiferroic Materials and Their Applications, and the 2015 International Network for Advanced and Multifunctional Materials Meeting, held in Maringá-PR, Brazil.
- from September 11 th to 15 th , 2016 : 10th LEEM/PEEM workshop, Monterey - California, presentation of a poster.
- from December 7 th to 9 th 2016 : 8th Joint BER II and BESSY II User Meeting, Berlin, Germany, presentation of a poster.

A.2 Publications

- Mori, T. J. A., Mouls, C. L., Morgado, F. F., Schio, P. and Cezar, J. C.. (2017) *"Parasitic phases at the origin of magnetic moment in BiFeO3 thin films grown by low deposition rate RF sputtering"*, Journal of Applied Physics, 122 (12), p. 124102. doi: 10.1063/1.5003764.

- Mouls, C. L. et al., *"Magnetoelectric coupling between ferroelectric and ferromagnetic domains in ultra-thin Fe layers on $BaTiO_3$ substrates"*, in preparation.